



Joint inversion of surface wave dispersion and receiver functions: A Bayesian Monte-Carlo approach

Journal:	<i>Geophysical Journal International</i>
Manuscript ID:	GJI-S-12-0278.R1
Manuscript Type:	Research Paper
Date Submitted by the Author:	22-Aug-2012
Complete List of Authors:	Shen, Weisen; University of Colorado at Boulder, Center for Imaging the Earth's Interior, Department of Physics Ritzwoller, Michael; University of Colorado at Boulder, Center for Imaging the Earth's Interior, Department of Physics Schulte-Pelkum, Vera; University of Colorado at Boulder, Cooperative Institute for Research in Environmental Sciences and Department of Geological Sciences Lin, Fan-Chi; California Institute of Technology, Seismological Laboratory
Keywords:	Seismic tomography < SEISMOLOGY, Inverse theory < GEOPHYSICAL METHODS, Surface waves and free oscillations < SEISMOLOGY, Composition of the continental crust < COMPOSITION and PHYSICAL PROPERTIES

Joint inversion of surface wave dispersion and receiver functions: A Bayesian Monte-Carlo approach

Weisen Shen¹, Michael H. Ritzwoller¹, Vera Schulte-Pelkum² and Fan-Chi Lin³

1 – Center for Imaging the Earth's Interior, Department of Physics, University of Colorado at Boulder, Boulder, CO 80309, USA (weisen.shen@colorado.edu)

2 – Cooperative Institute for Research in Environmental Sciences and Department of Geological Sciences, University of Colorado at Boulder, Boulder, CO 80309, USA

3 – Seismological Laboratory, Division of Geological and Planetary Sciences, California Institute of Technology, Pasadena, CA 91125, USA

Abstract

A non-linear Bayesian Monte-Carlo method is presented to estimate a Vsv model beneath stations by jointly interpreting Rayleigh wave dispersion and receiver functions and associated uncertainties. The method is designed for automated application to large arrays of broadband seismometers. As a testbed for the method, 185 stations from the USArray Transportable Array are used in the Intermountain West, a region that is geologically diverse and structurally complex. Ambient noise and earthquake tomography are updated by applying eikonal and Helmholtz tomography, respectively, to construct Rayleigh wave dispersion maps from 8 sec to 80 sec across the study region with attendant uncertainty estimates. A method referred to as “harmonic stripping method” is described and applied as a basis for quality control and to generate back-azimuth independent receiver functions for a horizontally-layered, isotropic effective medium with uncertainty estimates for each station. A smooth parameterization between (as well as above and below) discontinuities at the base of the sediments and crust suffices to fit most features of both data types jointly across most of the study region. The effect of introducing receiver functions to surface wave dispersion data is quantified through improvements in the posterior marginal distribution of model variables. Assimilation of receiver functions quantitatively improves the accuracy of estimates of Moho depth, improves the determination of the Vsv contrast across Moho, and improves uppermost mantle structure because of the ability to relax a priori constraints. The method presented here is robust and can be applied systematically to construct a 3-D model of the crust and uppermost mantle across the large networks of seismometers that are developing globally, but also provides a framework for further refinements in the method.

Key words: Inverse theory, Seismic tomography, Surface waves and free oscillations,

Composition of the continental crust

1. Introduction

The construction of crustal and uppermost mantle velocity models over extended regions is critical to an understanding of continental tectonics and the thermal and compositional structure of the lithosphere as well as to provide the structural framework for an assessment of natural hazards. Surface waves provide spatially continuous information that is useful in developing 3-D shear wave velocity (V_s) models at regional (e.g., Levshin and Ritzwoller, 1995; Ritzwoller et al., 1998; Levin et al., 2002; Ritzwoller et al., 2003; Levshin et al., 2005; Yang and Forsyth, 2006; Shapiro et al., 2008; Yang et al., 2011), continental (e.g., Ritzwoller and Levshin, 1998; Ritzwoller et al., 2001, Villasenor et al., 2001; Bensen et al., 2009) and global (e.g., Shapiro and Ritzwoller, 2002; Ritzwoller et al., 2004) scales. Receiver functions (RFs), in contrast, provide the spatially discrete local response of seismic waves to discontinuities beneath receiver locations (Vinnik, 1977; Langston, 1979). Receiver functions also have been applied to construct local 1-D (Ammon and Zandt, 1993) and 3-D models (Vinnik et al., 2004, Vinnik et al., 2006). The use of each type of data alone presents significant non-uniqueness problems (e.g., Ammon et al., 1990; Shapiro et al., 2002): surface wave data do not image discontinuities whereas receiver functions do not strongly constrain absolute shear velocities between discontinuities (although they do constrain the contrast in S-wave velocity across the discontinuity). As a consequence, combining the two complementary data types was a natural direction for efforts to determine structure near to Earth's surface and was introduced more than a decade ago (e.g., Last et al., 1997, Ozalaybey et al., 1997), with numerous realizations of the idea having subsequently been developed. Linearized joint inversions have been particularly popular (e.g., Du and Foulger, 1999; Julia et al., 2000, 2003; Endrun et al., 2004, Horspool et al., 2006, Gok et al., 2007, Tkalčić et al., 2006; Pasyanos et al., 2007; Yoo et al., 2007; Tokam et al., 2010, Salah et al., 2011, Bailey et al., 2012).

Non-linear inversions based on model-space sampling methods such as Markov Chain Monte Carlo perhaps augmented by Bayesian approaches to construct ensembles of models that are used to quantify the degree of belief about earth structures (Mosegaard and Tarantola, 1995; Sambridge, 2001; Mosegaard and Sambridge, 2002; Sambridge and Mosegaard, 2002) also have been applied in both receiver function inversions (e.g., Shibutani et al., 1996; Zhao et al., 1996;

1
2
3 Levin and Park, 1997; Sambridge 1999a; Clitheroe *et al.*, 2000; Piana Agostinetti *et al.*, 2002;
4 Bannister *et al.*, 2003; Fredericksen *et al.*, 2003; Nicholson *et al.*, 2003; Vinnik *et al.*, 2004, 2006;
5 Lucente *et al.*, 2005; Hetenyi and Bus, 2007; Piana Agostinetti and Chiarabba, 2008; Piana
6 Agostinetti and Malinverno, 2010) and surface wave inversions (e.g., Shapiro *et al.*, 2002;
7 Yoshizawa and Kennett, 2002; Socco and Boiero, 2008; Maraschini and Foti, 2010; Molnar *et al.*,
8 2010; Khan *et al.*, 2011) with varying degrees of theoretical sophistication, generality, spatial
9 extent, and data quantity. Joint inversions of receiver functions and surface wave dispersion or
10 other geophysical data within the context of a non-linear, model-space sampling scheme are
11 more rare and recent (An and Assumpcao, 2004; Chang *et al.*, 2004; Lawrence and Wiens, 2004;
12 Vinnik *et al.*, 2006; Liu *et al.*, 2010; Moorkamp *et al.*, 2010; Tokam *et al.*, 2010; Basuyau and
13 Tiberi, 2011; Bodin *et al.*, 2011).

14
15
16
17
18
19
20
21
22
23
24 Despite these advances, the joint interpretation of surface wave dispersion and receiver functions
25 is still faced with at least four significant challenges. First, as traditionally applied, surface waves
26 and receiver functions have yielded information at different lateral length scales. Second, also
27 traditionally, surface wave dispersion information has derived from teleseismic earthquakes and
28 has been produced mostly at long periods (> 20 sec), which are not ideally sensitive to the earth's
29 crust. Third, joint quantitative interpretation requires meaningful uncertainties for both data
30 types. Fourth, the uncertainties in the resulting model must be quantified. Inextricably related to
31 this is the need to find a model parameterization that possesses all and only the detail of structure
32 necessary to fit both types of data. The purpose of this paper is to develop an approach to joint
33 interpretation of surface wave dispersion and receiver functions that addresses these challenges
34 in a practical, computationally efficient way that allows for automated application to large arrays
35 of seismometers.

36
37
38
39
40
41
42
43
44
45 The first challenge has been ameliorated by the recent deployment of large seismic arrays such as
46 the Earthscope/USarray Transportable Array (TA), CEArray in China (Zheng *et al.*, 2010), the
47 Virtual European Broadband Seismic Network, and PASSCAL and Flexible Array experiments
48 in which relatively close station spacing (50-100 km) allows much better resolution from surface
49 waves. Recent developments in surface wave tomography have been stimulated to exploit these
50 arrays. Examples of array-based surface wave tomography methods include the two-plane wave
51 and related methods (Pollitz, 2008; Yang *et al.*, 2008a,b; Pollitz and Snoke, 2010), eikonal
52 tomography (Lin *et al.*, 2009) and Helmholtz tomography (Lin and Ritzwoller, 2011). These new
53
54
55
56
57
58
59
60

array methods applied to data from the TA (e.g., Lin *et al.*, 2011; Ritzwoller *et al.*, 2011) and CEArray (Zhou *et al.*, 2012) generate surface wave dispersion maps of unprecedented resolution (50-75 km) across large regions. In addition, tomographic methods based on ambient noise have been developed to augment information from teleseismic earthquakes. Ambient noise tomography (ANT) produces relatively short period (8-40 sec) surface wave information that agrees with information from teleseismic earthquakes in the period band of overlap (25-40 sec) (e.g., Yang and Ritzwoller, 2008; Ritzwoller *et al.*, 2011). Dispersion information from ambient noise, therefore, constrains the crust in a way that is directly complementary to receiver function analyses. The second challenge facing the joint interpretation of surface wave and receiver function information, therefore, is addressed by the development of ANT. Indeed, inversions for 3-D models of the crust and uppermost mantle based on surface wave dispersion information from ANT (perhaps with earthquake tomography) have been increasingly common in the past few years (e.g., Bensen *et al.*, 2009; Lin *et al.*, 2011; Moschetti *et al.*, 2010a,b; Yang *et al.*, 2008a,b; Yang *et al.*, 2012; Zheng *et al.*, 2011; Zhou *et al.*, 2012).

The third challenge, determining uncertainty estimates for both types of data, has been partially solved recently for surface waves by the eikonal and Helmholtz tomography methods, which produce reliable error estimates for both ambient noise and earthquake tomography. We discuss in the Appendix a method to construct receiver functions referred to as harmonic stripping based on azimuthal harmonic analysis (e.g., Girardin and Farra, 1998; Bianchi *et al.*, 2010) that we use both to construct azimuthally independent receiver functions and estimate their uncertainty. Bodin *et al.* (2011) insightfully and in considerable detail discuss the importance of reliable uncertainty information, with particular emphasis on the need to estimate full data covariance matrices in the joint inversion. Finally, the fourth challenge, estimating model uncertainties, is addressed by the Bayesian Monte Carlo method that we develop and describe here. We show along the way that a quite simple model parameterization based on smooth B-splines in the crust and mantle can fit both data types at most locations across the western US.

Therefore, we present here a non-linear Bayesian Monte-Carlo algorithm to estimate a Vs model beneath stations by jointly interpreting surface wave dispersion and receiver functions and associated uncertainties. The method is designed specifically to be applied automatically to large numbers of seismic stations. As a testbed for the method, we use 185 stations from the TA in the Intermountain West (Fig. 1). We first update the ambient noise and earthquake tomography to

1
2
3 construct Rayleigh wave dispersion maps from 8 sec to 80 sec across the study region. Eikonal
4 and Helmholtz tomography are applied to estimate uncertainties in ambient noise and earthquake
5 dispersion information and the harmonic stripping method is used to generate back-azimuth
6 independent receiver functions with uncertainty estimates for each station. After applying the
7 joint inversion (and for comparison the inversion based on surface wave dispersion alone) at
8 each station, the final 3D model of the crust and uppermost mantle is produced by interpolating
9 between stations using simple-kriging at each model depth. Prior and posterior marginal
10 distributions are presented to visualize changes in uncertainties for each data set. The study
11 region is geologically diverse and structurally complex and provides an excellent proving ground
12 for the methodology.
13
14
15
16
17
18
19
20
21

22 **2. Overview of the Method**

23
24 Monte Carlo and related parameter search algorithms (e.g., Sambridge, 1999a) are designed to
25 map data misfit across a broad range of model space. Within a Bayesian framework, these
26 models are interpreted by computing the a posteriori (or posterior) probability distribution, which
27 is the probability distribution of the model parameters given the observed data. Bayes' theorem
28 allows the posterior distribution $\sigma(m)$ for a model m to be computed from the prior information
29 on model space (given by the prior probability density $\rho(m)$ for model m) and the observed data
30 as represented by the likelihood functional $L(m)$ (the probability of observing the measured data
31 given a particular model):
32
33
34
35
36
37

$$38 \quad \sigma(m) \propto \rho(m)L(m) \quad (1)$$

39
40
41 Geophysical applications of Bayesian inference have been presented by Tarantola and Valette
42 (1982), Mosegaard and Tarantola (1995), and Sambridge (1999b). The key steps are the
43 expression of prior information as a probability density function and the computation of the
44 likelihood functional, which is determined from data misfit. From a set of models distributed like
45 the posterior distribution, one can then determine certain properties of the ensemble (e.g., best
46 fitting model, mean model, median model), the covariance between model parameters, or the
47 marginal distribution of particular model parameters or quantities derived from the model
48 parameters.
49
50
51
52
53
54

55
56 The procedure we have developed to jointly invert surface wave dispersion information and
57
58
59
60

receiver functions is similar in motivation and even in some of the details to the methods described by Bodin *et al.* (2011). We present a general overview of our methodology here as a guidepost to the principal results in the paper. We will also point out some differences with the method of Bodin *et al.* (2011). The data used in the inversion are described in detail in section 3.

The model parameterization and the construction of the prior distribution are presented in section 4. The prior information includes ranges in which individual model parameters are allowed to vary as well as rules that govern the relative values of different model parameters. Examples of the prior distribution for several model parameters are shown in Figure 9.

The likelihood functional is simply related to the misfit function $S(m)$ as follows:

$$L(m) = \exp\left(-\frac{1}{2}S(m)\right) \quad (2)$$

where

$$S(m) = \left(g(m) - D^{obs}\right)^T C_e^{-1} \left(g(m) - D^{obs}\right) \quad (3)$$

and D^{obs} is a vector of measured data, $g(m)$ is the vector of data predicted from model m , C_e is the data covariance matrix, and T represents transpose of a vector. For surface wave dispersion here the vector D^{obs} consists of Rayleigh wave phase velocities observed on a discrete set period grid and for receiver functions D^{obs} is the azimuthally independent receiver function over a fixed discrete time grid.

The Markov Chain Monte Carlo sampling of model space to generate the posterior distribution evolves as follows. A model m_j is selected from the prior distribution. A second model m_i is drawn and the likelihoods $L(m_i)$ and $L(m_j)$ are computed. The Metropolis law defines the probability of acceptance for model m_i :

$$P_{accept} = \begin{cases} 1 & \text{if } L(m_i) \geq L(m_j) \\ L(m_i) / L(m_j) & \text{if } L(m_i) < L(m_j) \end{cases} \quad (4)$$

That is, model m_i is accepted if its likelihood is greater than that of model m_j (i.e., its misfit is lower). Even if its likelihood is smaller than that of model m_j it may still be accepted, however. For example, if $P_{accept} = 0.4$, we use a uniformly distributed random deviate generated between 0 and 1. If the value is less than 0.4 we accept the model. If the new model m_i is accepted, we

1
2
3 define a new perturbation based on this model and search on. If the new model is not accepted,
4 we make a record of it and its associated misfit information and start a new perturbation based on
5 the previously accepted model m_j to choose the next step. The evolution of the algorithm in terms
6 of improving misfit for surface wave data alone is shown in [Figure 8](#) and for the joint inversion
7 in [Figure 11](#).
8
9

10
11
12 An additional model acceptance criterion then is applied to define the posterior distribution. In
13 this we diverge from strict Bayesian methodology. If the data covariance matrix were known
14 accurately, the choice of the acceptance criterion would be straightforward. Misfits to surface
15 wave and receiver function data would be commensurable and the acceptance criterion would
16 involve only choosing a probability threshold in the posterior distribution. As described later,
17 because of difficulty in estimating the off-diagonal elements of the data covariance matrices, we
18 have assumed that the surface wave dispersion data and the receiver functions have error
19 processes that are independently but not identically distributed so that each covariance matrix is
20 diagonal with elements σ_i^2 and s_j^2 , respectively, for phase velocity at period i and receiver
21 function at time j . This assumption has the practical effect that the misfits between the two data
22 types are incommensurable. We are, therefore, forced to introduce a misfit scaling parameter κ
23 to normalize the misfits between the two data types, as described in section 6.1. The resulting joint
24 misfit function, therefore, has the following form:
25
26
27
28
29
30
31
32
33
34
35

$$S_{\text{joint}}(m) = S_{SW} + \frac{1}{\kappa} S_{RF} = \sum_{i=1}^N \frac{(g_i(m) - D_i^{obs})^2}{\sigma_i^2} + \frac{1}{\kappa} \sum_{j=1}^M \frac{(R_j(m) - A_0(t_j))^2}{s_j^2} \quad (5)$$

36
37
38 where $g_i(m)$ is the phase velocity predicted for model m at period i on a discrete grid of N periods,
39 D^{obs} is the observed phase velocity, the function $A_0(t_j)$ is the observed receiver function at time t_j
40 on a discrete grid of M times and $R_j(m)$ is the predicted receiver function for model m at time t_j .
41
42
43
44
45
46
47
48
49

50 Somewhat different model acceptance criteria are applied in the inversion with surface wave data
51 alone in section 5 and in the joint inversion in section 6. Example posterior marginal
52 distributions are shown in [Figures 9](#) and [12](#).
53
54
55
56

57 The methods that we present here differ from those of [Bodin et al. \(2011\)](#) in two principal ways.
58
59
60

1
2
3 First, we choose smooth velocity profiles between specified boundaries at variable depths and fix
4 the parameterization across the region of application. The nominal “transdimensionality” of the
5 method of Bodin et al. refers to the variable parameterization of their method. We do not use an
6 adaptive parameterization because, for the most part, we find that the parameterization we
7 choose is sufficiently flexible to fit the data. Second, as discussed above, we do not estimate the
8 off-diagonal elements of the covariance matrices. Inspired by the hierarchical Bayesian
9 formalism of Bodin et al., we attempted to estimate full covariance matrices for receiver
10 functions, but found first that the estimated covariance matrices were singular and did not yield
11 to matrix regularization methods designed to approximate the inverse matrices. Second, the
12 covariance matrices that we derived were appropriate for a raw receiver function not the
13 estimated azimuthally independent receiver function $A_0(t)$ that we use in the inversion. This is a
14 subtle point that requires further analysis. For both reasons, we moved forward with diagonal
15 covariance matrices for both dispersion data and receiver functions. Although these differences
16 with the more general formulation of Bodin et al. (2011), which attempted to estimate the full
17 covariance matrices for receiver functions, were motivated in part by our inability to estimate
18 satisfactory covariance matrices, they do accelerate the inversion, which facilitates the
19 application of the method to a large array like the USArray. In addition, as we show, the method
20 works well to improve 3D models relative to those produced from surface wave dispersion data
21 alone.
22
23
24
25
26
27
28
29
30
31
32
33
34
35
36

37 **3. Data Processing**

38 **3.1 Rayleigh wave data processing**

39 **3.1.1 Ambient noise tomography (ANT)**

40
41
42 The method of ambient noise tomography is now well established, including cross-correlation of
43 long pre-processed time series to generate empirical Green’s functions, measuring both Rayleigh
44 and Love wave phase and group velocity curves, and producing dispersion maps at particular
45 periods (Shapiro et al., 2005, Yang et al., 2007, Moschetti et al., 2007, Yao et al., 2006). The
46 data processing procedures that we adopt follow those of Bensen et al. (2007) and Lin et al.
47 (2008), which we only briefly summarize here. First, raw vertical component seismograms
48 recorded from 2005 to 2010 are downloaded from the IRIS DMC for the USArray TA stations in
49 the western and central US and are cut into 1-day time series. The time series length of each
50
51
52
53
54
55
56
57
58
59
60

1
2
3 station is usually about two years, but time series lengths are variable and we do not apply a
4 minimum time series length restriction. Second, earthquake signals and other types of
5 interference are removed by time domain normalization, in which the reciprocal of the mean of
6 the absolute value of the waveform in a moving 80 sec time window is used to weight the data
7 point at the center of the window. The weights are determined in the “earthquake band” between
8 periods of 15 and 50 sec period, but then are applied to the unfiltered data. Third, the data are
9 band-pass filtered between 5 and 100 sec period and cross-correlation is performed between all
10 station pairs. Then, Rayleigh wave group and phase velocity dispersion measurements are
11 obtained from the symmetric component of each inter-station cross-correlation by performing
12 automatic frequency-time analysis (FTAN) (Bensen *et al.*, 2007) . In this study, only Rayleigh
13 wave phase velocity measurements are used. The automated FTAN dispersion measurements are
14 winnowed by applying two criteria to select reliable measurements for surface wave
15 tomography: (1) The inter-station distance must be greater than three wavelengths at each period
16 to ensure the far-field approximation and sufficient separation from precursory noise and (2)
17 signal-to-noise ratio (SNR) must be greater than 10 at each period for the measurement at that
18 period to be accepted. Once all measurements are obtained, eikonal tomography (Lin *et al.*, 2009)
19 is then applied to produce phase velocity maps from 8 to 40 sec period. Eikonal tomography
20 takes account of ray bending (off-great circle propagation) but does not model finite frequency
21 effects (Lin and Ritzwoller, 2011) . One of the signature features of eikonal tomography is that it
22 produces meaningful uncertainty estimates at each geographical location. This is done by
23 accumulating phase velocity estimates at a given location from many central stations, fitting and
24 then removing a truncated Fourier Series over azimuth to estimate azimuthal anisotropy, and
25 then measuring the standard deviation of the mean of the residual. Figure 2a-c presents phase
26 velocity maps from ambient noise tomography at periods of 8, 20 and 36 sec. By 40 sec period,
27 the SNR of ambient noise has decreased enough that high resolution phase velocity maps are no
28 longer generated. Earthquake data are introduced to produce the longer period dispersion maps.
29
30
31
32
33
34
35
36
37
38
39
40
41
42
43
44
45
46
47
48
49

50 3.1.2 Earthquake tomography (ET)

51 The data processing procedure for teleseismic earthquake data is discussed by Lin and Ritzwoller
52 (2011) and is only briefly summarized here. First, teleseismic records at the USArray TA
53 stations in the western US following earthquakes with surface wave magnitudes $M_s \geq 5.0$ are
54
55
56
57
58
59
60

downloaded from the IRIS DMC and cut according to the arrival window of surface waves before instrument responses are removed. Second, FTAN is applied to the cut seismograms and Rayleigh wavefront group and phase travel times and amplitudes are measured as a function of period. Phase ambiguity is resolved using a network-based approach in which travel time measurements are compared with measurements at nearby stations using the method of Lin and Ritzwoller (2011). Then Helmholtz tomography is performed to produce Rayleigh wave phase velocity maps from 32 to 80 sec period. Uncertainties are estimated similar to eikonal tomography applied to ambient noise data, but by accumulating phase velocities over many different earthquakes. In Helmholtz tomography, finite frequency effects are corrected through a term involving the local Laplacian of the amplitude field. Figure 2d,e shows the phase velocity maps from ET at periods of 36 and 70 sec, respectively. A comparison of the 36 sec phase velocity maps obtained from ANT and ET is shown in Figure 2f. The average difference is 5 m/s with slightly faster phase velocities emerging from ET.

3.1.3 Construction of phase velocity curves at station locations

After Rayleigh wave phase velocity maps are generated on a $0.2^\circ \times 0.2^\circ$ grid from both ANT and ET, phase velocity curves are interpolated to each station location. At short periods (8-36 sec), phase velocity measurements and associated uncertainties are taken exclusively from ANT maps. At long periods (40-80 sec) results are taken solely from ET maps. Between periods of 36 sec and 40 sec, we weight the two velocity measurements by their local uncertainties and a smooth curve is produced. Figure 3 shows four dispersion curves and uncertainty estimates for TA stations R11A, T18A, Q22A and O25A whose locations are shown on Figure 1. In the overlapping period band, the phase velocity measurements from ANT and ET are overplotted, demonstrating the coherence between ANT measurements (red error-bars) and ET measurements (blue error-bars).

3.2 Receiver function data processing

In the Appendix we describe a method to estimate the azimuthally independent receiver function, $A_0(t)$, and associated uncertainty, $s(t)$, for each station. We refer to the method as “harmonic stripping” because a truncated harmonic function is fit to the azimuthally dependent raw receiver functions for a given station at each time t :

$$H(\theta, t) = A_0(t) + A_1(t)\sin(\theta + \theta_1(t)) + A_2(t)\sin(2\theta + \theta_2(t)) \quad (6)$$

where the A_i ($i=0,1,2$) are the amplitudes of the three harmonic components and the θ_i are initial phases for the azimuthally dependent components. This procedure approximately strips the azimuthal dependence from the receiver functions and produces the azimuthally independent receiver function, $A_0(t)$. As shown in the Appendix, dipping crustal interface and azimuthal anisotropy dominantly produce signals with periodicities of 2π and π , respectively, which are largely removed via harmonic stripping so that the azimuthally independent component of the fit is a reliable estimate of the receiver function for a horizontally-layered isotropic effective medium. Without complete and uniform azimuthal coverage, simply taking the average of the receiver functions over azimuth as is commonly done does not guarantee an unbiased estimate. The data processing and quality control (QC) procedures for the receiver functions are also discussed in the Appendix.

In this study we use Ps receiver functions (teleseismic P-to-S converted waves) exclusively, but Sp receiver functions could also be used in the context of the methods we develop, at least in principle (Vinnik *et al.*, 2004). We select all teleseismic events in the NEIC PDE catalogue with a body wave magnitude $m_b \geq 5.1$ within the epicentral distance range of 30° - 99° from each station. All sets of 3-component seismograms are rotated to form the radial and transverse components and are then band-pass filtered between 0.03 and 4 Hz using a Butterworth filter (2 poles, 2 passes). The harmonic stripping method and quality control procedures have been applied to the 185 TA stations in the study region (Fig. 1). An example is shown in Figure 4 for the TA station R11A. The QC'ed receiver functions presented over azimuth are shown in Figure 4a and the harmonic function $H(\theta, t)$ fit to these receiver functions is shown in Figure 4b for comparison. As described in the Appendix, the residual between these functions is used to define the uncertainty, $s(t)$, of the azimuthally independent receiver function and is presented in Figure 4c. The individual harmonic components are shown in Figure 4d-f. The functions $A_1(t)$ and $A_2(t)$ quantify the azimuthally dependent signals that may be produced by tilts on internal interfaces and anisotropy, respectively. Some of these arrivals are observed to undergo a move-out at different azimuths. These functions could be applied to fine-tune the model presented here, but are not currently used for this purpose.

Several examples of the final azimuthally independent receiver functions $A_0(t)$ and associated

1
2
3
4
5
6
7
8
9
10
11
12
13
14
15
16
17
18
19
20
21
22
23
24
25
26
27
28
29
30
31
32
33
34
35
36
37
38
39
40
41
42
43
44
45
46
47
48
49
50
51
52
53
54
55
56
57
58
59
60

uncertainties are shown in [Figure 5](#). The receiver functions display significant station-to-station variations. Those observed at station R11A in the Basin and Range province and station Q22A in the Rocky Mountains have strong P-to-S converted positive amplitude phases between 3 and 7 sec delay time, suggesting a sharp rather than gradient transition from crustal to mantle velocities. The receiver function for TA station T18A in the Colorado Plateau, in contrast, shows no Moho P-to-S conversion, which means that a gradient Moho is probable at this point. The receiver function for station O25A in the Great Plains has a strong negative arrival at ~ 4 sec caused by sedimentary layer reverberations at this location which probably interferes with observation of the Moho conversion.

4. Model Parameterization and Determining the Prior Distribution

4.1 Model parameterization

Surface wave phase velocity curves and azimuthally averaged receiver functions are sensitive to the local average 1-D Vs structure beneath each location. For this reason, the inversion for a 3-D model reduces to a set of 1-D Vs inverse problems. We invert only for shear wave speed in the 200 km beneath the surface (reliable only to about 150 km) because the longest period of surface waves that we use here is 80 sec. Below 200 km, the model is assumed to be constant. Because we use only Rayleigh waves, which are predominantly sensitive to Vsv, we assume an isotropic Vsv model where $V_s = V_{sh} = V_{sv}$. We set the V_p/V_s ratio to 2.0 in the sedimentary layer and 1.75 in the crystalline crust and mantle. The V_p/V_s ratio is important in receiver function analysis and it is discussed further in section 8.1. For density we use the scaling relation (for 10 km) advocated by [Christensen and Mooney \(1995\)](#) in the crust and by [Karato \(1994\)](#) in the mantle. We apply a physical dispersion correction ([Kanamori and Anderson, 1977](#)) using the Q model from PREM ([Dziewonski & Anderson, 1981](#)), and the resulting model is reduced to 1 sec period.

In a traditional surface wave inversion a 1-D model may be parameterized with smooth functions in the crust and mantle ([Megnin and Romanowicz, 2000](#)), as a stack of layers ([Yang and Forsyth, 2006](#)), or a combination of both (e.g., [Shapiro and Ritzwoller, 2002](#), [Moschetti et al., 2010](#), [Yang et al., 2008](#)). Receiver function inversions are, however, typically parameterized with a set of fine layers ([Cassidy, 1992](#), [Julia et al., 2000](#)). We parameterize our model similar to some surface wave inversions in which B-splines represent structure in both the crystalline crust and the

1
2
3 uppermost mantle as follows. (1) There is one sedimentary layer with a linear gradient velocity.
4 Three parameters are used to describe this layer: layer thickness and V_{sv} at the top and bottom of
5 the layer. (2) There is one crystalline crustal layer. Five parameters are used to describe this layer:
6 layer thickness (km) and four B-spline coefficients for V_{sv} . (3) There is one uppermost mantle
7 layer to a depth of 200 km. Five parameters are used to describe this layer: five B-spline
8 coefficients for V_{sv} . The thickness of this layer is controlled by the thicknesses of the top two
9 layers.
10
11

12
13
14
15
16 This model-parameterization contains 13 free parameters (Fig. 6). We explicitly seek vertically
17 smooth models that fit the data. Here, smooth means that the model has no more vertical
18 structure than required to fit the data within a specified tolerance and also that the model is
19 continuous within some depth ranges. In this model parameterization, two discontinuities are
20 introduced because the predominant signals in receiver functions are from the Moho and, in the
21 presence of sediments, from the sediment-basement contact. We demonstrate that a smooth
22 parameterization can explain both the surface wave and receiver function data within data
23 uncertainties across almost the entire study region. In other areas where a discrete higher-
24 velocity lower crustal layer is observed (e.g., immediately north of our study area; Gorman et al.,
25 2002), an additional crustal interface may be needed. The smoothness of the model is imposed by
26 the parameterization so that ad hoc damping is not needed during the inversion.
27
28
29
30
31
32
33
34
35

36 With this model parameterization, we construct the model space in which the prior and posterior
37 distributions are determined. The construction of the model space is based on perturbations to a
38 reference model, where sedimentary structure is taken from Mooney and Kaban (2010), crustal
39 thickness from Bassin et al. (2000), and shear wave speeds in the crust and mantle from Shapiro
40 and Ritzwoller (2002), as summarized in Table 1. At each location models are sampled around
41 the reference in the range prescribed in the table. For example, the crystalline crustal thickness
42 variation is $\pm 25\%$ of the input value. If the reference thickness were 40 km, values would be
43 considered from 30 to 50 km.
44
45
46
47
48
49
50

51 **4.2 Determining the prior distribution**

52 The prior distribution reflects the state of knowledge before data are introduced. Prior
53 information that we apply in choosing models includes the following seven prior assumptions. (1)
54 Models exist in the model space M , which is defined as the reference model subject to allowed
55
56
57
58
59
60

1
2
3 perturbations (Table 1). (2) The model is continuous between V_{sv} discontinuities at the base of
4 the sediments and Moho and is continuous in the mantle. (3) Velocity in the sedimentary layer
5 increases with depth. (4) Velocity in the crystalline crust increases with depth (monotonicity
6 constraint). (5) Velocity contrasts across the sedimentary basement and across the Moho
7 discontinuity are positive. (6) $V_s < 4.9$ km/s throughout the model. (7) When surface wave data
8 are used alone we apply the assumption of a positive velocity gradient in the uppermost mantle.
9 Up to constraint (7), the prior distributions for inversions using only surface wave data or surface
10 wave data jointly with receiver functions are identical. We discuss in section 7.3 how constraint
11 (7) may introduce bias in the estimated model, and how it can be eliminated when receiver
12 functions are introduced. Together, these assumptions reduce model complexity and also
13 ameliorate some of the velocity-depth trade-offs that occur in the surface wave inversion.

14
15 To determine the prior distribution, we perform a random walk in model space with the
16 following steps. First, we initiate the model search at a random point in model space M . If this
17 random point does not obey the assumptions listed above, it is rejected and another random point
18 is chosen. Second, we introduce a random jump in model space. We simultaneously perturb all
19 13 parameters by selecting a new value randomly governed by a Gaussian probability
20 distribution near the old value subject again to the previous assumptions. This Gaussian
21 distribution is controlled by the width of the distribution (standard deviation), which is given in
22 Table 2. These Gaussian widths have been chosen empirically to ensure the efficiency of the
23 random walk in sampling the prior and posterior distributions. If the model produced is not
24 contained in model space M (i.e., does not satisfy the seven constraints in the previous paragraph
25 and does not fall within the ranges presented in Table 1), then the model is rejected and the
26 process re-initiates.

27
28 With a sufficient number of sample points ($> 100,000$), the prior distribution of each parameter
29 can be viewed as histograms of marginal distributions of model characteristics at different depths
30 such as those shown in Figure 7 at the location of the TA station R11A. For this figure we
31 generated V_{sv} models from such parameter distributions by converting the B-spline coefficients
32 to V_{sv} values as a function of depth. Due to the lack of prior information imposed on the
33 thickness of the sedimentary layer or on the thickness of the crystalline crust, the marginal prior
34 distributions of both appear as uniform distributions (Fig. 7a,c). However, the marginal
35 distributions of V_s at different depths are not uniform because different parameters interact
36
37
38
39
40
41
42
43
44
45
46
47
48
49
50
51
52
53
54
55
56
57
58
59
60

1
2
3 through the prior assumptions. The resulting marginal distributions for these variables are more
4 similar to tilted Gaussian patterns because they are affected by prior restrictions to sampling such
5 as the monotonicity constraint on crustal velocities.
6
7
8

9 10 **5. Monte Carlo Inversion of Surface Wave Dispersion Data**

11 In this section, we discuss the Bayesian Monte Carlo inversion based on surface wave data alone
12 for later comparison with the joint inversion with receiver functions, which is presented in
13 section 6. As above, we use the USArray TA station R11A in the Basin and Range province for
14 examples and the input data for the inversion are shown in [Figure 3a](#). At each location, Rayleigh
15 wave phase velocities exist on a fixed discrete grid from 8 to 80 sec period. Prior constraint (7) is
16 not applied in this section.
17
18
19
20
21

22 **5.1 The likelihood functional**

23 For a problem in which the measurements are observed Rayleigh wave phase speeds at a
24 particular location, which have independent but not identically distributed Gaussian
25 observational uncertainties σ_i (period index i), the likelihood functional is computed from
26 equation (2) where the misfit function comes from the first term on the right hand side of
27 equation (5). The assumption of the frequency independence of error processes in surface wave
28 dispersion is made here and in other studies ([Liu et al., 2010](#), [Bodin et al., 2012](#)), because the
29 covariance over frequency is not well understood. The correlation of the dispersion velocities
30 over frequency deserves further investigation.
31
32
33
34
35
36
37
38

39 **5.2 Determining the posterior distribution**

40 The information about model space extracted by introducing the data is described by the
41 posterior distribution. As defined by equation (1), the posterior distribution is the product of the
42 prior distribution and the evaluation of fit to the observed data, which is summarized by the
43 likelihood functional L . During model space sampling, when a new model m_i is generated by
44 perturbing a given model m_j under the prior assumptions, the likelihood functional of this model
45 is calculated through forward computation using the Thomson-Haskell method ([computed using
46 the code of Herrmann, <http://www.eas.slu.edu/eqc/eqccps.html>](#)) with an earth-flattening
47 transformation. Both of the likelihoods $L(m_i)$ and $L(m_j)$ are computed as discussed in section 5.1,
48 where the Metropolis law, equation (4), defines the probability of acceptance for model m_i , as
49 described in section 2.
50
51
52
53
54
55
56
57
58
59
60

Figure 8 shows an example of how the likelihood functional and misfit function of the models accepted during sampling of the posterior distribution evolve for TA station R11A. Accepted models are identified with circles, rejected models are not plotted. The trend shows that after about 100 samples, the likelihood functional will fluctuate near unity during the remaining iterations. We choose to stop iterating after 3000 sampling steps. To ensure that the starting point does not affect the sampling, we initiate the Monte Carlo sampling at ten different random models and the resulting statistics reflect these ten independent samplings. Figure 8 also shows how the RMS misfit function, $\chi = \sqrt{N^{-1}S(m)}$, evolves. When $\chi < 1$, the fit lies within the estimated uncertainties, on average.

As discussed in section 2, an additional model acceptance criterion is introduced as the basis for accepting models to form the posterior distribution. The minimum misfit χ_{\min} is defined as the minimum value of χ found for all models visited during model space sampling. Once χ_{\min} is found, we define the threshold of acceptance χ_{crit} for the surface wave inversion as follows:

$$\chi_{\text{crit}} = \begin{cases} 2\chi_{\min} & \text{if } \chi_{\min} \geq 0.5 \\ \chi_{\min} + 0.5 & \text{if } \chi_{\min} < 0.5 \end{cases} \quad (7)$$

Thus, to define the ensemble of accepted models a posteriori, we accept any model m that is visited during the inversion as long as $\chi(m) \leq \chi_{\text{crit}}$. The choice of the critical threshold level below which models are accepted to form members of the posterior distribution is admittedly ad-hoc and deviates from strict Bayesian practice. Equation (7) succeeds to produce posterior distributions that capture our degree of belief in the final models, however.

From the set of accepted models in the posterior distribution, we compute the distribution of each parameter and the marginal distribution of Vsv at each depth. Figure 9 presents example histograms of marginal distributions for several structural variables derived using surface wave data alone to compare with the prior marginal distributions shown in Figure 7. Typically, the distributions of velocities between boundaries are narrowed. For example, Vsv at 10 km depth in the crust is narrowed; its standard deviation decreases by about a factor of six from ~ 0.3 km/sec to ~ 0.05 km/sec. However, posterior distributions of discontinuity depths (Moho, sediments) or velocity jumps across the discontinuities do not decrease as appreciably. For example, crustal thickness and Vsv contrast across Moho are not changed strongly. These histograms demonstrate

1
2
3 the sensitivity of Rayleigh wave dispersion to V_s structure. (1) Sedimentary thickness does not
4 change because of the lack of very short period (< 8 sec) surface wave dispersion measurements.
5 (2) V_{sv} at 10 km depth shows a much narrower distribution compared with the prior distribution
6 because ambient noise provides information about this depth. (3) The mean of the crustal
7 thickness distribution is about 33 km with a 1σ width of ~ 3.6 km, showing that surface wave
8 dispersion at this location possesses only weak sensitivity to the depth of the Moho discontinuity.
9 The distribution is bimodal and not strongly peaked. (4) The marginal distributions of V_{sv} in the
10 lower crust and the V_{sv} contrast across the Moho are narrowed somewhat but retain considerable
11 uncertainties (0.15-0.2 km/sec) and the lower crustal distribution is also bimodal. (5) V_{sv} in the
12 uppermost mantle (120 km) is narrowed appreciably because the earthquake data are sensitive to
13 this depth, but it is not constrained as well as at 10 km in the crust. This demonstrates that the
14 vertical resolution of surface waves to local structure degrades with depth. Therefore, we only
15 report structure to 150 km. These findings make intuitive sense and are quantified with the
16 posterior distributions.
17
18
19
20
21
22
23
24
25
26
27

28 An alternative view of the results is provided by computing the mean, the median, the 1σ
29 uncertainty, and the full range of V_{sv} at each depth after all accepted models are identified.
30 **Figure 10** shows the resulting extent of accepted models for station R11A. The gray corridors in
31 **Figure 10a,b** outline the extent of all accepted models that fit the data, while the red lines present
32 the 1σ width around the mean model. Note that without assimilating receiver functions, the
33 crustal thickness (Moho depth referenced to the surface in **Fig. 10b**) is not well resolved and the
34 predicted receiver functions (red waveforms in **Fig. 10c**) do not fit the observed azimuthally
35 independent receiver function well, on average. There is also a strong trade-off between the
36 lower crustal velocity and the uppermost mantle velocity. We show in section 6 that these
37 problems are ameliorated with the addition of receiver functions in the inversion.
38
39
40
41
42
43
44
45
46
47

48 **6. Monte Carlo Inversion of Surface Wave Dispersion and Receiver Function Data**

49
50 When receiver functions are assimilated into the Monte Carlo algorithm, the prior distribution of
51 models largely remains the same, although as we discuss in section 7.3 we release the constraint
52 on the positivity of the uppermost mantle velocity gradient. Here, we introduce the joint
53 likelihood functional and then describe the posterior marginal distribution at TA station R11A
54 and then for three other TA stations.
55
56
57
58
59
60

6.1 The joint likelihood functional

The joint likelihood functional is defined by equations (2) and (5), but because we do not know the diagonal elements of the data covariance matrices we need to estimate the relative scaling of the misfits for surface waves and receiver functions that is quantified through parameter κ . We consider values of κ ranging from 1 to 40, and choose 2.5 as a value that strikes the appropriate balance between the two data sets. By choosing this value both data sets are approximately weighted equally in the inversion and the resulting misfits of the two data sets are comparable.

The joint misfit function of equation (5), therefore, becomes:

$$S_{\text{joint}}(m) = S_{SW} + \frac{1}{2.5} S_{RF} = N \chi_{SW}^2 + \frac{M}{2.5} \chi_{RF}^2 = \sum_{i=1}^N \frac{(g_i(m) - D_i^{obs})^2}{\sigma_i^2} + \frac{1}{2.5} \sum_{j=1}^M \frac{(R_j(m) - A_0(t_j))^2}{s_j^2} \quad (8)$$

where we have implicitly defined the χ^2 misfit for surface waves and receiver functions. RMS misfit is the square root of χ^2 .

6.2 Determining the posterior distribution in the joint inversion

Figure 11 shows how the joint likelihood functional for station R11A evolves as model space is sampled. The convergence duration for this sampling is about 500 samples, which requires about five times more models than considered when surface wave data are used alone (Fig. 8). As with the surface wave inversion, we repeat the procedure starting from ten different random points to find the range of models that fit the data acceptably. The forward calculation of receiver functions is based on the code developed by [Shibutani et al. \(1996\)](#), which has also been used by [Sambridge \(1999a\)](#). We introduce for the joint inversion a somewhat different criterion than for the surface wave inversion as the basis for accepting models to form the posterior distribution.

For each location, minimum RMS misfits for surface wave dispersion χ_{\min}^{SW} and receiver functions χ_{\min}^{RF} are identified, although the models that minimize misfits for these two types of data are generally not the same. The joint normalized relative RMS function χ^{joint} is defined as follows:

$$\chi^{\text{joint}} = \frac{1}{2} \left(\frac{\chi^{SW}}{\chi_{\min}^{SW}} + \frac{\chi^{RF}}{\chi_{\min}^{RF}} \right) \quad (9)$$

This function is a combination of relative RMS misfits for the two data sets. The criterion for

model acceptance is $\chi^{\text{joint}} < \chi_{\text{crit}}$, where χ_{crit} is defined as:

$$\chi_{\text{crit}} = \chi_{\text{min}}^{\text{joint}} + 0.5 \quad (10)$$

For example, in the particular inversion for TA station R11A, the minimum misfit for the surface wave data is $\chi_{\text{min}}^{\text{SW}} = 0.51$, the minimum misfit for the receiver function data is $\chi_{\text{min}}^{\text{RF}} = 0.53$, and the minimum misfit to both data in the joint inversion is $\chi_{\text{min}}^{\text{joint}} = 1.15$. Thus, the best fitting model that emerges from the joint inversion does not fit either data type optimally, but fits them both acceptably. In total, about 1000 models are found below the critical threshold $\chi_{\text{crit}} = 1.65$.

Example posterior marginal distributions are plotted and compared with prior (marginal) distributions in [Figure 12](#). All the marginal distributions change shape relative to the prior distributions, especially for Vsv at different depths and for crustal thickness. Compared with the posterior distributions using surface wave data alone ([Fig. 9](#)), the distributions of velocities in the crust and upper mantle change only subtly ([Fig. 12b,f](#)). The other distributions change profoundly. For example, crustal thickness at station R11A sharpens (from $\sigma = 3.6$ km to $\sigma = 1.3$ km). Concerning the velocity difference across the Moho, the mean increases and the standard deviation approximately halves. Such significant changes are expected because receiver functions are most sensitive to velocity contrasts across layer boundaries beneath the station; therefore, the position of the Moho is better determined as are the values of model variables that trade-off with Moho depth in the surface wave inversion.

6.3 Examples of model ensembles

The model ensemble as well as the fit to the data at TA station R11A are shown in [Figure 13](#). The 1σ width is less than half of the full width of the model ensemble, because the Vsv distribution at any depth for the joint inversion is approximately Gaussian except for the sedimentary layer (see [Fig. 12](#)). [Figure 13c](#) presents the azimuthally independent receiver function where the corridor outlined by black lines indicates the uncertainty range. The predicted receiver functions from the ensemble of accepted models are shown with gray lines and the model that fits the receiver function best is shown with the red line. The most prominent signal is the peak at about 4 sec, which is fit quite well. However, the small trough near 2 sec is not fit because doing so would require introducing another crustal discontinuity, which would violate monotonicity. The fact that the algorithm does not automatically adapt the parameterization to accommodate other

1
2
3 discontinuities is discussed further in section 8.2. **Figure 13d** identifies the model that fits the
4 surface wave data best, but the model that fits the receiver function best misfits the surface wave
5 data somewhat between about 40 and 60 sec period. The model that minimizes the joint misfit
6 strikes a balance between these models.
7
8
9

10
11 **Figure 14** presents another example of the joint inversion for station T18A in the Colorado
12 Plateau. In the observed receiver function, no clear peak is found from 3 sec to 8 sec where the
13 Moho P-to-S converted phase would be seen in “normal” receiver functions. After inversion, the
14 receiver function data is well fit without a P-to-S converted arrival based on the model ensemble
15 shown in **Figure 14b**. The Moho discontinuity is not well defined in the ensemble of models and
16 V_{sv} changes smoothly from the lower crust to the uppermost mantle.
17
18
19
20

21
22 **Figure 15** summarizes the joint inversion result for station Q22A in the Colorado Rocky
23 Mountains. In the observed receiver function, a peak at about 6 sec suggests that the Moho is
24 deeper than at station R11A in the Basin and Range province. As a result, the crustal thickness
25 distribution is centered at about 49 km depth with an uncertainty of 2.3 km. The relatively small
26 uncertainty of crustal thickness generates a sharp transition between the lower crust and
27 uppermost mantle, particularly compared with station T18A in the Colorado Plateau.
28
29
30
31

32
33 **Figure 16** shows the joint inversion result for station O25A in a sedimentary basin, the Denver
34 Basin region of the Great Plains. The peak at 1 sec on the receiver function and the trough at 4
35 sec indicate a thick sedimentary layer at shallow depths. After inversion, a thick sedimentary
36 layer (~4 km) with a strong vertical velocity gradient is found and the crustal thickness is
37 estimated to be 51.1 ± 3.9 km. Signatures in receiver functions that are common for sedimentary
38 basins are a broadened direct P-pulse or an apparent lack of a direct P-arrival at zero delay time
39 followed by a large amplitude arrival in the first second or so – the latter feature being due to
40 bending to vertical incidence and a strong conversion to shear energy at the sediment-basement
41 contact. The high-amplitude apparent mid-crustal negative arrival is modeled here as a
42 reverberation within the sedimentary basin with two shear and one compressional legs within the
43 sediment layer. The constraint of monotonically increasing velocities within the crust aids
44 suppression of sediment multiples in favor of imaging true deeper crustal structure. In a few
45 other locations in which there are true mid-crustal low-velocity layers, such as the Rocky
46 Mountain location shown in **Figure 15**, this may suppress a true feature, however. Extreme
47
48
49
50
51
52
53
54
55
56
57
58
59
60

1
2
3 examples may be magma chambers (e.g., Wilson, 2003). V_{sv} in the sediments at O25A increases
4 from less than 1 km/sec to more than 3 km/sec at depth of ~ 3 km, representing the compaction of
5 sediments in this layer. V_{sv} in the upper crust is ~ 3.4 km/sec and reaches higher than 4 km/sec in
6
7 sediments in this layer. V_{sv} in the upper crust is ~ 3.4 km/sec and reaches higher than 4 km/sec in
8
9 the lower crust, perhaps indicating a mafic lower underplated crust (“7.x layer”) that has been
10 proposed for parts of the High Plains (e.g. Gorman *et al.*, 2002). A fast lithosphere (>4.5 km/sec)
11 is observed in the upper mantle.
12
13

14 **7. Systematic Application of the Joint Inversion Across the Intermountain West**

15
16
17 In previous sections, the joint Bayesian Monte Carlo inversion of surface wave dispersion and
18 receiver functions was shown to estimate reasonable 1-D models with attendant uncertainty
19 information for stations situated in a wide variety of structural environments. We now report on
20 the application of the joint inversion method to the 185 TA stations across the intermountain west
21 (Fig. 1).
22
23
24
25

26 **7.1 Construction of a 3-D V_{sv} model for the Intermountain West**

27
28 We apply the Monte Carlo inversion to the 185 stations shown in Figure 1. For each joint
29 inversion, we identify the model from the resulting model ensemble that fits the surface wave
30 data (SW) or receiver functions (RF) best as the SW or RF best fitting model, respectively. The
31 misfits to SW data by the SW best fitting models for the stations tested are plotted with the white
32 histogram in Figure 17a, while the misfits to the RFs by the RF best fitting models are plotted in
33 Figure 17b. For each station, the model with minimum joint misfit is identified, and is called the
34 joint best fitting model. Misfits to SW and RF data from the joint best fitting models are shown
35 in Figure 17 with red histograms. At most stations, the joint best fitting models fit the SW or RF
36 data only slightly worse than the model that fits each single data type best. This indicates that
37 there is some tension in fitting the two data types. Second, the joint best fitting models have a
38 misfit < 1 for both data sets for almost all stations, which indicates that the simple model
39 parameterization that we use in the joint inversion can reproduce the RFs with misfits below the
40 RF uncertainties for most of the stations tested. Third, larger RF misfits appear for stations near
41 the corner of Utah/Colorado/Wyoming and are sparsely distributed through the Basin and Range.
42 The RFs at those stations have sharp back-azimuthal variations that vitiate the harmonic
43 stripping method’s attempt to estimate an azimuthally independent receiver function. Cases with
44 sharp back-azimuthal signals in the RFs are discussed further in the Appendix, but in these cases
45
46
47
48
49
50
51
52
53
54
55
56
57
58
59
60

the uncertainty in the receiver function increases substantially and the inversion reverts for the most part to fitting surface wave data. Fewer than three stations show a large misfit (>0.9) to surface wave data and these stations are sparsely distributed across the map. Finally, the comparable minimum and joint misfits for the two data sets also indicate that neither data set is over-weighted during the inversion.

After inversion is performed at all stations, we obtain Vsv model ensembles beneath the 185 stations with means and uncertainties at all depths. The distribution of stations forms an irregular grid. To produce a smooth Vsv model on a regular grid, simple kriging (Schultz *et al.*, 1999) interpolation is applied to smooth the Vsv values at each depth based on the mean value at that depth and the estimated uncertainties. For a given depth, at each grid node we search for stations within a 1-degree radius. We weight the average Vsv of the model ensemble for at given station using a weighting function defined as follows:

$$W_i = \begin{cases} \frac{1}{(1 + d_i)\sigma_i} & \text{if } d_i \leq 1^\circ \\ 0 & \text{otherwise} \end{cases} \quad (11)$$

where d_i and σ_i denote the distance to station i from the grid node and the uncertainty of the model at the specified depth for that station, respectively. By performing this simple-kriging interpolation, map views of the 3-D model on a $0.25^\circ \times 0.25^\circ$ spatial grid are produced.

7.2 Characteristics of the 3-D model

In the upper crust (10 km depth, Figure 18a), high velocities are observed beneath the Colorado Plateau and Great Plains, while the Rocky Mountains show low Vsv. Near the northern boundary of the Colorado Plateau low velocities are also observed, presumably caused by very thick sediments in the Green River Basin, Uinta Basin, etc. At these locations, the maximum allowed sediment thickness may be less than the true thickness, leading to smearing of low velocities into the upper portion of the crystalline crustal layer. In contrast, the Denver Basin is much thinner than 10 km and the structure there is well constrained by receiver function data. Uncertainties at 10 km depth are approximately homogeneous across the region, averaging about 27 m/s, which is about 0.8%.

In the lower crust (averaged from 4 km above the Moho to the Moho, Fig. 18c), the most prominent feature is the slow anomaly (<3.6 km/sec) encompassing the eastern Basin and Range

1
2
3 province near the northwestern Colorado Plateau. Slow lower crust is found across the entire
4 Basin and Range and also near the western edge of the Rocky Mountain province in
5 southwestern Colorado. There is coincidence between the ~ 3.85 km/sec V_{sv} contour and the
6 eastern Rocky Mountain topographic high in Colorado, implying a strong relationship between
7 topography and crustal structure. A fast lower crustal anomaly extends through the Colorado
8 Great Plains and southern Wyoming and also penetrates into the Colorado Plateau. Uncertainties
9 are larger and more variable in the lower crust (Fig. 18d) than the upper crust, ranging from
10 about 40 m/s in parts of the Colorado Plateau to more than 160 m/s in the Rocky Mountains of
11 southern Colorado. Higher uncertainties have two causes. First, they appear where there is a
12 large jump in velocities across the Moho, due to a trade-off between Moho depth and uppermost
13 mantle structure. The trade-off has been ameliorated but not entirely eliminated through the
14 addition of receiver functions in the inversion. Second, larger uncertainties also occur where
15 receiver functions have a larger uncertainty in the amplitude of P-to-S conversions.

16
17
18
19
20
21
22
23
24
25
26
27 At 60 km depth (Fig. 18e), which is in the uppermost mantle across the region, a strong contrast
28 is observed between the eastern and western sides of the study region. A strong anomaly as low
29 as 4.0-4.1 km/s is seen at the eastern edge of the Basin and Range, which may be related to the
30 Cenozoic magmatism in this region (Roy *et al.*, 2009). Much higher velocities are observed
31 beneath the Great Plains, reaching up to 4.8 km/s. Uncertainties are largely homogeneous across
32 the study region, averaging about 50 m/s (Fig. 18f). At a depth of 120 km (Fig. 18g), V_{sv}
33 beneath the Great Plains is very high, but the strongest high velocity anomaly is detected beneath
34 the Wyoming Craton in southern Wyoming. This high velocity feature continues beneath the
35 Colorado Plateau, suggesting a strong, thick lithosphere beneath the northern Colorado Plateau
36 except for its northwestern periphery. The Basin and Range and Rocky Mountains show
37 relatively homogeneous low V_{sv} compared with other regions. Uncertainties (Fig. 18h) are
38 fairly homogeneous and average about 65 m/s ($< 1.5\%$) across the entire study region.
39
40
41
42
43
44
45
46
47
48
49
50
51
52
53
54
55
56
57
58
59
60
Uncertainties are larger deeper in the mantle (120 km versus 60 km) because the surface wave
dispersion information is less sensitive to deeper structure.

7.3 Changes in the 3D model compared with the surface wave inversion

There are several significant advantages to adding receiver functions to surface wave dispersion
data in the Monte Carlo inversion. We focus on three topics: (1) determining crustal thickness

1
2
3 and uncertainties, (2) determining the velocity jump across the Moho, and (3) constraining
4 uppermost mantle structure.
5
6

7
8 By utilizing receiver functions in the inversion, there is a natural increase in the accuracy of
9 estimates of Moho depth or crustal thickness. This is apparent on comparison between the
10 crustal thickness distribution for station R11A from the inversion with surface wave data alone
11 and that from the joint inversion of both data sets (Fig. 9c and Fig. 12c). This observation holds
12 for all stations with clear P-to-S converted signals. Figure 19a,b presents crustal thickness and
13 associated uncertainties from inverting surface wave dispersion data alone. The uncertainty level
14 scales with crustal thickness and is ~ 5 km on average with smaller values in the Basin and
15 Range and larger values in the Great Plains. In contrast, crustal thickness and uncertainty
16 determined from the joint inversion appears in Figure 19c,d. The uncertainty level from the joint
17 inversion decreases in the Basin and Range, the central Rocky Mountains and parts of the Great
18 Plains, where P-to-S converted phases are well observed. In the northern part of the Colorado
19 Plateau and southern Wyoming craton where thick sediments exist, crustal thickness
20 uncertainties are not reduced by adding receiver functions or may even increase where the P-to-
21 S signals in the receiver functions are muted by sedimentary reverberations. In addition to
22 improving the determination of Moho depth, receiver functions also help to determine whether a
23 sharp Moho discontinuity exists or not. An example is shown in the inversion at station T18A in
24 the Colorado Plateau (Fig. 14), where the raw receiver function has no dominant arrival from 3
25 sec to 7 sec where a P-to-S conversion should appear. The joint Monte Carlo inversion thus
26 produces a model that has a gradient in V_{sv} at the depth where Moho is expected. The resulting
27 crustal thickness distribution has larger uncertainty than when a clear P-to-S phase is observed,
28 but none of the models in the distribution shows a sharp Moho.
29
30
31
32
33
34
35
36
37
38
39
40
41
42
43
44

45 Second, introducing receiver functions improves the determination of the V_{sv} contrast across the
46 Moho, which is related to the amplitude of the P-to-S phase in the receiver functions. For
47 instance, the receiver function at station R11A (Fig. 13) shows a strong Moho conversion while
48 the converted phase in the receiver function at T18A is weak, resulting in a V_{sv} contrast at Moho
49 that is stronger at R11A than at T18A (or perhaps a gradational crust-mantle transition at station
50 T18A). A map of the V_{sv} contrast and uncertainty across the region is shown in Figure 19e,f.
51
52
53
54
55
56
57
58
59
60 The features shown are coherent with geological province. A high V_{sv} contrast across Moho is
observed beneath the Basin and Range as well as parts of the Rocky Mountains and the Great

1
2
3 Plains east of the Denver Basin. In contrast, beneath the Colorado Plateau, especially under the
4 northwestern Colorado Plateau, the V_{sv} contrast is very low. This feature is consistent with
5 observations made by earlier studies (Sheehan *et al.*, 1997, Gilbert and Sheehan, 2004, Levander
6 *et al.*, 2011, Bailey *et al.*, 2012). Beneath the southern Wyoming Craton, we observe a small
7 Moho V_{sv} contrast as well as high uncertainties in crustal thickness and thick sediments. This is
8 because sedimentary reverberations dominate the receiver function where a Moho peak would be
9 expected and the V_{sv} contrast across Moho is difficult to resolve. Uncertainties in the velocity
10 contrast across Moho range between about 80 m/s to 160 m/s, being smallest in the Colorado
11 Plateau where the V_{sv} contrast is low in all accepted models.
12
13
14
15
16
17
18

19
20 The third advantage of the joint inversion method is a better determination of mantle structure
21 below the Moho discontinuity. This is largely due to reduction of the trade-off between Moho
22 depth and lower crustal velocity. Because of this trade-off, when surface wave dispersion is used
23 alone to invert for a 3-D model, a prior constraint is often applied on the vertical velocity
24 gradient in the uppermost mantle. For example, several studies have set the V_{sv} gradient in the
25 uppermost mantle to be positive (Yang *et al.*, 2008, Moschetti *et al.*, 2010, Zheng *et al.*, 2011).
26 **Figure 20** shows the result of various upper mantle constraints along the transect identified in
27 **Figure 1**. In the model constructed by using surface wave data alone with an imposed positive
28 V_{sv} gradient in the uppermost mantle (**Fig. 20a**), a slow anomaly belt is found immediately
29 beneath the Moho. In contrast, if the constraint is changed in sign so that a negative V_{sv} gradient
30 is imposed, a fast anomaly belt is observed (**Fig. 20b**). These two models show differences down
31 to depths of more than 100 km and the placement of anomalies in depth is affected strongly.
32 Lithospheric thickness and the depth to prominent asthenospheric anomalies are both changed by
33 varying this constraint. However, both models fit the surface wave data equally well, which
34 indicates that the surface wave data alone cannot distinguish between them. **Figure 20c** shows
35 the model constructed from the joint inversion of surface wave dispersion and receiver function
36 data with no constraint on the uppermost mantle velocity gradient. The result looks like a
37 combination of **Figures 20a** and **20b**. Beneath the Basin and Range where the Moho is prominent
38 and the V_{sv} contrast across Moho is large, the model is more similar to **Figure 20b** constructed
39 with a negative gradient constraint in the uppermost mantle. However, in places where a gradient
40 Moho is expected, the model is more similar to models from the positive gradient constraint,
41 **Figure 20a**. The assimilation of receiver functions in the inversion resolves the velocity-depth
42
43
44
45
46
47
48
49
50
51
52
53
54
55
56
57
58
59
60

1
2
3 trade-off with data rather than with ad hoc prior constraints.
4

5 **8. Discussion**

6 **8.1 Sensitivity to the V_p/V_s ratio**

7
8
9
10 Rayleigh wave phase velocity dispersion curves are only weakly sensitive to V_p compared to V_s ;
11 hence, the V_p/V_s ratio is usually a fixed parameter in the inversion of surface wave data.

12
13 However, the V_p/V_s ratio is important in receiver function analysis because it is needed to map
14 the P-to-S conversion time delay to depth. The V_p/V_s ratio can be determined when Moho
15 reverberations such as the PpPs or PsPs phases are used as discussed by [Zhu and Kanamori](#)
16 [\(2000\)](#). However, these phases arrive later than the 10 sec time window used here in the Monte
17 Carlo inversion. We omit these phases from consideration because at many locations in the
18 western US Moho reverberations cannot be isolated cleanly due to lateral heterogeneity (e.g., the
19 large scatter in the results of [Lowry and Perez-Gussinye, 2011](#), Fig. 2a) and in some places a
20 gradational crust-mantle transition. Rayleigh wave ellipticity and local amplification may also
21 potentially be used to constrain the crustal V_p/V_s ratio ([Lin et al. 2012a,b](#)). However, this is
22 beyond of the scope of this study.
23
24
25
26
27
28
29
30

31
32 Because we ignore crustal reverberation phases, we are unable to determine the three relevant
33 parameters (V_s in the crust, crustal thickness, and V_p/V_s ratio) simultaneously. To demonstrate
34 this result, we add an extra degree of freedom to the model space, the V_p/V_s ratio in the
35 crystalline crust, which we allow to vary between 1.65 and 1.85 during the inversion. First, the
36 posterior distribution of the V_p/V_s ratio as well as its prior distribution are plotted in [Figure 21a](#).
37 The posterior distribution of the V_p/V_s ratio does not center at any particular value. Second, once
38 the V_p/V_s ratio is introduced as a variable in the inversion, the posterior distribution of the
39 crustal thickness broadens ([Fig. 21b](#)) about 20% compared with the same posterior distribution
40 from the inversion with fixed V_p/V_s ratio ([Fig. 12c](#)) from 1.4 km to ~ 1.7 km. Finally, we
41 observe a strong trade-off between crustal thickness and the V_p/V_s ratio ([Fig. 21c](#)), which
42 indicates that given a higher V_p/V_s ratio the estimated crustal thickness will be lower and vice
43 versa.
44
45
46
47
48
49
50
51
52

53
54 The fact that we are unable to determine a preferred V_p/V_s ratio from our data at station R11A
55 also holds for other stations. [Figure 21d-f](#) shows the posterior distributions of V_p/V_s ratio at
56 stations T18A in CP, Q22A in RM, and O25A in GP, respectively. Overall, we poorly constrain
57
58
59
60

1
2
3 the V_p/V_s ratio from the data we are using. The direct effect is that when we present the 3-D
4 model in section 7.2, the uncertainty of crustal thickness is under-estimated by up to $\sim 20\%$ due
5 to the fact that the V_p/V_s ratio is set to 1.75. To improve the determination of the V_p/V_s ratio,
6 other information such as reverberation phases arriving after 10 sec in the receiver functions and
7 Rayleigh wave ellipticity and local amplification (Lin et al., 2012a, b) would have to be included
8 in the Monte Carlo sampling.
9
10
11
12
13

14 **8.2 Limitations of the current method and potential refinements**

15
16
17 The procedure that we have developed is intended to provide a practical method to invert surface
18 wave dispersion and receiver functions jointly over large areas. As it currently exists, the method
19 can be applied fruitfully across large arrays that have been developed around the globe. This
20 includes all of the USArray in the US, as well as the Chinese Earthquake Array, the Virtual
21 European Seismic Network, various PASSCAL experiments around the world, and F-net in
22 Japan. However, the method also serves as a framework for future enhancements and
23 improvements. In this regard we highlight four known limitations with the method as it is
24 currently effected that may call for modification. A fifth limitation is discussed in section 8.1
25 regarding a variable V_p/V_s ratio.
26
27
28
29
30
31
32

33
34 First, the parameterization that we have defined is applied rigidly in the inversion. The algorithm
35 has not been designed to sense misfit to the data and to adapt the parameterization accordingly,
36 although other recent joint inversion algorithms include this feature (e.g., Bodin et al., 2011). For
37 instance, in the inversion at station R11A (Fig. 13), a mid-crustal discontinuity was
38 not introduced automatically to fit the negative arrival at ~ 1 sec on the receiver function. An
39 adaptive parameterization would help the algorithm fit aspects of the data that are currently being
40 ignored, but introducing more structure would increase uncertainties and may lead to over-
41 interpretation of the data.
42
43
44
45
46
47

48
49 Second, the travel time variation of P-to-S conversions due to dipping interfaces (notably on the
50 Moho) is not fit in our inversion and is removed in the harmonic stripping algorithm to estimate
51 the azimuthally independent receiver function that we use in the joint inversion, $A_0(t)$. Not
52 modeling the delay time variation explicitly means that the amplitude of P-to-S conversions will
53 be underestimated if the variation is significant (i.e., ≥ 0.5 sec). The delay time variation does
54
55
56
57
58
59
60

1
2
3 appear in the $A_1(t)$ and $A_2(t)$ components of the receiver function that are estimated in the
4 harmonic stripping algorithm but which are not used in the inversion. Optimally, the algorithm
5 would employ information that exists in these two components to correct for the underestimation
6 of the amplitude of the phase conversions from dipping interfaces. In principle, this information
7 as well as transverse component receiver function amplitudes and delay time variations could
8 also be used to estimate the dip on the interfaces, but this information would probably have to be
9 interpreted independently from surface wave data.

10
11
12 Third, we do not use the receiver function (RF) produced from a multi-station imaging technique
13 (e.g., the Common Conversion Point (CCP) stacked receiver function) but rather a single-station
14 RF which is an average of the 3-D variation near each single station. In the future, this procedure
15 could be replaced with the receiver function stacked at the common conversion point (CCP)
16 rather than at the station. This procedure is inappropriate for the TA because the CCPs beneath
17 nearby stations do not overlap, as [Figure 22a](#) illustrates. The procedure would be appropriate for
18 a denser array such as PASSAL or EarthScope Flexible Array experiments. [Figure 22b](#) also
19 presents a comparison between RFs computed using the TA and the CD-ROM PASSCAL
20 experiment. The blue RFs are from three TA stations along the green transect in [Figure 22a](#), and
21 the red RFs are binned CD-ROM+TA RFs produced according to the Moho Conversion Points
22 (MCP), where radial receiver functions that pierce the same bin at Moho depth are averaged
23 laterally. The similarity between MCP RFs and the harmonic stripping $A_0(t)$ RFs demonstrate
24 that the single station azimuthally independent RFs that we construct are consistent with the multi-
25 station RFs. A smoothed image of the multi-station RFs is presented in [Figure 22c](#),
26 demonstrating the resolution that RFs from a tighter network geometry provide. Higher
27 resolution features such as the mid-crustal signal at ~ 2.5 sec beneath the Cheyenne Belt
28 (CB) are not captured by the sparse TA array. However, using higher resolution RFs would
29 necessitate accommodating the lower resolution of surface wave dispersion maps so as not to
30 alias sharp features from the RFs into larger scale features derived in the joint inversion. It
31 remains unclear what maximum resolution may be possible for surface waves from a tighter
32 array spacing than the TA, for example from the Flexible Array component of USArray. It is
33 likely, however, that surface wave resolution will always lag resolution from receiver functions.
34 Although the installation of the TA has ameliorated the differential resolution problem in the US,
35 the issue may ultimately need to be resolved by low-pass filtering the RFs.

36
37
38
39
40
41
42
43
44
45
46
47
48
49
50
51
52
53
54
55
56
57
58
59
60

1
2
3 Fourth, the full error covariance matrices for surface wave dispersion data and receiver functions
4 have not been utilized here. Rather, we have assumed that the matrices are diagonal (errors are
5 independent) and have balanced the two data sets by introducing a scaling parameter (κ) that
6 effectively normalizes the misfit found for the two data sets. Estimating the inverse covariance
7 matrix for both data sets is not trivial, but it would improve the effectiveness of the algorithm.
8
9

10 11 12 **9. Conclusions**

13
14 We present a new method for joint inversion of surface wave dispersion data and receiver
15 functions based on a Bayesian Monte Carlo scheme. When applied to receiver functions and
16 surface wave data from ambient noise and earthquakes that are now emerging from extended
17 broadband seismic arrays, the method produces a 3-D model of the crust and uppermost mantle
18 to a depth of about 150 km with associated uncertainties. The method is designed to be used in
19 an automated fashion across a large number of stations and has been applied to data from 185
20 USArray Transportable Array (TA) stations in a geologically diverse part of the Intermountain
21 West. The effect of the introduction of receiver functions to surface wave dispersion data is
22 visualized through improvements in the posterior marginal distribution of model variables. By
23 comparing the statistics of the posterior distributions, we find that adding receiver function data
24 quantitatively improves the accuracy of estimates of Moho depth, improves the determination of
25 the V_{sv} contrast across Moho, and improves uppermost mantle structure. Knowledge of
26 uppermost mantle structure is improved because the assimilation of receiver function data makes
27 it possible to relax ad-hoc structural constraints that are commonly invoked in inversions based
28 on surface wave data alone.
29
30
31
32
33
34
35
36
37
38
39
40
41

42 Although the inversion method we describe can be applied robustly across large regions, there
43 remain aspects of the method where refinements may prove beneficial. Three are particularly
44 noteworthy: (1) development of an adaptive parameterization, particularly in the crust where low
45 velocity layers may exist, (2) further investigation of the estimation of the full data covariance
46 matrix and its inverse for both receiver functions (covariance over time) as was done by *Bodin et*
47 *al. (2011)* and surface wave dispersion (covariance over frequency), (3) extension of the receiver
48 functions past 10 sec to recover reverberations that may help to constrain the V_p/V_s ratio. These
49 and other potential refinements to the method may reduce small biases that derive from current
50 assumptions, but the current method produces results that are preferable to the use of surface
51
52
53
54
55
56
57
58
59
60

1
2
3 wave dispersion or receiver function data alone.
4
5
6

7 **Acknowledgments.** The authors gratefully acknowledge insightful reviews from Thomas Bodin,
8 Malcolm Sambridge, an anonymous reviewer, and the Associate Editor, Gabi Laske, that helped
9 to improve this paper. They are also grateful to Craig Jones for insights into receiver function
10 analyses and to Anne Sheehan for discussions concerning the history of joint inversions with
11 receiver functions and surface wave dispersion. The facilities of the IRIS Data Management
12 System, and specifically the IRIS Data Management Center, were used to access the waveform
13 and metadata required in this study. The IRIS DMS is funded through the National Science
14 Foundation and specifically the GEO Directorate through the Instrumentation and Facilities
15 Program of the National Science Foundation under Cooperative Agreement EAR-0552316. This
16 research was supported by NSF grants EAR-0711526, EAR-0844097, EAR-0750035, and
17 EAR-1053291 at the University of Colorado at Boulder. F.-C. Lin is supported by the Director's
18 Post-Doctoral Fellowship of the Seismological Laboratory at the California Institute of
19 Technology.
20
21
22
23
24
25
26
27
28
29
30
31
32
33
34
35
36
37
38
39
40
41
42
43
44
45
46
47
48
49
50
51
52
53
54
55
56
57
58
59
60

Table 1. Model space and references.

Model Parameters	Range	Reference
Sediment thickness	$0-2\mathbf{m}_0$ (km)	Mooney and Kaban (2010)
Crystalline crustal thickness	$\mathbf{m}_0 \pm 0.25\mathbf{m}_0$ (km/s)	Bassin, C. <i>et al.</i> (2000)
Vsv, top of sedimentary layer	$\mathbf{m}_0 \pm 0.2\mathbf{m}_0$ (km/s)	Bassin, C. <i>et al.</i> (2000)
Vsv, bottom of sedimentary layer	$\mathbf{m}_0 \pm 0.2\mathbf{m}_0$ (km/s)	Bassin, C. <i>et al.</i> (2000)
B-spline coefficients, crust	$\mathbf{m}_0 \pm 0.2\mathbf{m}_0$ (km/s)	Shapiro and Ritzwoller (2002)
B-spline coefficients, mantle	$\mathbf{m}_0 \pm 0.2\mathbf{m}_0$ (km/s)	Shapiro and Ritzwoller (2002)

Table 2. Width of the Gaussian distribution in the model perturbation.

Parameters	Gaussian Width
Thickness, sedimentary layer	0.1 km
Thickness, crystalline crust layer	1 km
B-spline coefficients, crust	0.05 km/sec
B-spline coefficients, mantle	0.05 km/sec
Velocity at top/bottom of sedimentary layer	0.05 km/sec

Table A1. Horizontally-layered isotropic model M_0

Layer	Vsv (m/sec)	Vp (m/sec)	Density (kg/m^3)	Thickness (km)
1	3500	6125	2746	45
2	4300	7525	3350	~

References

- Abers, G. A. (1998), Array measurements of phases used in receiver-function calculations: Importance of scattering, *Bulletin of the Seismological Society of America.*, 88, 313-318
- Ammon, C. J., G. E. Randall, and G. Zandt (1990), On the nonuniqueness of receiver function inversions, *J. Geophys. Res.*, 95(B10), 15,303–15,318, doi:10.1029/JB095iB10p15303.
- Ammon, C.J. & Zandt, G. (1993), Receiver structure beneath the southern mojave block, California, *Bulletin of the Seismological Society of America*, 83, 737-755.
- An, M., and M. S. Assumpção (2004), Multi-objective inversion of surface waves and receiver functions by competent genetic algorithm applied to the crustal structure of the Paraná Basin, SE Brazil, *Geophys. Res. Lett.*, 31, L05615, doi:10.1029/2003GL019179.
- Bailey, I. W., M. S. Miller, K. Liu, and A. Levander (2012), V_S and density structure beneath the Colorado Plateau constrained by gravity anomalies and joint inversions of receiver function and phase velocity data, *J. Geophys. Res.*, 117, B02313, doi:10.1029/2011JB008522.
- Bannister, S., Yu, J., Leitner, B. & Kennett, B.L.N., (2003). Variations in crustal structure across the transition from West to East Antarctica, Southern Victoria Land, *Geophysical Journal International*, 155, 870-884.
- Bassin, C., Laske, G. and Masters, G., The Current Limits of Resolution for Surface Wave Tomography in North America, (2000). EOS Trans AGU, 81, F897.
- Basuyau, C. & Tiberi, C. (2011), Imaging lithospheric interfaces and 3D structures using receiver functions, gravity, and tomography in a common inversion scheme, *Computers & Geosciences*, 37, 1381-1390.
- Bensen, G.D., Ritzwoller, M.H., Barmin, M.P., Levshin, A.L., Lin, F., Moschetti, M.P., Shapiro, N.M. & Yang, Y., (2007). Processing seismic ambient noise data to obtain reliable broad-band surface wave dispersion measurements, *Geophysical Journal International*, 169, 1239-1260.
- Bensen, G.D., M.H. Ritzwoller, and Y. Yang (2009), A 3D shear velocity model of the crust and uppermost mantle beneath the United States from ambient seismic noise, *Geophysical*

- 1
2
3 *Journal International*, 177(3), 1177-1196.
4
5
6 Bianchi, I., J. Park, N. Piana Agostinetti, and V. Levin (2010), Mapping seismic anisotropy using
7 harmonic decomposition of receiver functions: An application to Northern Apennines,
8 Italy, *J. Geophys. Res.*, 115, B12317, doi:10.1029/2009JB007061.
9
10
11 Bodin, T., M. Sambridge, H. Tkalčić, P. Arroucau, K. Gallagher, and N.
12 Rawlinson (2012), Transdimensional inversion of receiver functions and surface wave
13 dispersion, *J. Geophys. Res.*, 117, B02301, doi:10.1029/2011JB008560.
14
15
16
17 Bostock, M. G. (1998), Mantle stratigraphy and evolution of the Slave province, *J. Geophys.*
18 *Res.*, 103(B9), 21,183–21,200, doi:10.1029/98JB01069.
19
20
21
22 Cassidy, J. F. (1992), Numerical experiments in broad-band receiver function-analysis, *Bulletin*
23 *of the Seismological Society of America*, 82(3), 1453-1474.
24
25
26 Chang, S.J., Baag, C.E. & Langston, C.A. (2004), Joint analysis of teleseismic receiver functions
27 and surface wave dispersion using the genetic algorithm, *Bulletin of the Seismological*
28 *Society of America*, 94, 691-704.
29
30
31
32 Christensen, N.I. & Mooney, W.D. (1995), Seismic velocity structure and composition of the
33 continental crust: A global view, *J. Geophys. Res.*, 100(B6): 9761–9788.
34
35
36 Clitheroe, G., O. Gudmundsson, and B. L. N. Kennett (2000), The crustal thickness of
37 Australia, *J. Geophys. Res.*, 105(B6), 13,697–13,713, doi:10.1029/1999JB900317.
38
39
40
41 Croftwell, H. P., and T. J. Owens (2005), Automated receiver function processing, *Seismological*
42 *Research Letters*, 76(6), 702-709.
43
44
45 Du, Z.J. & Foulger, G.R., (1999). The crustal structure beneath the northwest fjords, Iceland,
46 from receiver functions and surface waves, *Geophysical Journal International*, 139, 419-432.
47
48
49 Dziewonski, A. and D. Anderson (1981), Preliminary reference Earth model, *Phys. Earth Planet.*
50 *Int.*, 25(4): 297–356.
51
52
53 Endrun, B., Meier, T., Bischoff, M. & Harjes, H.P. (2004), Lithospheric structure in the area of
54 Crete constrained by receiver functions and dispersion analysis of Rayleigh phase velocities,
55 *Geophysical Journal International*, 158, 592-608.
56
57
58
59
60

- 1
2
3
4
5
6
7
8
9
10
11
12
13
14
15
16
17
18
19
20
21
22
23
24
25
26
27
28
29
30
31
32
33
34
35
36
37
38
39
40
41
42
43
44
45
46
47
48
49
50
51
52
53
54
55
56
57
58
59
60
- Frederiksen, A.W., Folsom, H. & Zandt, G., (2003). Neighbourhood inversion of teleseismic Ps conversions for anisotropy and layer dip, *Geophysical Journal International*, 155, 200-212.
- Gilbert, H. J., and A. F. Sheehan (2004), Images of crustal variations in the intermountain west, *J. Geophys. Res.*, 109, B03306, doi:10.1029/2003JB002730.
- Girardin, N. and V. Farra (1998), Azimuthal anisotropy in the upper mantle from observations of P-to-S converted phases: application to southeast Australia, *Geophysical Journal International*, 133, 615-629.
- Gok, R., Pasyanos, M.E. & Zor, E. (2007), Lithospheric structure of the continent-continent collision zone: eastern Turkey, *Geophysical Journal International*, 169, 1079-1088.
- Gorman, A. R., Clowes, R. M., Ellis, R. M. et al., (2002), Deep Probe: Imaging the roots of western North America, *Can. Journ. Earth Sci.*, 39(3), 375-398.
- Hetenyi, G. & Bus, Z., (2007). Shear wave velocity and crustal thickness in the Pannonian Basin from receiver function inversions at four permanent stations in Hungary, *Journal of Seismology*, 11, 405-414.
- Horspool, N.A., Savage, M.K. & Bannister, S. (2006), Implications for intraplate volcanism and back-arc deformation in northwestern New Zealand, from joint inversion of receiver functions and surface waves, *Geophysical Journal International*, 166, 1466-1483.
- Jones, C. H., and R. A. Phinney (1998), Seismic structure of the lithosphere from teleseismic converted arrivals observed at small arrays in the southern Sierra Nevada and vicinity, California, *J. Geophys. Res.*, 103(B5), 10,065–10,090, doi:10.1029/97JB03540.
- Julia, J., Ammon, C.J. & Herrmann, R.B. (2003), Lithospheric structure of the Arabian Shield from the joint inversion of receiver functions and surface-wave group velocities, *Tectonophysics*, 371, 1-21.
- Julia, J., Ammon, C.J., Herrmann, R.B. & Correig, A.M. (2000), Joint inversion of receiver function and surface wave dispersion observations, *Geophysical Journal International*, 143, 99-112.
- Kanamori, H. and D. Anderson (1977), Importance of physical dispersion in surface wave and free oscillation problems : Review, *Revs. Geophys. Space Phys.*, 15(1):105-112.

- 1
2
3 Karato, S. (1993), Importance of anelasticity in the interpretation of seismic
4 tomography, *Geophys. Res. Lett.*, 20(15), 1623–1626, doi:10.1029/93GL01767.
5
6
7 Khan, A., Zunino, A. and Deschamps, F. (2011) The thermo-chemical and physical structure
8 beneath the North American continent from Bayesian inversion of surface-wave phase
9 velocities, *J. Geophys. Res.*, 116, B09304, doi:10.1029/2011JB008380.
10
11
12 Langston, C. A. (1979), Structure Under Mount Rainier, Washington, Inferred From Teleseismic
13 Body Waves, *J. Geophys. Res.*, 84(B9), 4749–4762, doi:10.1029/JB084iB09p04749.
14
15
16 Last, R. J., A. A. Nyblade, C. A. Langston, and T. J. Owens (1997), Crustal structure of the East
17 African Plateau from receiver functions and Rayleigh wave phase velocities, *J. Geophys.*
18 *Res.*, 102(B11), 24,469–24,483, doi:10.1029/97JB02156.
19
20
21 Lawrence, J.F. & Wiens, D.A., (2004). Combined receiver-function and surface wave phase-
22 velocity inversion using a niching genetic algorithm: Application to Patagonia, *Bulletin of the*
23 *Seismological Society of America*, 94, 977-987.
24
25
26 Levander, A., B. Schmandt, M. S. Miller, K. Liu, K. E. Karlstrom, R. S. Crow, C. T. A. Lee, and
27 E. D. Humphreys (2011), Continuing Colorado plateau uplift by delamination-style
28 convective lithospheric downwelling, *Nature*, 472(7344), 461-U540.
29
30
31 Levin, V. & Park, J., (1997). P-SH conversions in a flat-layered medium with anisotropy of
32 arbitrary orientation, *Geophysical Journal International*, 131, 253-266.
33
34
35 Levshin, A.L. and M. H. Ritzwoller (1995), Characteristics of surface waves generated by
36 events on and near the Chinese nuclear test site, *Geophys. J. Int.*, 123, 131-149.
37
38
39 Levin, V., N.M. Shapiro, J. Park, and M.H. Ritzwoller (2002), Seismic evidence for catastrophic
40 slab loss beneath Kamchatka, *Nature*, 418, 763-767.
41
42
43 Levshin, A.L., M.H. Ritzwoller, and N.M. Shapiro (2005), The use of crustal higher modes to
44 constrain crustal structure across Central Asia, *Geophys. J. Int.*, 160, 961-972.
45
46
47 Ligorria, J. P., and C. J. Ammon (1999), Iterative deconvolution and receiver-function
48 estimation, *Bulletin of the Seismological Society of America*, 89(5), 1395-1400.
49
50
51 Lin, F.C., Moschetti, M.P. & Ritzwoller, M.H., (2008). Surface wave tomography of the western
52
53
54
55
56
57
58
59
60

1
2
3 United States from ambient seismic noise: Rayleigh and Love wave phase velocity maps,
4 *Geophysical Journal International*, 173, 281-298.
5
6

7 Lin, F.C., M.H. Ritzwoller, Y. Yang, M.P. Moschetti, and M.J. Fouch (2011), Complex and
8 variable crustal and uppermost mantle seismic anisotropy in the western United States,
9 *Nature Geoscience*, Vol 4, Issue 1, 55-61.
10
11

12 Lin, F.C., Ritzwoller, M.H. & Snieder, R., (2009). Eikonal tomography: surface wave
13 tomography by phase front tracking across a regional broad-band seismic array, *Geophysical*
14 *Journal International*, 177, 1091-1110.
15
16

17 Lin, F.C. & Ritzwoller, M.H., 2011. Helmholtz surface wave tomography for isotropic and
18 azimuthally anisotropic structure, *Geophysical Journal International*, 186, 1104-1120.
19
20

21 Lin, F.C., V. Tsai, and M.H. Ritzwoller (2012a), The local amplification of surface waves: A new
22 observable to constrain elastic velocities, density, and anelastic attenuation, *J. Geophys. Res.*,
23 117, B06302, doi:10.1029/2012JB009208.
24
25

26 Lin, F.C., B. Schmandt, and V.C. Tsai (2012b), Joint inversion of Rayleigh wave phase velocity
27 and ellipticity using USArray: constraining velocity and density structure in the upper crust,
28 submitted to *Geophys. Res. Letts*.
29
30

31 Liu, Q.Y., Li, Y., Chen, J.H., van der Hilst, R.D., Guo, B.A., Wang, J., Qi, S.H. & Li, S.C.,
32 (2010). Joint inversion of receiver function and ambient noise based on Bayesian theory,
33 *Chinese Journal of Geophysics-Chinese Edition*, 53, 2603-2612.
34
35

36 Lowry, A.R. & Perez-Gussinye, M., (2011). The role of crustal quartz in controlling Cordilleran
37 deformation, *Nature*, 471, 353-+.
38
39

40 Lucente, F. P., N. Piana Agostinetti, M. Moro, G. Selvaggi, and M. Di Bona (2005), Possible fault
41 plane in a seismic gap area of the southern Apennines (Italy) revealed by receiver function
42 analysis, *J. Geophys. Res.*, 110, B04307, doi:10.1029/2004JB003187.
43
44

45 Maraschini, M. & Foti, S., 2010. A Monte Carlo multimodal inversion of surface waves,
46 *Geophysical Journal International*, 182, 1557-1566.
47
48

49 Megnin, C., and B. Romanowicz (2000), The three-dimensional shear velocity structure of the
50 mantle from the inversion of body, surface and higher-mode waveforms, *Geophysical*
51
52

1
2
3 *Journal International*, 143(3), 709-728.

4
5
6 Molnar, S., S.E. Dosso and J.F. Cassidy, (2010). Bayesian inversion of microtremor array
7 dispersion data in southwestern British Columbia, *Geophys. J. Int.*, 183, 923-940.

8
9
10 Mooney, W. D., and M. K. Kaban (2010), The North American upper mantle: Density,
11 composition, and evolution, *J. Geophys. Res.*, 115, B12424, doi:10.1029/2010JB000866.

12
13
14 Moorkamp, M., A. G. Jones, and S. Fishwick (2010), Joint inversion of receiver functions,
15 surface wave dispersion, and magnetotelluric data, *J. Geophys. Res.*, 115, B04318,
16 doi:10.1029/2009JB006369.

17
18
19
20 Moschetti, M.P., M.H. Ritzwoller, and F.C. Lin (2010), Seismic evidence for widespread crustal
21 deformation caused by extension in the western USA, *Nature*, 464, Number 7290, 885-889.

22
23
24 Moschetti, M. P., M. H. Ritzwoller, and N. M. Shapiro (2007), Surface wave tomography of the
25 western United States from ambient seismic noise: Rayleigh wave group velocity
26 maps, *Geochem. Geophys. Geosyst.*, 8, Q08010, doi:10.1029/2007GC001655.

27
28
29
30 Moschetti, M. P., M. H. Ritzwoller, F. C. Lin, and Y. Yang (2010a), Crustal shear wave velocity
31 structure of the western United States inferred from ambient seismic noise and earthquake
32 data, *Journal of Geophysical Research-Solid Earth*, 115.

33
34
35
36 Moschetti, M.P., M.H. Ritzwoller, F.C. Lin, and Y. Yang, Crustal shear velocity structure of the
37 western US inferred from amient noise and earthquake data (2010b), *J. Geophys. Res.*, 115,
38 B10306, doi:10.1029/2010JB007448.

39
40
41 Mosegaard, K., and A. Tarantola (1995), Monte Carlo sampling of solutions to inverse
42 problems, *J. Geophys. Res.*, 100(B7), 12,431–12,447, doi:10.1029/94JB03097.

43
44
45
46 Mosegaard K. and Sambridge M. 2002. Monte Carlo analysis of inverse problems. *Inverse*
47 *Problems* 18, 29–54.

48
49
50 Nicholson, T., Bostock, M. & Cassidy, J.F., (2005). New constraints on subduction zone structure
51 in northern Cascadia, *Geophysical Journal International*, 161, 849-859.

52
53
54 Ozalaybey, S., Savage, M.K., Sheehan, A.F., Louie, J.N. & Brune, J.N., (1997). Shear-wave
55 velocity structure in the northern Basin and Range province from the combined analysis of
56
57
58
59
60

1
2
3 receiver functions and surface waves, *Bulletin of the Seismological Society of America*, 87,
4 183-199.
5
6

7 Pasyanos, M.E., Tkalčić, H., Gok, R., Al-Enezi, A. & Rodgers, A.J., (2007). Seismic structure of
8 Kuwait, *Geophysical Journal International*, 170, 299-312.
9

10 Piana Agostinetti, N., F. P. Lucente, G. Selvaggi, and M. Di Bona (2002), Crustal Structure and
11 Moho Geometry beneath the Northern Apennines (Italy), *Geophys. Res. Lett.*, 29(20), 1999,
12 doi:10.1029/2002GL015109.
13
14
15

16 Piana Agostinetti, N. & Chiarabba, C., 2008. Seismic structure beneath Mt Vesuvius from
17 receiver function analysis and local earthquakes tomography: evidences for location and
18 geometry of the magma chamber, *Geophysical Journal International*, 175, 1298-1308.
19
20
21

22 Piana Agostinetti, N. & Malinverno, A., 2010. Receiver function inversion by trans-dimensional
23 Monte Carlo sampling, *Geophysical Journal International*, 181, 858-872.
24
25
26

27 Pollitz, F.F. (2008), Observations and interpretation of fundamental mode Rayleigh wavefields
28 recorded by the Transportable Array (USArray), *Geophys. J. Int.*, **173**,189-204.
29
30
31

32 Pollitz, F. F. & Snoke, J. A. (2010), Rayleigh-wave phase-velocity maps and three dimensional
33 shear velocity structure of the western US from local non-plane surface wave tomography.
34 *Geophys. J. Int.*, **180**, 1153–1169.
35
36

37 Ritzwoller, M.H. and A.L. Levshin (1998), Eurasian surface wave tomography: Group velocities,
38 *J. Geophys. Res.*, 103, 4839 - 4878.
39
40
41

42 Ritzwoller, M.H., A.L. Levshin, L.I. Ratnikova, and A.A. Egorin (1998), Intermediate period
43 group velocity maps across Central Asia, Western China, and parts of the Middle East,
44 *Geophys. J. Int.*, 134, 315-328.
45
46
47

48 Ritzwoller, M. H., N. M. Shapiro, A. L. Levshin, and G. M. Leahy (2001), Crustal and upper
49 mantle structure beneath Antarctica and surrounding oceans, *J. Geophys. Res.*, 106(B12),
50 30,645–30,670, doi:10.1029/2001JB000179.
51
52
53

54 Ritzwoller, M.H., N.M. Shapiro, and G.M. Leahy, A resolved mantle anomaly as the cause of the
55 Australian-Antarctic Discordance (2003), *J. Geophys. Res.*, 108, no. B12, 2559,
56 doi:10.1029/2003JB002522.
57
58
59
60

- 1
2
3 Ritzwoller, M.H., N.M. Shapiro, S. Zhong (2004), Cooling history of the Pacific lithosphere,
4 *Earth Planet. Sci. Letts.*, 226, 69-84.
5
6
7 Ritzwoller, M.H., F.C. Lin, and W. Shen, Ambient noise tomography with a large seismic array,
8 *Compte Rendus Geoscience*, (2011), 13 pages, doi:10.1016/j.crte.2011.03.007.
9
10
11 Roy, M., T. H. Jordan, and J. Pederson (2009), Colorado Plateau magmatism and uplift by
12 warming of heterogeneous lithosphere, *Nature*, 459(7249), 978-U102.
13
14
15 Salah, M.K., Chang, S.J. & Fonseca, J., 2011. Crustal structure beneath the Lower Tagus Valley,
16 southwestern Iberia using joint analysis of teleseismic receiver functions and surface-wave
17 dispersion, *Geophysical Journal International*, 184, 919-933.
18
19
20
21 Sambridge, M., 1999a. Geophysical inversion with a neighbourhood algorithm - I. Searching a
22 parameter space, *Geophysical Journal International*, 138, 479-494.
23
24
25 Sambridge, M., 1999b. Geophysical inversion with a neighbourhood algorithm - II. Appraising
26 the ensemble, *Geophysical Journal International*, 138, 727-746.
27
28
29 Sambridge M. 2001. Finding acceptable models in nonlinear inverse problems using a
30 neighbourhood algorithm. *Inverse Problems* **17**, 387–403.
31
32
33 Sambridge M. and Mosegaard K. 2002. Monte Carlo methods in geophysical inverse problems.
34 *Reviews of Geophysics* **40**, 1–29
35
36
37 Savage, M. K. (1998), Lower crustal anisotropy or dipping boundaries? Effects on receiver
38 functions and a case study in New Zealand, *J. Geophys. Res.*, 103, 15069-15087.
39
40
41
42 Schultz, C.A., Myers, S.C., Hipp, J. & Young, C.J., 1999. Nonstationary Bayesian kriging: a
43 predictive technique to generate spatial corrections for seismic detection, location and
44 identification, *Physics of the Earth and Planetary Interiors*, 113, 321-338.
45
46
47
48 Shapiro, N.M., Campillo, M., Stehly, L. & Ritzwoller, M.H., 2005. High-resolution surface-wave
49 tomography from ambient seismic noise, *Science*, 307, 1615-1618.
50
51
52
53 Shapiro, N.M. & Ritzwoller, M.H., 2002. Monte-Carlo inversion for a global shear-velocity
54 model of the crust and upper mantle, *Geophysical Journal International*, 151, 88-105.
55
56
57 Shapiro, N. M., M. H. Ritzwoller, and E. R. Engdahl (2008), Structural context of the great
58
59
60

1
2
3 Sumatra-Andaman Islands earthquake, *Geophys. Res. Lett.*, 35, L05301,
4
5 doi:10.1029/2008GL033381.
6

7 Sheehan, A. F., C. H. Jones, M. K. Savage, S. Ozalaybey, and J. M.

8
9 Schneider (1997), Contrasting lithospheric structure between the Colorado Plateau and Great
10 Basin: Initial results from Colorado Plateau - Great Basin PASSCAL Experiment, *Geophys.*
11 *Res. Lett.*, 24(21), 2609–2612, doi:10.1029/97GL02782.
12
13

14
15 Shibutani, T., M. Sambridge, and B. Kennett (1996), Genetic algorithm inversion for receiver
16 functions with application to crust and uppermost mantle structure beneath eastern
17 Australia, *Geophys. Res. Lett.*, 23(14), 1829–1832, doi:10.1029/96GL01671.
18
19

20
21 Socco, L.V. and D. Boiero, Improved Monte Carlo inversion of surface wave data (2008),
22
23 *Geophys. Prospecting*, 56, 357-371.
24

25
26 Tarantola, A., and B. Valette (1982), Generalized nonlinear inverse problems solved using the
27 least squares criterion, *Rev. Geophys.*, 20(2), 219–232, doi:10.1029/RG020i002p00219.
28

29
30 Tkalčić, H., M. E. Pasyanos, A. J. Rodgers, R. Gök, W. R. Walter, and A. Al-Amri (2006), A
31 multistep approach for joint modeling of surface wave dispersion and teleseismic receiver
32 functions: Implications for lithospheric structure of the Arabian Peninsula, *J. Geophys.*
33 *Res.*, III, B11311, doi:10.1029/2005JB004130.
34
35

36
37 Tokam, A.P.K., Tabod, C.T., Nyblade, A.A., Julia, J., Wiens, D.A. & Pasyanos, M.E. (2010),
38 Structure of the crust beneath Cameroon, West Africa, from the joint inversion of Rayleigh
39 wave group velocities and receiver functions, *Geophysical Journal International*, 183, 1061-
40
41 1076.
42
43

44
45 Villasenor, A., M.H. Ritzwoller, A.L. Levshin, M.P. Barmin, E.R. Engdahl, W. Spakman, and J.
46 Trampert (2001), Shear velocity structure of Central Eurasia from inversion of surface wave
47 velocities, *Phys. Earth Planet. Int.*, 123(2-4), 169 - 184.
48
49

50
51 Vinnik, L.P., 1977. Detection of waves converted from P to SV in the mantle, *Earth Planet.*
52 *Inter.*, 15, 39-45.
53

54
55 Vinnik, L.P., Aleshin, I.M., Kaban, M.K., Kiselev, S.G., Kosarev, G.L., Oreshin, S.I. & Reigber,
56 C., 2006. Crust and mantle of the Tien Shan from data of the receiver function tomography,
57
58
59
60

1
2
3 *Izvestiya-Physics of the Solid Earth*, 42, 639-651.

4
5
6 Vinnik, L.P., Reigber, C., Aleshin, I.M., Kosarev, G.L., Kaban, M.K., Oreshin, S.I. & Roecker,
7 S.W., 2004. Receiver function tomography of the central Tien Shan, *Earth and Planetary*
8 *Science Letters*, 225, 131-146.

9
10
11 Wilson, C. K., Jones, C. H., and Gilbert, H. J., 2003. Single-chamber silicic magma system
12 inferred from shear wave discontinuities of the crust and uppermost mantle, Coso geothermal
13 area, California, *J. Geophys. Res.*, 108(B5), 2226.

14
15
16
17 Yang, Y. & Forsyth (2006), D. Regional tomographic inversion of the amplitude and phase of
18 Rayleigh waves with 2-D sensitivity kernels, *Geophys. J. Int.*, **166**, 1148–1160.

19
20
21 Yang, Y.J., Ritzwoller, M.H., Levshin, A.L. & Shapiro, N.M., 2007. Ambient noise rayleigh wave
22 tomography across Europe, *Geophysical Journal International*, 168, 259-274.

23
24
25
26 Yang, Y., and M. H. Ritzwoller (2008), Teleseismic surface wave tomography in the western U.S.
27 using the Transportable Array component of USArray, *Geophys. Res. Lett.*, 35, L04308,
28 doi:10.1029/2007GL032278.

29
30
31
32 Yang, Y., A. Li, and M.H. Ritzwoller (2008a), Crustal and uppermost mantle structure in
33 southern Africa revealed from ambient noise and teleseismic tomography, *Geophys. J. Int.*,
34 doi:10.1111/j.1365-246X.2008.03779.x.

35
36
37
38 Yang, Y., M. H. Ritzwoller, F.-C. Lin, M. P. Moschetti, and N. M. Shapiro (2008b), Structure of
39 the crust and uppermost mantle beneath the western United States revealed by ambient noise
40 and earthquake tomography, *J. Geophys. Res.*, 113, B12310, doi:10.1029/2008JB005833.

41
42
43
44 Yang, Y., M. H. Ritzwoller, and C. H. Jones (2011), Crustal structure determined from ambient
45 noise tomography near the magmatic centers of the Coso region, southeastern
46 California, *Geochem. Geophys. Geosyst.*, 12, Q02009, doi:10.1029/2010GC003362.

47
48
49
50 Yang, Y., M. H. Ritzwoller, Y. Zheng, W. Shen, A. L. Levshin, and Z. Xie (2012), A synoptic
51 view of the distribution and connectivity of the mid-crustal low velocity zone beneath
52 Tibet, *J. Geophys. Res.*, 117, B04303, doi:10.1029/2011JB008810.

53
54
55
56 Yao, H.J., van der Hilst, R.D. & de Hoop, M.V., 2006. Surface-wave array tomography in SE
57 Tibet from ambient seismic noise and two-station analysis - I. Phase velocity maps,
58
59
60

1
2
3
4
5
6
7
8
9
10
11
12
13
14
15
16
17
18
19
20
21
22
23
24
25
26
27
28
29
30
31
32
33
34
35
36
37
38
39
40
41
42
43
44
45
46
47
48
49
50
51
52
53
54
55
56
57
58
59
60

Geophysical Journal International, 166, 732-744.

Yoo, H.J., Herrmann, R.B., Cho, K.H. & Lee, K., 2007. Imaging the three-dimensional crust of the Korean Peninsula by joint inversion of surface-wave dispersion and teleseismic receiver functions, *Bulletin of the Seismological Society of America*, 97, 1002-1011.

Yoshizawa, K. and B.L.N. Kennett (2002), Non-linear waveform inversion for surface waves with a neighbourhood algorithm – application to multimode dispersion measurements, *Geophys. Int.* 149, 118-133.

Zhao, L.S., Sen, M.K., Stoffa, P. & Frohlich, C., 1996. Application of very fast simulated annealing to the determination of the crustal structure beneath Tibet, *Geophysical Journal International*, 125, 355-370.

Zheng, X. F., Z. X. Yao, J. H. Liang, and J. Zheng (2010), The role played and opportunities provided by IGP DMC of China National Seismic Network in Wenchuan earthquake disaster relief and researches, *Bull. Seismol. Soc. Am.*, 100(5B), 2866-2872.

Zheng, Y., W. Shen, L. Zhou, Y. Yang, Z. Xie, and M. H. Ritzwoller (2011), Crust and uppermost mantle beneath the North China Craton, northeastern China, and the Sea of Japan from ambient noise tomography, *J. Geophys. Res.*, 116, B12312, doi:10.1029/2011JB008637.

Zhou, L., J. Xie, W. Shen, Y. Zheng, Y. Yang, H. Shi, and M.H. Ritzwoller (2012), The structure of the crust and uppermost mantle beneath South China from ambient noise and earthquake tomography, *Geophys. J. Int.*, doi: 10.1111/j.1365-246X.2012.05423.x.

Zhu, L., and H. Kanamori (2000), Moho depth variation in southern California from teleseismic receiver functions, *J. Geophys. Res.*, 105(B2), 2969–2980, doi:10.1029/1999JB900322.

Figure 1. Stations of the Earthscope USArrayTransportable Array(TA) used in this study are shown with blue triangles. The main geological provinces are outlined with red contours and titled with red abbreviations (the Basin and Range (BR) province, the Colorado Plateau (CP), the Rocky Mountains (RM), and the Great Plains (GP)). Other regional geological features and basins are also identified with abbreviations (Snake River Plain (SNP), Green River Basin in Southern Wyoming (GRB), Uinta Basin in Northwestern Utah (UB), Piceance Basin in northwestern Colorado (PB) and Denver Basin in Colorado (DB). Four stations that are used to demonstrate the methods are identified with red triangles. The black line indicates transect A-A' ranging from the BR to the GP.

Figure 2. (a-c) Phase velocity maps at periods of 8, 20 and 36 sec from ambient noise eikonal tomography (ANT). (d-e) Phase velocity maps at 36 and 70 sec from earthquake Helmholtz tomography (ET). (f) Difference between the ANT and EQ results at 36 sec period.

Figure 3. Phase velocity curves taken from the maps presented in Fig. 2 (and similar maps at the intervening periods) at the locations of stations R11A, T18A, Q22A and O25A, respectively. Blue symbols are uncertainties from the ambient noise tomography maps, red symbols are uncertainties for earthquake tomography maps, and the line is the joint dispersion curve from the two kinds of measurements.

Figure 4. (a) The quality controlled receiver functions are plotted along back-azimuth for station R11A. (b) The estimated receiver functions, $H(\theta, t)$, from harmonic stripping. (c) The difference between (a) and (b), from which uncertainties in the azimuthally independent receiver function are determined. (d-f) The three estimated components from harmonic stripping.

Figure 5: The estimated azimuthally independent receiver function ($A_0(t)$, red curve) and uncertainty ($s(t)$, gray corridor) for four stations whose locations are identified in Fig. 1. The uncertainty is the rms of the residual remaining after the harmonic fitting (eqn. (A2)) to the azimuthally dependent receiver functions, reduced by a factor of two between 3 and 8 sec.

Figure 6. Model parameterization illustrating the 13 model parameters used in the Monte Carlo sampling of model space.

Figure 7. Prior distribution for several of the model parameters at the location of TA station R11A: (a) sediment thickness, (b) V_{sv} at 10 km depth, (c) crustal thickness, (d) V_{sv} in the lower

1
2
3 crust, (e) velocity contrast from 4 km above to 4 km below Moho (mantle – crust), and (f) V_{sv} at
4
5 120 km depth.
6

7
8 **Figure 8.** Convergence of the sampling of the posterior distribution of models when only surface
9 wave dispersion data are used at the location of station R11A. Models are provisionally accepted
10 according to the Metropolis Law in eqn. (4), and then replaced by other models as the procedure
11 evolves. Red dots are the likelihood function (eqn. (2)) for each model that is accepted during the
12 Metropolis sampling of model space, while blue dots are the rms-misfit (first term on the RHS of
13 eqn. (15)). The convergence point is at ~ 100 models (dashed line).
14
15
16
17

18
19 **Figure 9.** (a)-(f) The same as Fig. 7 for TA station R11A, but here the posterior distributions after
20 Monte Carlo sampling using surface wave data alone (models fit the surface wave data) are
21 plotted. The prior distributions from Fig. 7 are plotted as white histograms in the background.
22 Surface wave data reduce the spread of structural velocities between boundaries, but have less
23 effect on the depth to boundaries or velocity jumps across boundaries due to trade-offs between
24 the parameters near the boundaries.
25
26
27
28

29
30 **Figure 10.** (a-b) The model ensemble at the location of TA station R11A in the Basin and Range
31 province resulting from the Monte Carlo inversion of surface wave data alone is shown in full
32 width (black lines with gray fill) and 1σ width (red corridor. Average Moho depth is identified as
33 a dashed line at ~ 32 km. (c) The observed receiver function (white line) is plotted with predicted
34 receiver functions (maroon lines) computed from all accepted models (eqn. (7)), showing that
35 receiver functions are not well fit, on average, by models constrained by surface wave data alone.
36 (d) The observed Rayleigh wave phase velocity dispersion data (black error bars) are plotted
37 with predicted surface wave phase velocity curves computed from all accepted models (eqn. (7),
38 gray lines). The red curve is the predicted phase velocity curve from the best fitting model.
39
40
41
42
43
44
45

46
47 **Figure 11.** (a) The joint likelihood function (from eqns. (2) and (8), red dots) and the joint misfit
48 function (eqn. (8), blue dots) for TA station R11A as a function of number of models sampled. (b)
49 Misfit for each individual data set in the same search as (a). Blue dots are for surface wave phase
50 velocity data and red dots are for the RF data. When the model converges to maximize the
51 likelihood functional, both misfits typically converge to < 1 . In both plots, the location of 500
52 sampled models is identified with a dashed line, where the fit approaches convergence.
53
54
55
56

57
58 **Figure 12.** (a-f) The same as Fig. 9, but for the posterior distribution resulting from the joint
59
60

1
2
3 inversion of surface wave phase velocities and receiver functions. Note the sharpening of
4 distributions for parameters near the Moho in (c) – (e) compared to the distributions resulting
5 from surface wave data alone (Fig. 9).
6
7

8
9 **Figure 13.** (a-b): The same as Fig. 10, but for results from the joint inversion of Rayleigh wave
10 phase velocities and receiver functions at the same TA station (R11A). (c) The synthetic receiver
11 functions from the accepted model ensemble are plotted with gray lines, with the best fitting
12 receiver function shown as the red curve. The parallel black lines are the estimated uncertainty of
13 the receiver function. There is a clear P-to-S conversion near 4 sec period, necessitating a large
14 velocity jump at a shallow Moho. (d) The predicted surface wave dispersion curves from all
15 accepted models are plotted with gray lines with the best fitting curve identified in red.
16
17

18
19 **Figure 14.** The same as Fig. 13, but for the result at TA station T18A located in the Colorado
20 Plateau. No clear P-to-S Moho conversion is seen on the receiver function, probably implying a
21 gradient Moho.
22
23

24
25 **Figure 15.** The same as Fig. 13, but for the result at TA station Q22A located in the Colorado
26 Rocky Mountains. A clear P-to-S conversion is seen near 6 sec, requiring a large velocity jump at
27 a deeper Moho than in Fig. 13.
28
29

30
31 **Figure 16.** The same as Fig. 13, but for the result at TA station O25A located in the Great Plains.
32 Strong sedimentary reverberations dominate the receiver function adding uncertainty in the
33 location of and velocity jump at the Moho.
34
35

36
37 **Figure 17.** (a) Misfit histogram showing the misfits to surface wave data over the spatial grid
38 covering the area of study. The white histogram is for the model that best fits the surface wave
39 data at each point and the red histogram is for the model that jointly best fits both surface wave
40 and receiver function data. At most grid points, the jointly best fitting models fit the surface wave
41 data only slightly worse than the model that fits the surface wave data best. (b) Same as (a), but
42 for receiver functions. The white histogram is for the model that best fits the receiver function
43 data at each location and the red histogram is for the model that jointly best fits both data sets. At
44 most grid points, the jointly best fitting models fit the receiver function data only slightly worse
45 than the model that fits the receiver function data best.
46
47
48
49
50
51
52
53
54

55
56 **Figure 18:** Map views of V_{sv} at different depths (left) with uncertainties (right). (a-b) V_{sv} at 10
57
58
59
60

1
2
3 km depth. (c-d) Vsv in the lower crust, 4 km above Moho. (e-f) Vsv at 60 km depth. (g-h) Vsv at
4
5 120 km depth.

6
7 **Figure 19.** (a)-(b) Crustal thickness and its uncertainty resulting from inversion of surface wave
8
9 data alone. (c)-(d) Crustal thickness and its uncertainty resulting from the joint inversion of
10
11 surface wave and receiver function data. (e)-(f) Vsv contrast from 4 km below to 4 km above
12
13 Moho and its uncertainty from the joint inversion of surface wave and receiver function data.

14
15 **Figure 20.** (a) Vsv model along transect AA' in Fig. 1 constructed using surface wave data alone
16
17 with a positive gradient constraint in the uppermost mantle. (b) The same as (a), but with a
18
19 negative constraint on the uppermost mantle velocity gradient. (c) Vsv model from the joint
20
21 inversion of both surface wave and receiver function data with no constraint on the Vsv gradient
22
23 in the uppermost mantle. Crustal structure is presented in absolute shear wave speed but mantle
24
25 structure is presented as the percent perturbation relative to 4.4 km/s. Geological provinces are
26
27 presented with abbreviations (Fig. 1) overlying surface topography.

28
29 **Figure 21:** (a) Posterior distribution of Vp/Vs ratio when it is included as a parameter in the joint
30
31 inversion. The prior distribution is shown with the white histogram outlined in black. (b) The
32
33 posterior distribution of crustal thickness for station R11A from the inversion that includes
34
35 Vp/Vs as a free parameter. (c) The joint misfit (χ^{joint}) is plotted as a function of crustal thickness
36
37 and Vp/Vs ratio. Trade-off between crustal thickness and the Vp/Vs ratio is clear. (d)-(f) The
38
39 same as (a), but for stations T18A, Q22A and O25A, respectively.

40
41 **Figure 22:** (a) Piercing points of the P-wave incident at the Moho for TA stations are shown with
42
43 red dots. The piercing points for CD-ROM stations are shown with blue dots. The green line is
44
45 the transect AB along the CD-ROM line from Colorado to Wyoming. Three TA stations near the
46
47 transect are identified with names (L21A, M21A and O21A from north to south). State
48
49 boundaries are outlined with black lines and red lines are geological provinces (Fig. 1). (b) Moho
50
51 conversion point (MCP) stacked receiver functions are illustrated with red waveforms along
52
53 transect AB in (a). For comparison, single-station processed receiver functions ($A_0(t)$) are shown
54
55 with blue waveform for the three stations identified in (a). (c) The smoothed image of the red
56
57 receiver functions in (b). Blue dots indicate the location of the CD-ROM stations. The location of
58
59 the Cheyenne Belt is marked as CB.

60
Figure A1. (a) Raw receiver function (RF) waveforms for station R11A in the Basin and Range

1
2
3 are plotted as a function of back-azimuth, where 6 sec time is identified with the dashed line. (b)
4 Red dots are RF amplitude measured at 6 sec time with azimuthally binned amplitudes plotted
5 with black error-bars. The harmonic fitting result is shown with the blue curve and the
6 amplitudes of the estimated coefficients A_0 , A_1 , and A_2 (eqn. (A1)) are shown. (c) The
7 azimuthally independent $A_0(t)$ component of the RF that results from harmonic stripping is
8 plotted (red curve) with the uncertainty range (grey corridor), which is the rms of the residual
9 remaining after the harmonic fitting (eqn. (A2)) .

10
11
12
13
14
15
16 **Figure A2.** (a) The 755 raw receiver functions (RFs) are plotted along back-azimuth for TA
17 station R11A. (b) The same as (a), but for the 144 RFs in (a) that have been quality controlled by
18 EARS. (c) The 273 quality controlled RFs including the 144 RFs from EARS and an additional
19 129 RFs from (a) that are consistent with them.

20
21
22
23
24 **Figure A3.** Synthetic experiment performed with Moho dipping 10° with an up-dip azimuth of
25 165° clockwise from North. (a) The synthetic receiver functions $R(\theta, t)$ including additive noise
26 plotted at the appropriate back-azimuth. (b) The estimated receiver functions from harmonic
27 stripping $H(\theta, t)$. (c) The difference between (a) and (b). (d-e) The estimated A_0 , A_1 , A_2
28 components from harmonic stripping, respectively.

29
30
31
32
33 **Figure A4.** The same as Fig. A3, but for synthetic receiver functions computed from a model
34 with 4% azimuthal anisotropy in the mid-to-lower crust with a fast-axis direction at 75°
35 clockwise from North.

36
37
38
39 **Figure A5.** The same as Fig. A3, but for synthetic receiver functions from a model with a 5 km
40 step of crustal thickness such that Moho is at 40 km depth east of the station and 45 km depth
41 west of the station.

42
43
44
45 **Figure A6.** The same as Fig. A3, but for synthetic receiver functions from a model with a 2km
46 jump of sedimentary layer thickness such that there are no sediments east of the station and 2 km
47 of sediments west of the station.

48
49
50
51 **Figure A7.** (a) The azimuthally independent A_0 receiver function estimated from harmonic
52 stripping computed from a model with the dipping Moho is shown with the red dashed line. For
53 comparison, the receiver function from the azimuthally averaged model (horizontal Moho) is
54 shown with the blue line. Uncertainties $s(t)$ are outlined by red lines with a light-red fill. (b) The
55
56
57
58
59
60

1
2
3 same as (a), but for the A_0 receiver function estimated from synthetic receiver functions
4
5 computed using a model with 4% anisotropy in the mid-to-lower crust. (c) The same as (a), but
6
7 for the A_0 receiver function estimated from a model with a step in Moho depth of 5 km at the
8
9 station. (d) The same as (a), but for a model with a 2 km step in sediment thickness at the station.
10
11
12
13
14
15
16
17
18
19
20
21
22
23
24
25
26
27
28
29
30
31
32
33
34
35
36
37
38
39
40
41
42
43
44
45
46
47
48
49
50
51
52
53
54
55
56
57
58
59
60

For Peer Review

APPENDIX: CONSTRUCTING AZIMUTHALLY INDEPENDENT RECEIVER FUNCTIONS BY “HARMONIC STRIPPING”

A1. Receiver function data collection

We apply the time-domain iterative deconvolution method (Ligorria and Ammon, 1999) to a time window between 20 sec before and 30 sec after the predicted P-wave arrival to calculate radial component receiver functions and filtered to produce a pulse width of approximately 1 sec. P-waves at different distances have different incidence angles that affect both the timing and the amplitude of the P-to-S converted phase (Jones and Phinney, 1998; Levin and Park, 1997; Bostock, 1998). We make corrections to the receiver functions in both time and amplitude by normalizing to a reference slowness of 0.06 deg/sec. The correction is based on a two-layer model with a crustal layer ($V_s = 3.7$ km/sec) of 40 km thickness and a half-space mantle layer ($V_s = 4.3$ km/sec). Because this correction is designed to normalize the P-to-S conversion at the Moho discontinuity and reverberated phases have a different time and amplitude dependence on incidence angle, we discard the portion of the receiver function beyond 10 sec after the direct P-signal. Any shallow sedimentary multiples that are present in the receiver functions are still retained in this time series, but they are stacked down because of their different move-out behavior. After application of this correction, remaining variations in receiver functions over azimuth are mainly due to systematic effects such as dipping interfaces or anisotropy beneath the receiver, structural heterogeneity, scattering (Abers, 1998), and random noise in the seismograms. An example of quality controlled receiver functions observed at station R11A in the Basin and Range region is shown in Figures A1a, where the receiver functions are arrayed according to event back-azimuth.

A2. Harmonic stripping

Harmonic analysis of receiver functions is designed to analyze the azimuthal dependence of receiver function arrivals such that azimuthally smooth structural affects are detected and removed, notably potential dipping interfaces (e.g. Savage, 1998; Bianchi et al., 2010) and azimuthal anisotropy (e.g. Girardin and Farra, 1998). This is possible because both dipping interfaces and anisotropy generate sinusoidal variations as a function of back-azimuth with different azimuthal periodicity (Jones and Phinney, 1998). Decomposition into azimuthal components isolates contributions from horizontal symmetry axis anisotropy (two amplitude

peaks and troughs over the complete backazimuthal range) and a much stronger plunging symmetry axis anisotropy signal or dipping isotropic interfaces (one peak and trough over backazimuth). The azimuthally-independent component of the resulting harmonic function represents an isotropic, horizontally-layered average of structure that is relatively unbiased by uneven and incomplete backazimuthal sampling, and is useful for joint inversion with surface waves:

$$H(\theta, t) = A_0(t) + A_1(t)\sin(\theta + \theta_1(t)) + A_2(t)\sin(2\theta + \theta_2(t)) \quad (\text{A1})$$

where the A_i ($i=0,1,2$) are amplitudes of the three harmonic components, and the θ_i are initial phases for the azimuthally dependent components. An example of the amplitude vs. backazimuth for the receiver functions observed at TA station R11A at 6 sec is shown in [Figure A1b](#).

Under realistic circumstances where dipping interfaces and anisotropy beneath the receiver frequently exist, A_1 and A_2 will not be zero whereas A_0 will be the azimuthally-independent receiver function ([Fig. A1c](#)). Here, $A_0(t)$ is treated as the receiver function that is sensitive to the average horizontally-layered isotropic structure beneath the receiver and is, therefore, comparable to surface wave dispersion data. We refer to the method by which the azimuthally independent receiver function, $A_0(t)$, is estimated by fitting and removing the harmonic function $H(\theta, t)$ from the raw receiver functions as “harmonic stripping”.

To estimate the uncertainty $s(t)$ in $A_0(t)$ we use the RMS difference over azimuth between the observed receiver functions and the harmonic function defined by equation (A1):

$$s(t) = \left[N^{-1} \sum_{i=1}^N (R_i(\theta_i, t) - H(\theta_i, t))^2 \right]^{1/2} \quad (\text{A2})$$

Here, $R_i(\theta_i, t)$ represents an observed quality-controlled (see below) receiver function at discrete azimuth θ_i for event i and N is the number of such receiver functions. This residual is a measure of the difference between the red dots and the fit line in [Figure A1b](#), averaged over azimuth.

[Figure 4c](#) shows the difference between the observed receiver functions and the harmonic function for station R11A. The uncertainty estimated in this way is presented in [Figure A1c](#) as a one standard deviation corridor about $A_0(t)$. Examples of receiver functions and uncertainties are presented for other stations in [Figure 5](#).

The RMS of the residuals over time for the receiver functions in [Figure A1c](#) is ~ 0.035 , which is

1
2
3 about twice the estimated noise in receiver functions (~ 0.015) found by [Bodin *et al.* \(2012\)](#), and
4 is also about twice the RMS of the misfit between the observed receiver function and the receiver
5 function from the best fitting model. We believe, therefore, that this definition of the uncertainty
6 in receiver functions over-estimates the uncertainty of $A_0(t)$ that is produced from harmonic
7 stripping. To compensate for this overestimation of the uncertainties, we make two corrections.
8 First, we reduce uncertainties in the azimuthally independent receiver function between 3 sec and
9 8 sec by a factor of two in order to emphasize the fit to the P-to-S converted signal in the receiver
10 functions. Subsequent plots of receiver function uncertainties possess this reduction ([Figs. 5, 13-](#)
11 [16](#)). Second, we introduce a factor (κ) in the Monte Carlo inversion that acts to normalize the
12 misfit to the surface wave and receiver function data as seen in equation (5). The determination
13 of the appropriate value for κ is discussed in section 6.1.

24 **A3. Quality control (QC)**

25 The observed azimuthally dependent receiver functions, $R_i(\theta_i, t)$, that go into the harmonic
26 stripping procedure must first be quality controlled. We build on the quality control applied to
27 the EARS (Earthscope Automated Receiver Study) database and seek only receiver functions
28 that are consistent with the automatically QC'ed receiver functions from EARS used in their
29 stacking procedure that are available through IRIS ([Crotwell and Owens, 2005](#)). The EARS data
30 selection criterion is quite conservative (variance reduction in the iterative deconvolution of at
31 least 80%) so that significant azimuthal gaps are left in the EARS receiver function station sets
32 (e.g., [Fig. A2b](#)). We seek to expand the receiver function database relative to the EARS database,
33 but retain the quality of the constitutive receiver functions in the EARS database.

34 To control the quality of the raw receiver functions (e.g., [Fig. A2a](#) for station R11A) we, first,
35 perform harmonic stripping using the EARS data alone and get a preliminary estimate of the
36 harmonic function $\hat{H}(\theta, t)$. Then we consider each of the raw receiver functions in the database,
37 filtered identically with those in the EARS database (the time windows used in the deconvolution
38 differ somewhat between the EARS and our database, but this has little effect on the resulting
39 receiver functions). Those that are similar to the preliminary estimate $\hat{H}(\theta, t)$ from EARS are
40 retained, whereas those that are dissimilar are rejected. There are numerous ways to define
41 similarity that would yield similar results. We define the difference functional between each raw
42 receiver function at azimuth θ_i and the preliminary estimate of the harmonic fit from EARS as

follows:

$$D(\theta_i) = \left\{ M^{-1} \sum_{j=1}^M [R_i(\theta_i, t_j) - \hat{H}(\theta_i, t_j)]^2 \right\}^{1/2} \quad (\text{A3})$$

where M is the number of discrete time points in the receiver functions. We find that if we retain receiver functions where $D(\theta_i) < 0.05$, then we retain many more receiver functions than in the EARS database but at the same time do not greatly increase the noise level of the database.

Figure A2c presents the results of this QC procedure for TA station R11A. The resulting database has been expanded by about a factor of two relative to EARS, but most of the noisy raw receiver functions have been discarded. We refer to this as the QC'ed receiver function database and it is used to estimate the final harmonic fit and azimuthally independent receiver function $A_0(t)$ with associated uncertainties $s(t)$.

A4. Synthetic test of harmonic stripping

The goal of harmonic stripping is to remove the azimuthal periodicity of receiver function waveforms due to dipping interfaces, azimuthal anisotropy, or other structures beneath the receiver. Synthetic tests are presented here to illuminate the capabilities of harmonic stripping to remove structural effects and recover the azimuthally independent receiver function for a horizontally-layered, isotropic effective medium.

First, we test the affects of structures that produce azimuthally smooth signals in the receiver functions; namely (1) a dipping Moho interface and (2) crustal azimuthal anisotropy, and show that the effects of these types of structures are dealt with effectively by harmonic stripping.

(1) We define a horizontally layered, isotropic model M_0 without a dipping Moho or anisotropy in Table A1. The model, M_d , is the same as M_0 but with Moho tilted by 10° with the up-dip azimuth of 165° relative to North. Synthetic seismograms for every 10° in azimuth are computed [Frederiksen and Bostock, 2000], noise is added to the waveform before the time-domain deconvolution is performed to generate Ps receiver functions, $R(\theta, t)$, which are plotted in Figure A3a. The dipping Moho creates a sinusoidal variation to the P-s conversions at ~ 5.5 sec in both amplitude and arrival time. Harmonic stripping is applied to the synthetic receiver functions and the resulting estimates A_0, A_1, A_2 are shown in Figure A3d-f. As described by Jones and Phinney [1998], the dipping interface generates a 2π periodicity with the strongest amplitude at the updip

1
2
3 azimuth and the arrival time will be delayed most at this azimuth. This phenomenon is observed
4 in the harmonic stripping results. A_1 shows the strongest perturbation at 5-6 sec where the P-s
5 conversion occurs and A_2 is subtle in this time range. **Figure A3b,c** show the harmonic fit, $H(\theta,t)$,
6 and the difference between H and R, respectively. The random noise added to the seismograms is
7 not mapped into the A_1 or A_2 estimates, but resides exclusively in the residuals which we take as
8 the uncertainty of the final azimuthally independent receiver function. For comparison, the
9 receiver functions computed from the horizontally layered model M_0 (blue waveform) and the
10 estimate of A_0 (red dashed line) are shown in **Figure A7a**. The arrival times of the P-s conversion
11 from both are similar, but the A_0 component recovered from the dipping model (red dashed line)
12 displays a somewhat smaller amplitude because the harmonic stripping method does not fully
13 reproduce the sinusoidal variation in arrival time of the input model (blue line). This inaccuracy,
14 however, is encompassed by the enlargement of the uncertainties near the P-S conversion time as
15 discussed further in section 8.2.

16
17
18
19
20
21
22
23
24
25
26
27 (2) We also test an azimuthally anisotropic model, M_{ani} , in which a 4% azimuthally anisotropic
28 layer between 15-45 km depth range with a fast direction at 75° to North is added to M_0 . The
29 resulting synthetic receiver functions contaminated by random noise and the results of harmonic
30 stripping are shown in **Figure A4**. Azimuthal anisotropy introduces a π periodicity into the arrival
31 times of the P-S conversions (**Fig. A4a**), which appears in the estimated A_2 component (**Fig. A4f**).
32 The estimated A_0 component is shown in **Figure A7b** to agree with the receiver function
33 computed from model M_0 .

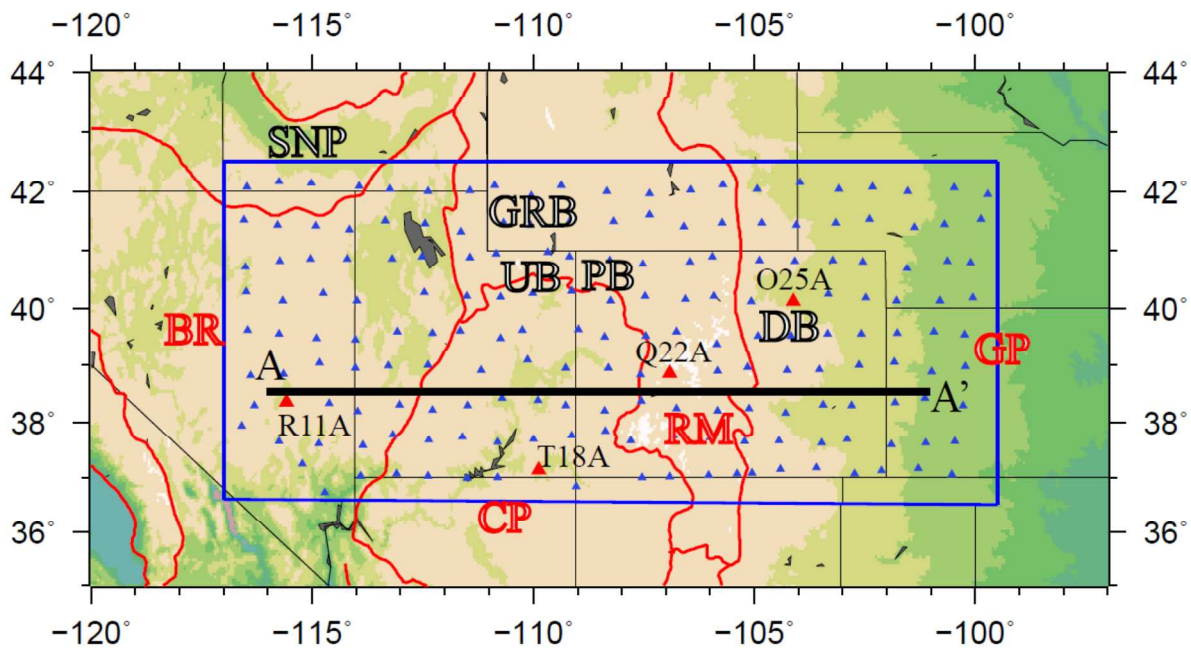
34
35
36
37
38
39
40 From these tests for structures that vary smoothly with azimuth, a dipping Moho or azimuthal
41 anisotropy in the crust, we conclude that the harmonic stripping technique effectively retrieves
42 the azimuthally-independent component which is an accurate estimate of the receiver function
43 for an effective horizontally layered, isotropic medium.

44
45
46
47
48
49
50
51
52
53
54
55
56
57
58
59
60
Second, we test another type of model that possesses azimuthally discontinuous features: (3) a
jump in Moho with azimuth and (4) a jump in sediment thickness with azimuth. We show that
for azimuthally discontinuous structures, harmonic stripping does not reliably estimate the
horizontally layered, isotropic effective medium. The method identifies this problem, however,
by enlarging the uncertainties in the time band in which the estimated receiver function diverges
from the receiver function of the effective medium.

1
2
3
4 (3) On the west side of the receiver (back-azimuthal angle between 180° and 360°) the model is
5 the isotropic horizontally layered model M_0 with a Moho depth of 45 km, but on the east side
6 Moho is 5 km shallower. Synthetic receiver functions from this model with additive noise are
7 plotted in [Figure A5a](#), and the harmonic stripping results are shown in [Figure A5d-f](#). The
8 variations of the receiver functions with back-azimuth are not sinusoidal; thus harmonic stripping
9 cannot fit them fully. As a result, the estimated A_0 component deviates from the receiver function
10 of the average model (a model with a Moho depth of 42.5 km), which is shown as the blue
11 waveform in [Figure A7c](#). However, uncertainties in the A_0 component grow in the time window
12 where A_0 differs from the receiver function of the average model. Thus, in this time band the
13 receiver function will be down-weighted relative to surface wave data, as desired.
14
15
16
17
18
19
20

21 (4) Finally, we test of the model with a step in sediment thickness ([Fig. A6](#)). The model has a 2
22 km sedimentary layer west of the receiver and no sediments on its east side. Both models have
23 the same Moho depth. The average model, therefore, has 1 km of sediments. The synthetic
24 receiver functions in [Figure A6a](#) display a dichotomous pattern such that the Moho P-S
25 conversion arrival times jumps near 180° azimuth. The estimated A_0 component of the receiver
26 function ([Fig. A7d](#)) shows an erroneous double Moho conversion peak as well as relatively large
27 uncertainties that reduce the weight of the receiver function relative to surface wave data in the
28 inversion.
29
30
31
32
33
34
35
36
37
38
39
40
41
42
43
44
45
46
47
48
49
50
51
52
53
54
55
56
57
58
59
60

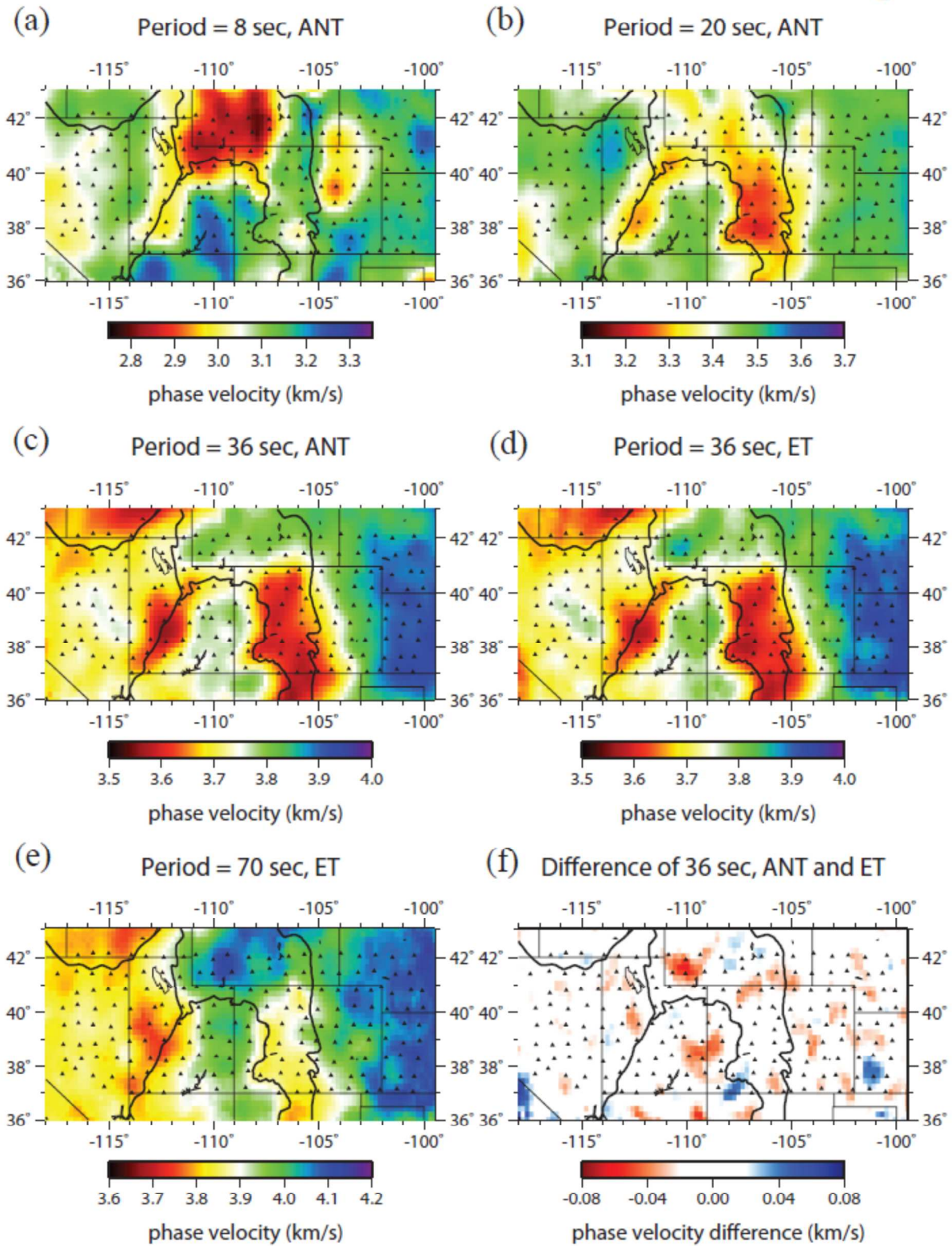
Figure 1



1
2
3
4
5
6
7
8
9
10
11
12
13
14
15
16
17
18
19
20
21
22
23
24
25
26
27
28
29
30
31
32
33
34
35
36
37
38
39
40
41
42
43
44
45
46
47
48
49
50
51
52
53
54
55
56
57
58
59
60

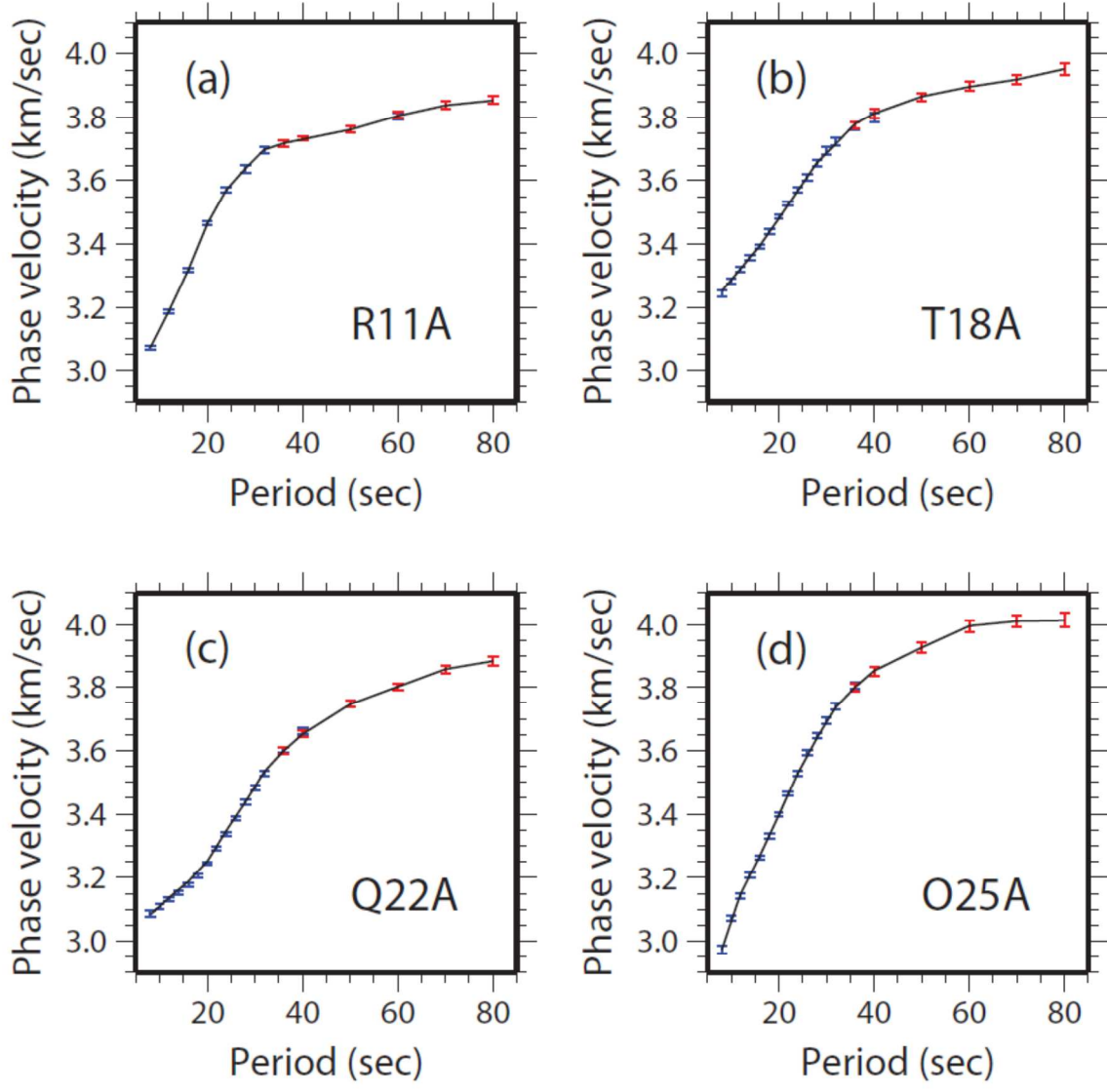
Review

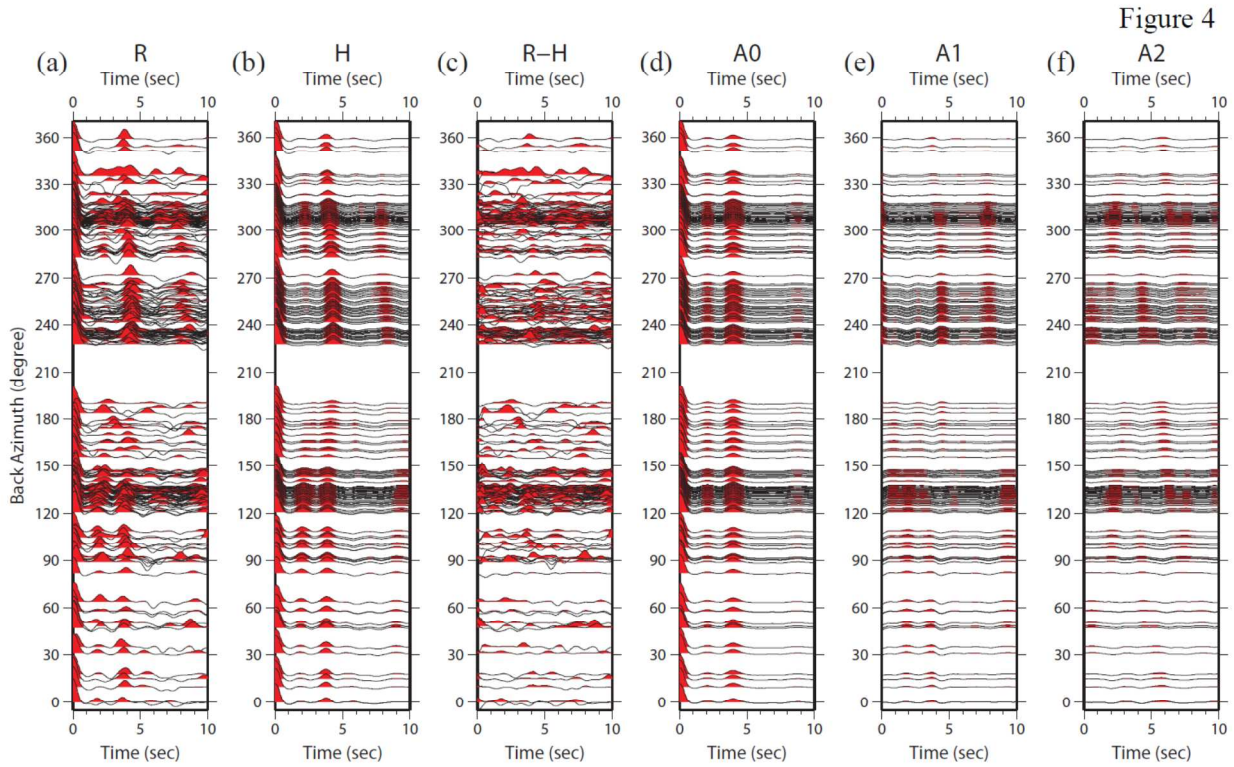
Figure 2



1
2
3
4
5
6
7
8
9
10
11
12
13
14
15
16
17
18
19
20
21
22
23
24
25
26
27
28
29
30
31
32
33
34
35
36
37
38
39
40
41
42
43
44
45
46
47
48
49
50
51
52
53
54
55
56
57
58
59
60

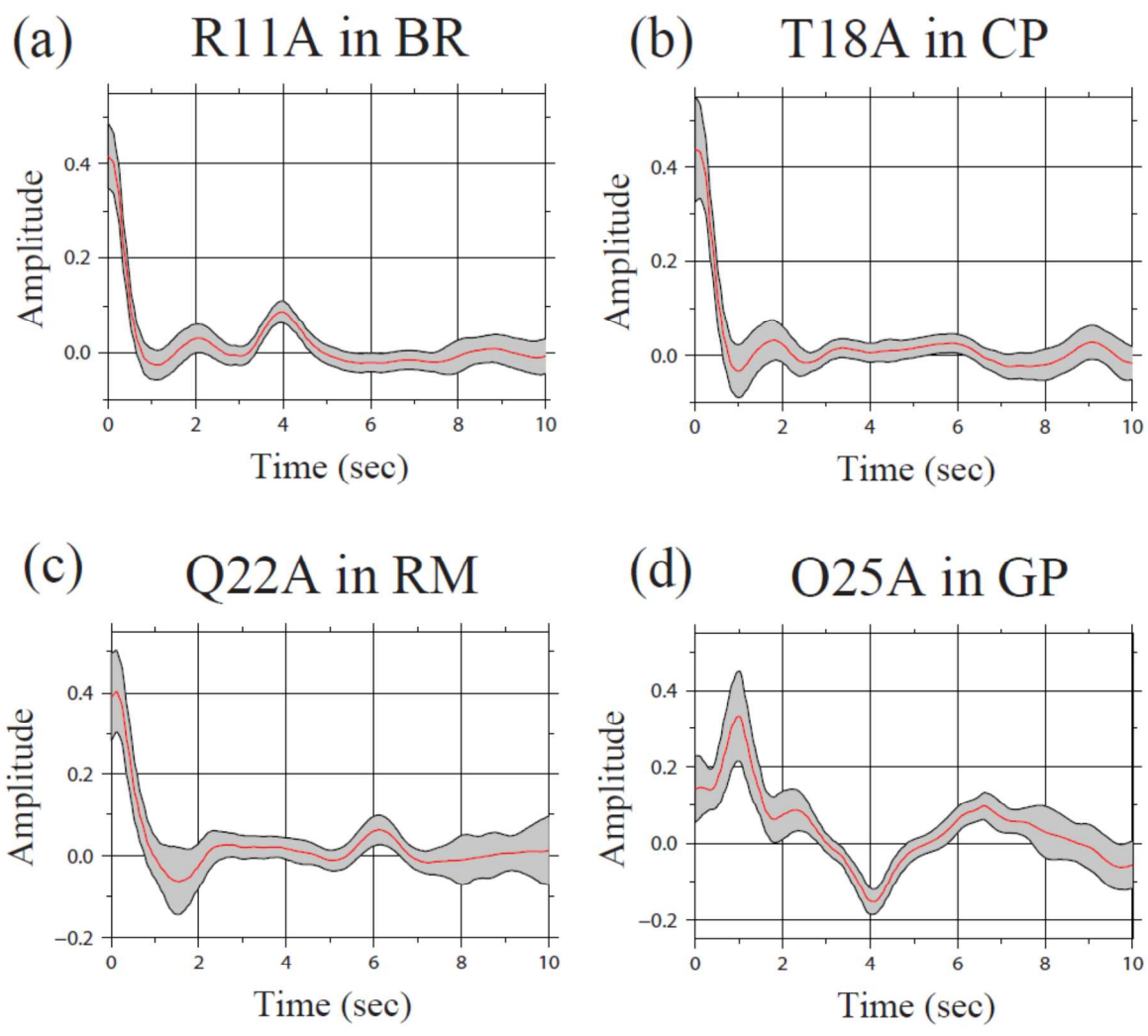
Figure 3





Review

Figure 5



EW

1
2
3
4
5
6
7
8
9
10
11
12
13
14
15
16
17
18
19
20
21
22
23
24
25
26
27
28
29
30
31
32
33
34
35
36
37
38
39
40
41
42
43
44
45
46
47
48
49
50
51
52
53
54
55
56
57
58
59
60

Figure 6

Model parameterization: 13 parameters

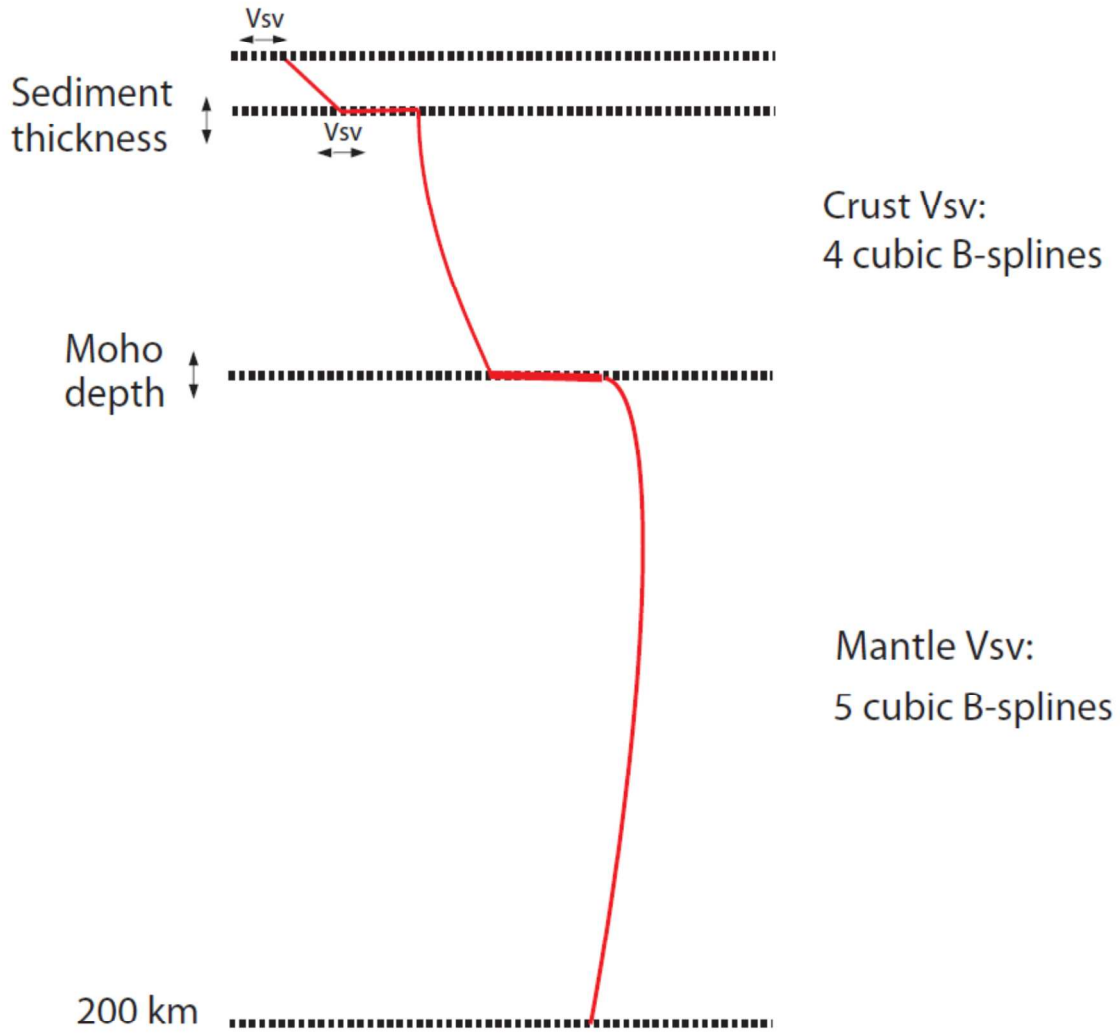


Figure 7

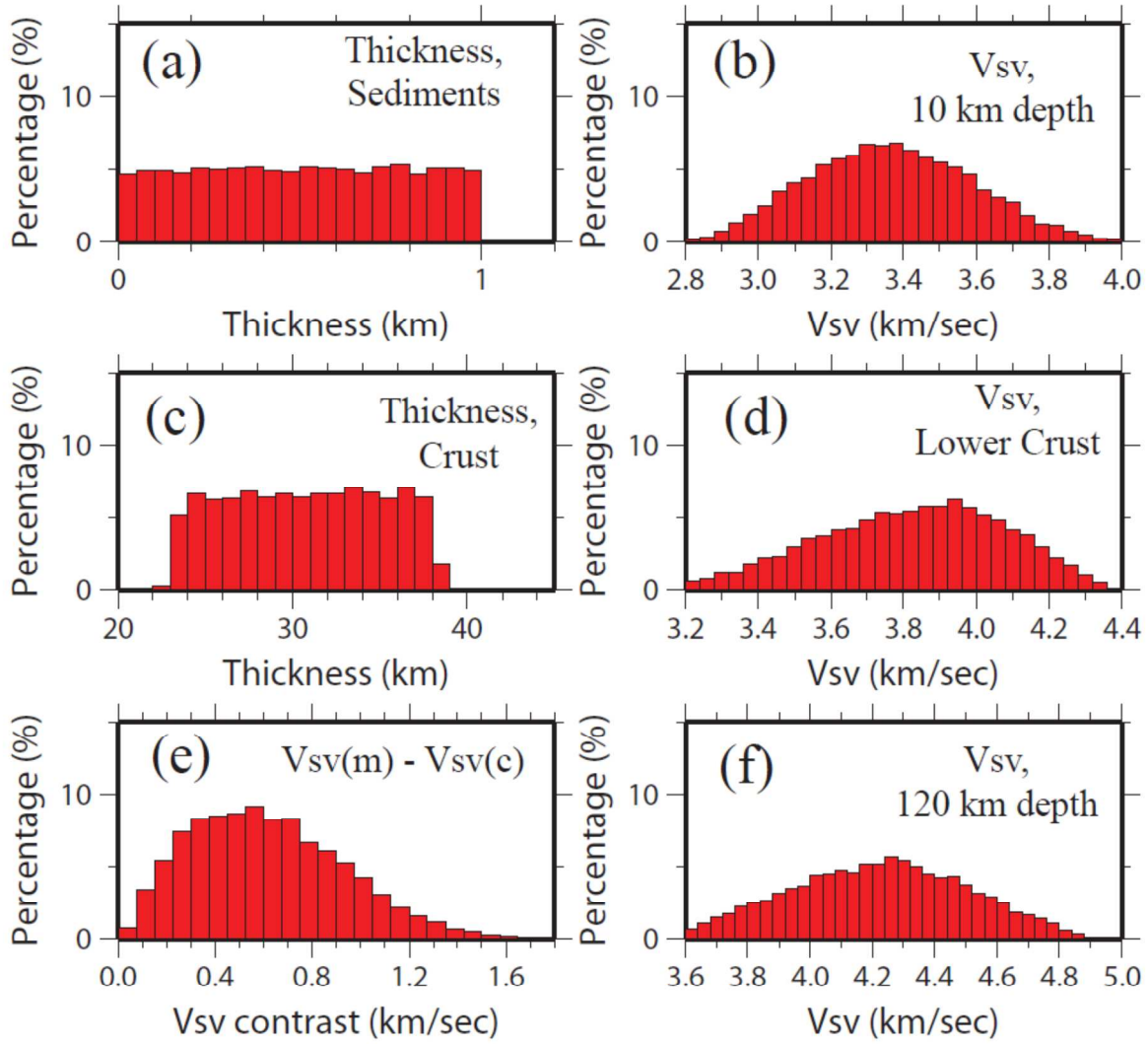


Figure 8

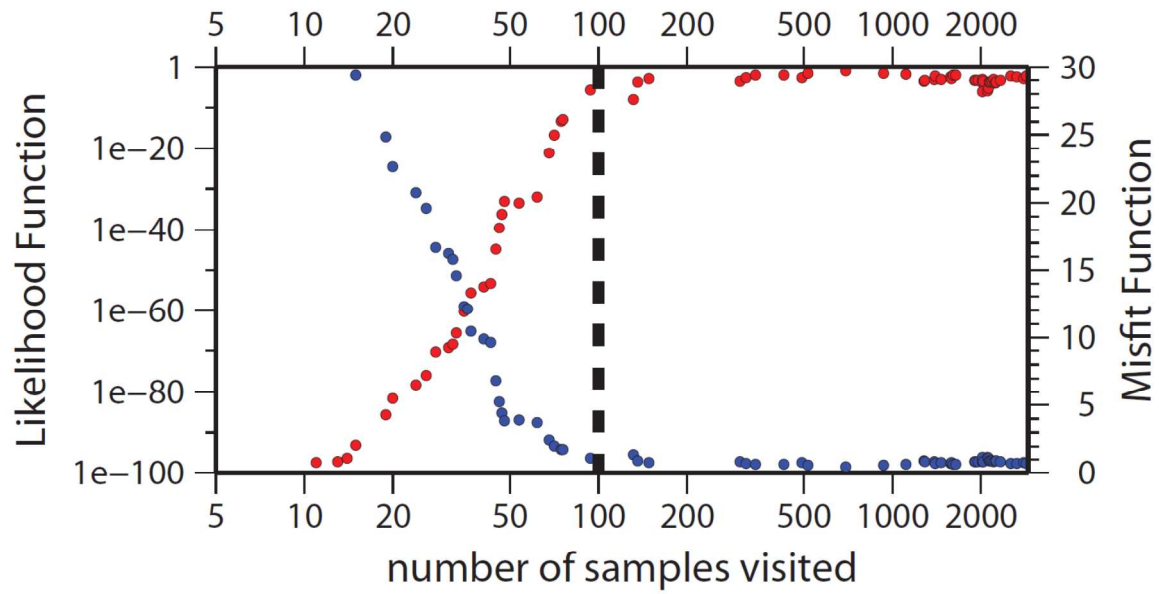


Figure 9

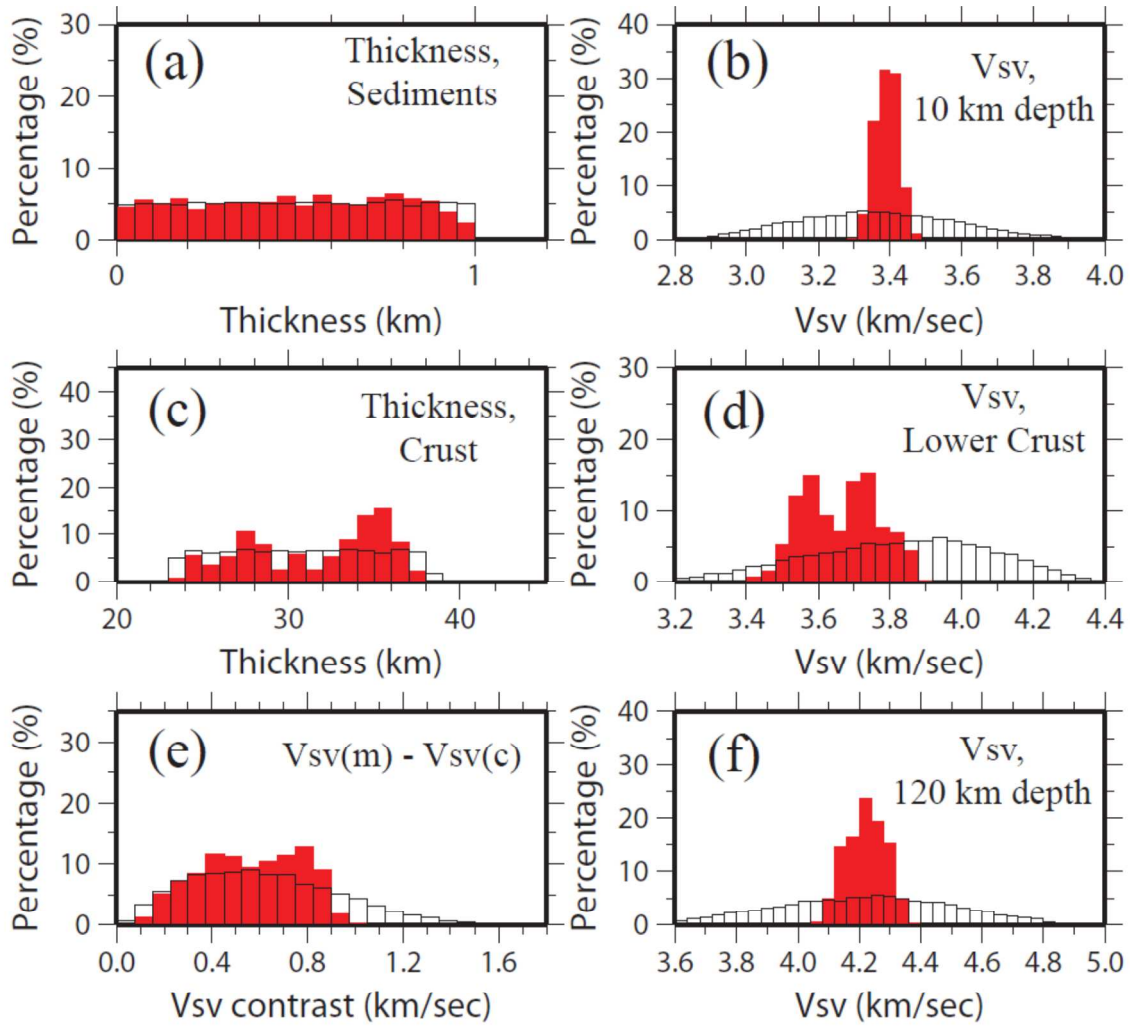


Figure 10

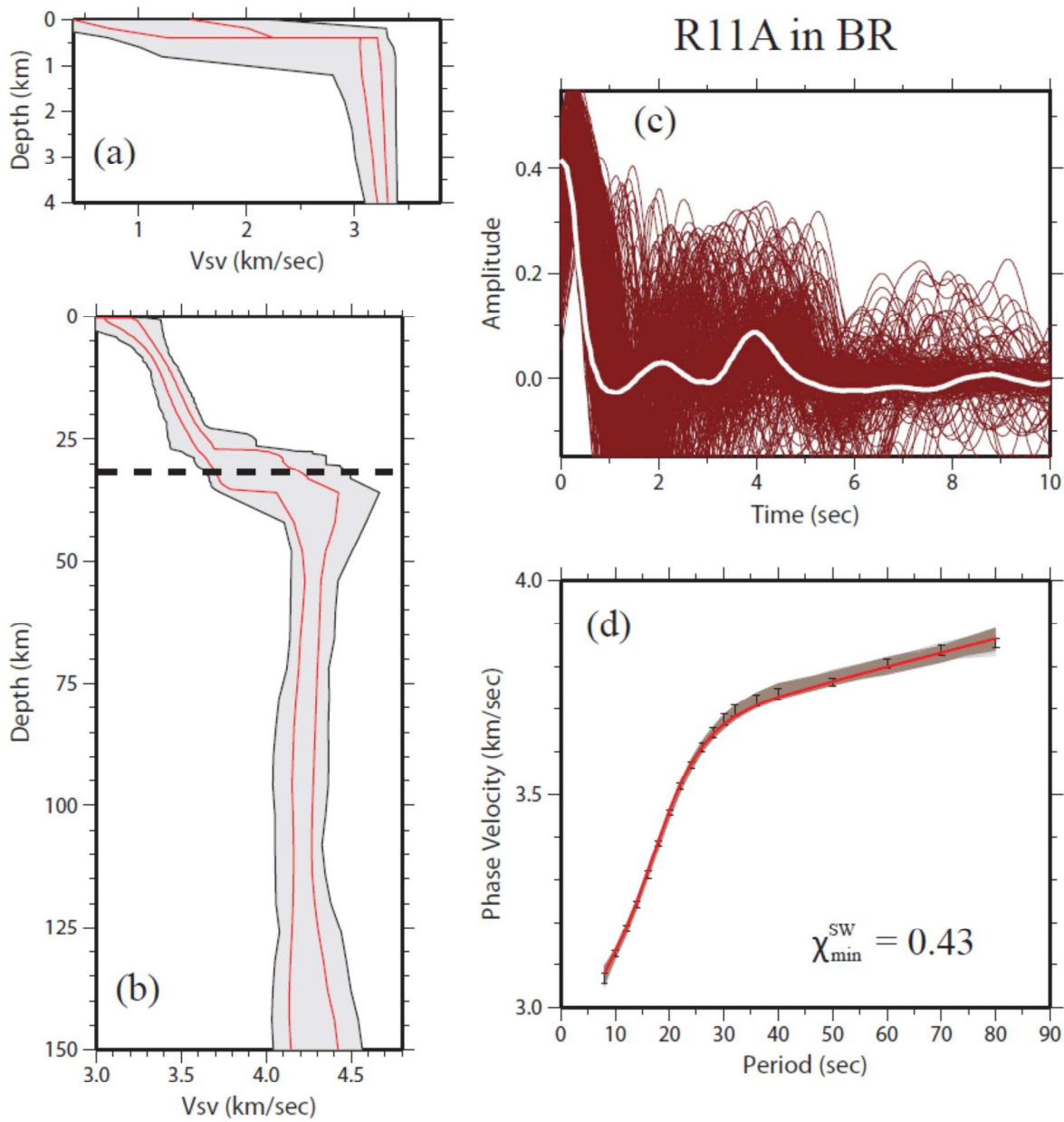
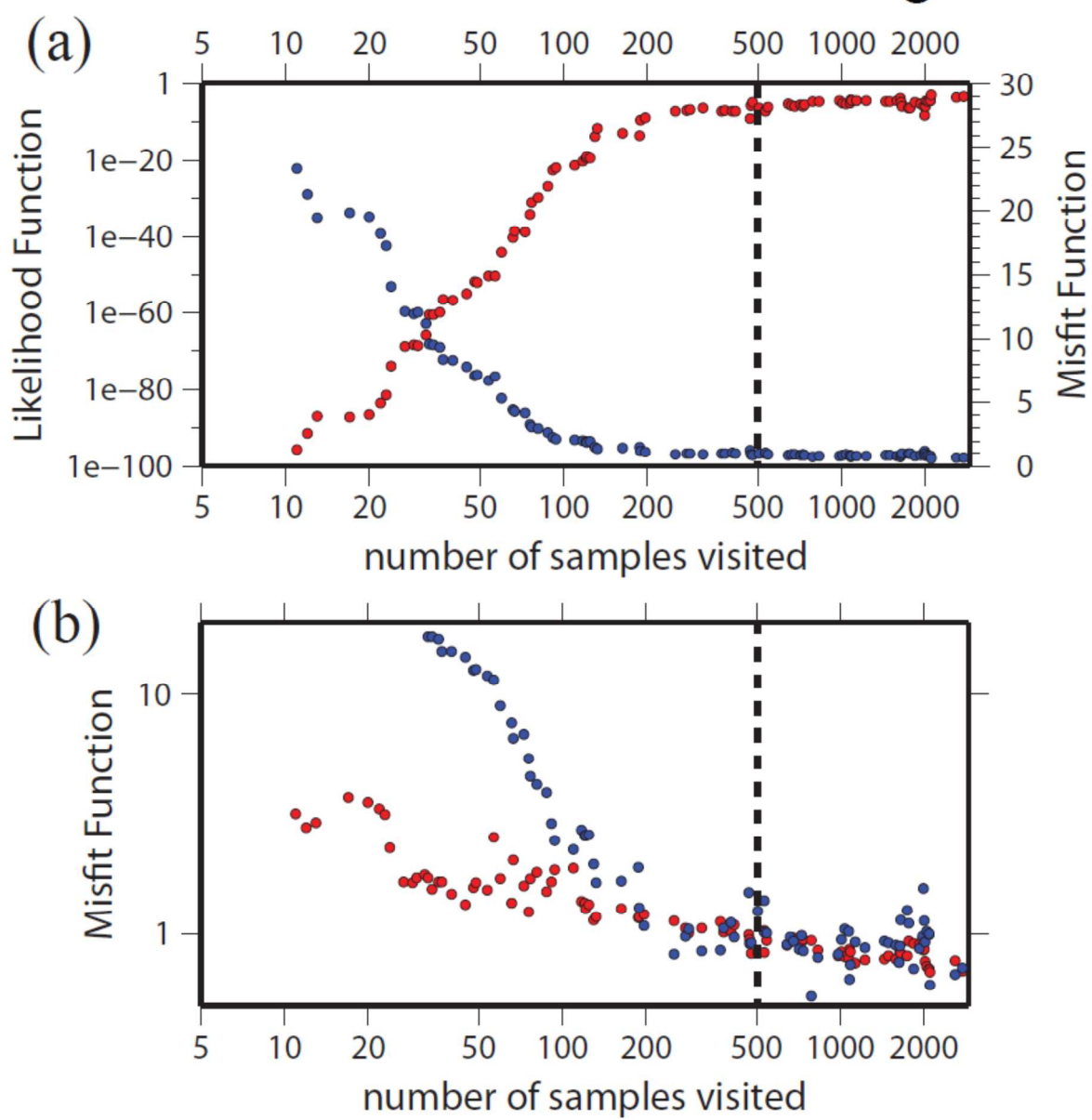


Figure 11



1
2
3
4
5
6
7
8
9
10
11
12
13
14
15
16
17
18
19
20
21
22
23
24
25
26
27
28
29
30
31
32
33
34
35
36
37
38
39
40
41
42
43
44
45
46
47
48
49
50
51
52
53
54
55
56
57
58
59
60

Figure 12

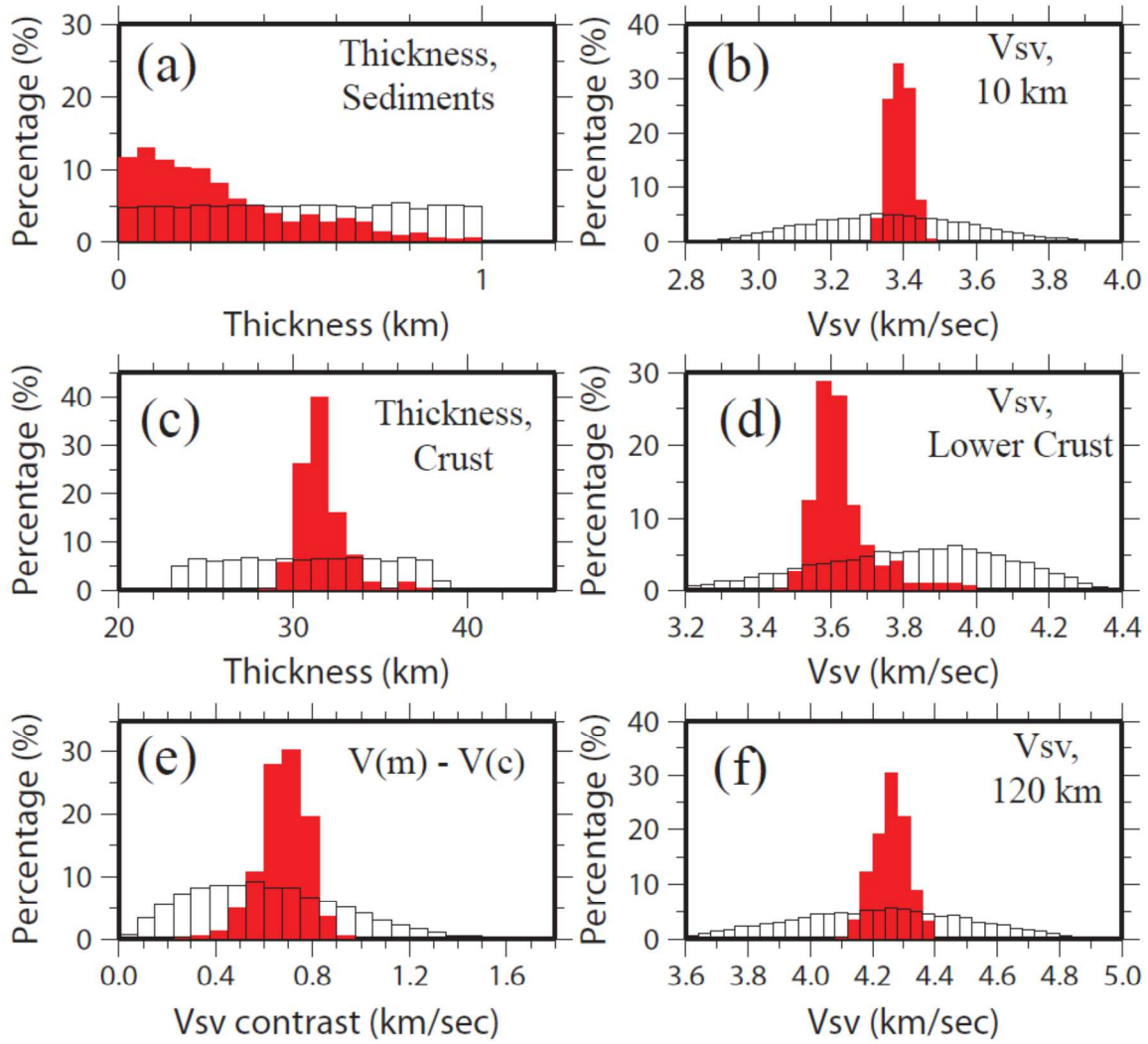
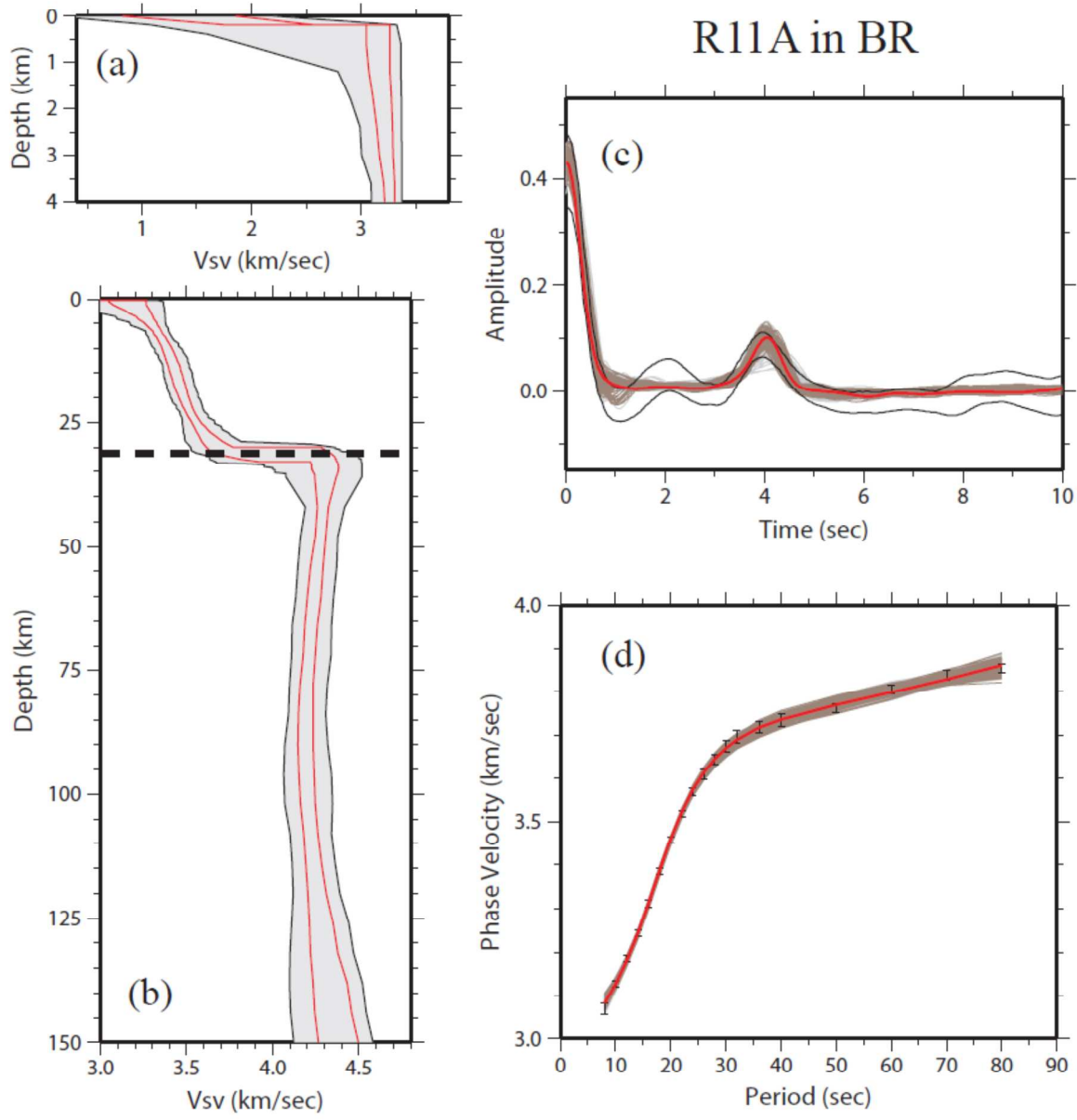


Figure 13



1
2
3
4
5
6
7
8
9
10
11
12
13
14
15
16
17
18
19
20
21
22
23
24
25
26
27
28
29
30
31
32
33
34
35
36
37
38
39
40
41
42
43
44
45
46
47
48
49
50
51
52
53
54
55
56
57
58
59
60

Figure 14

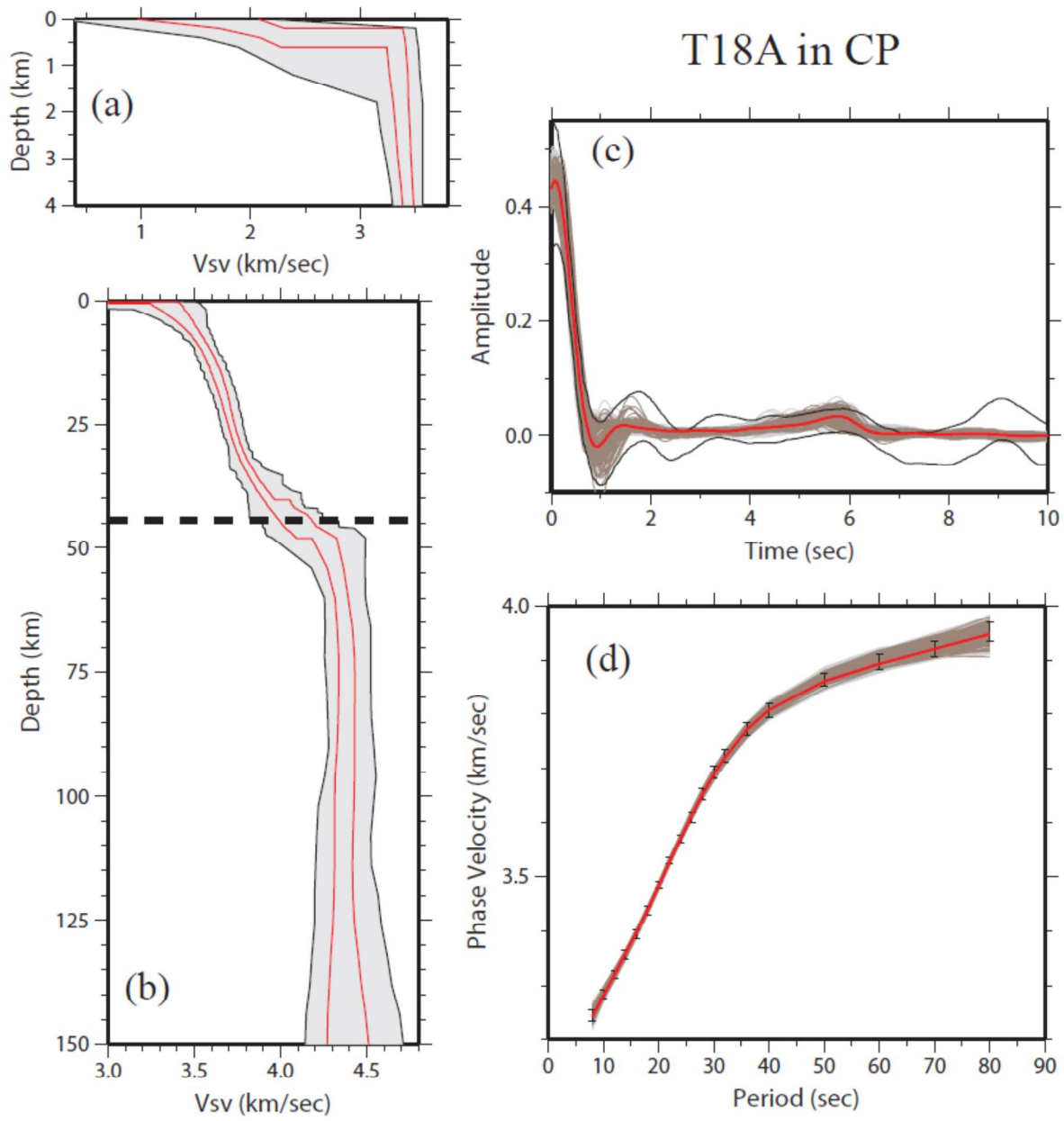
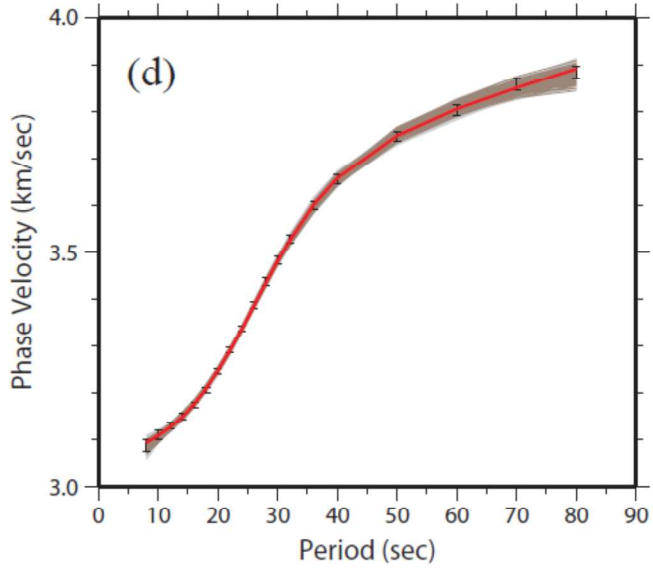
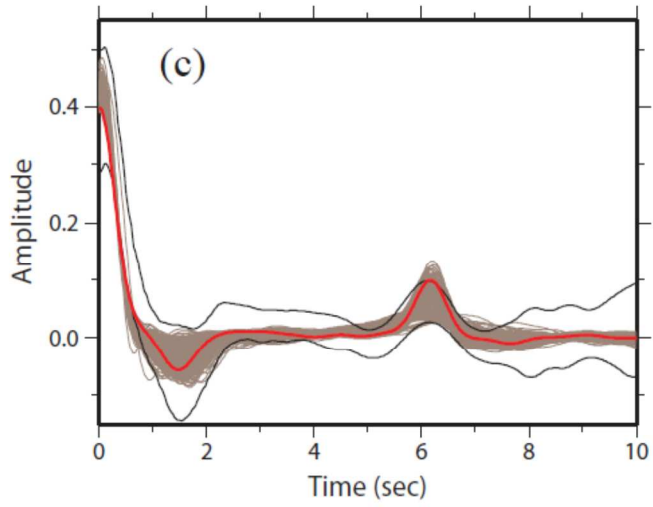
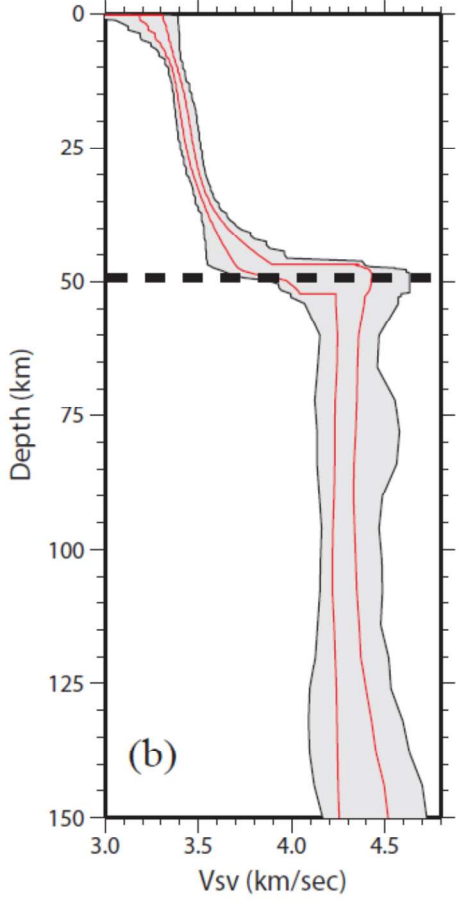
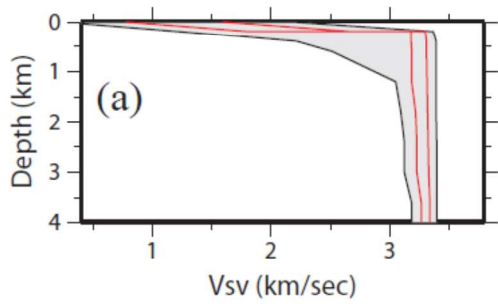


Figure 15

Q22A in RM



1
2
3
4
5
6
7
8
9
10
11
12
13
14
15
16
17
18
19
20
21
22
23
24
25
26
27
28
29
30
31
32
33
34
35
36
37
38
39
40
41
42
43
44
45
46
47
48
49
50
51
52
53
54
55
56
57
58
59
60

Figure 16

O25A in GP

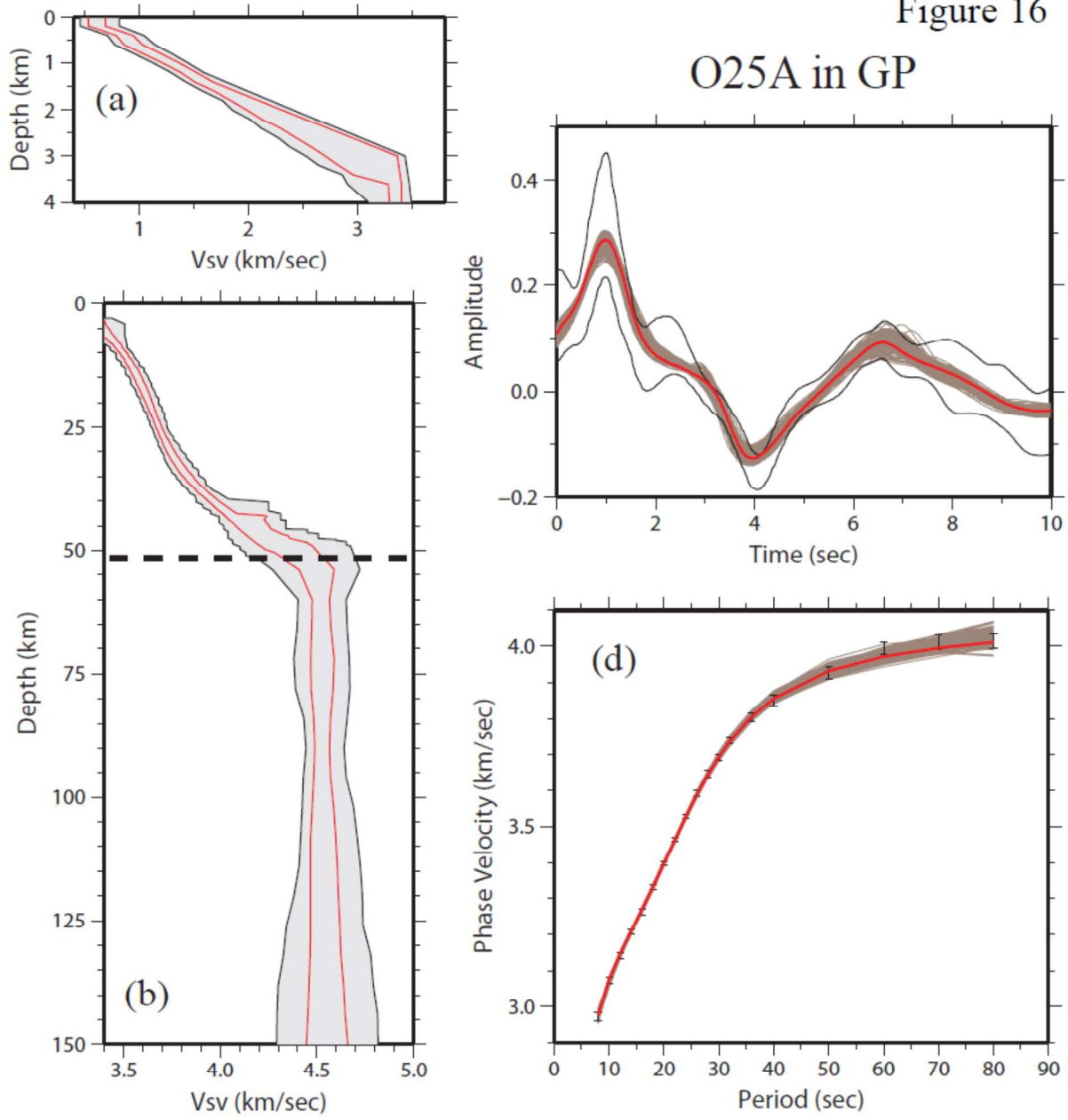


Figure 17

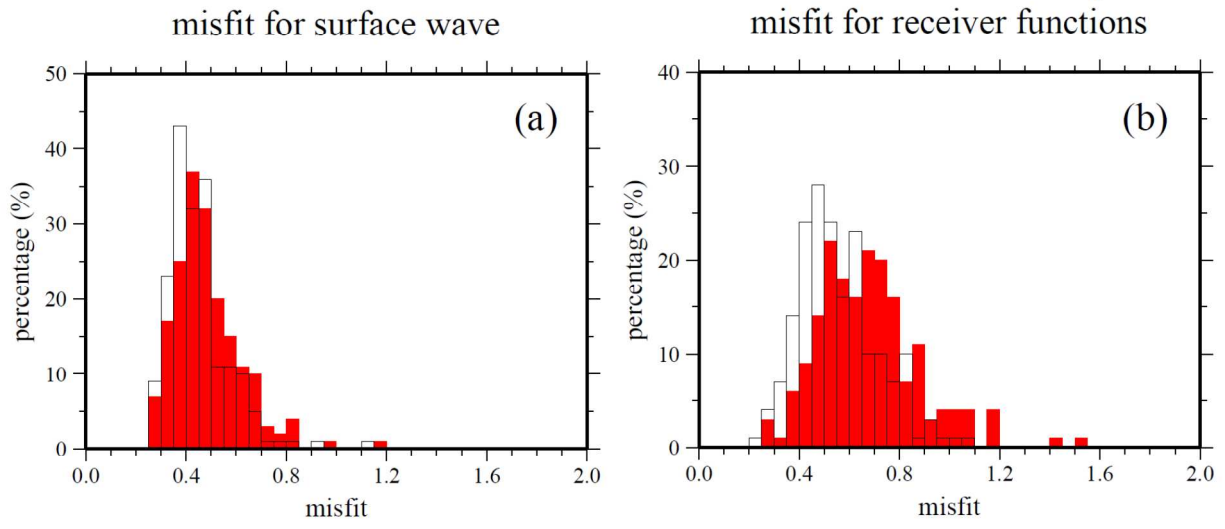


Figure 18

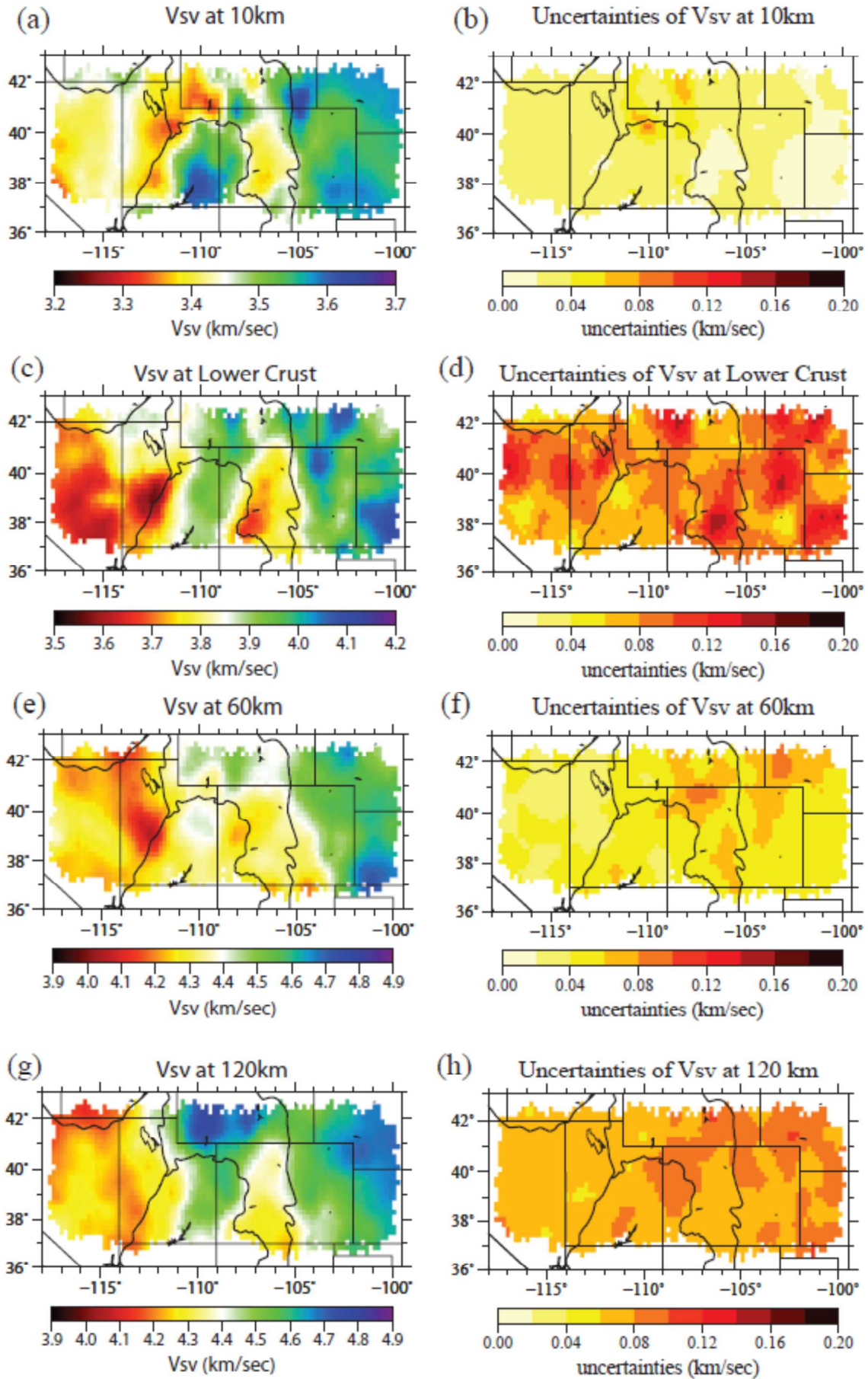
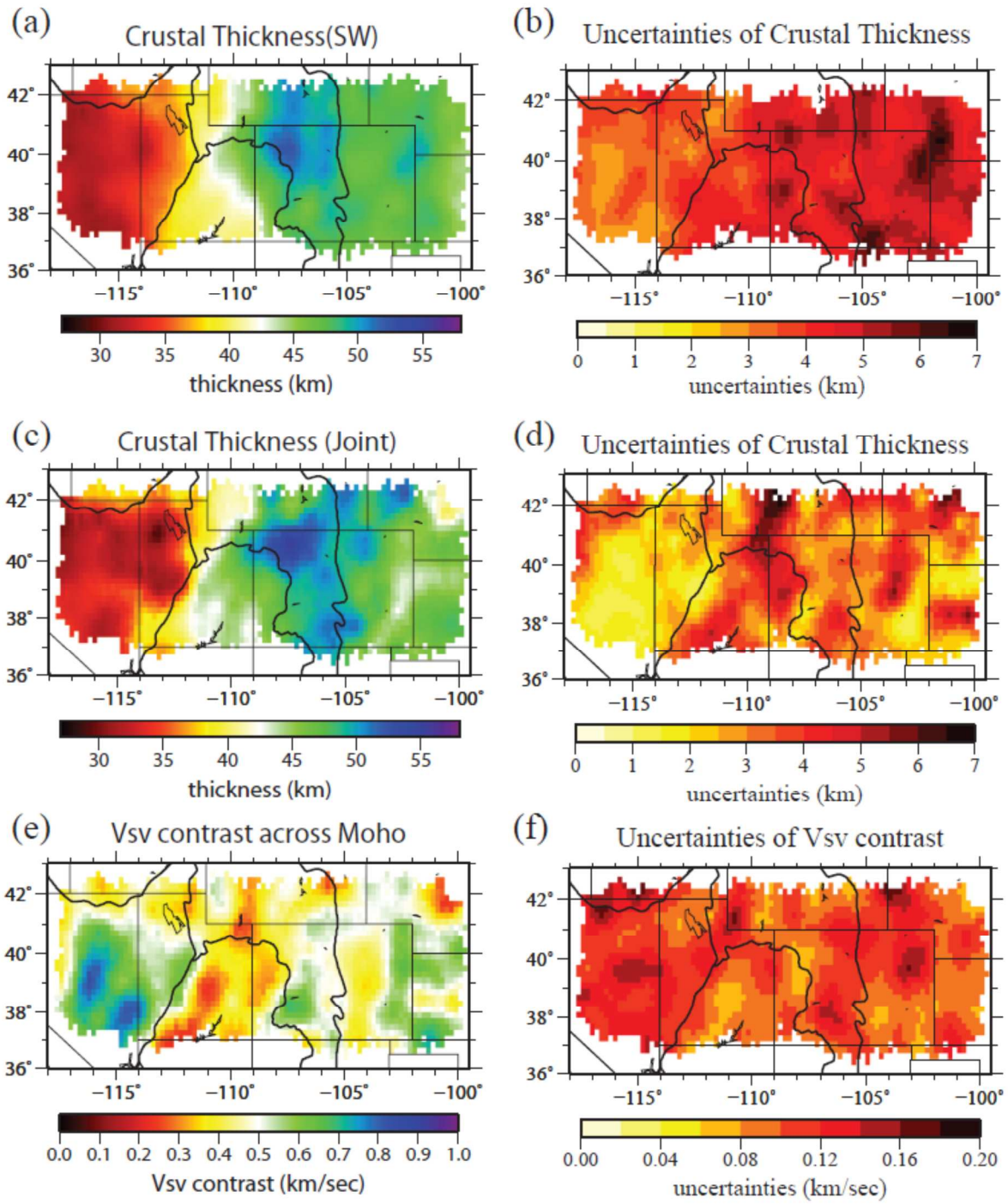


Figure 19



1
2
3
4
5
6
7
8
9
10
11
12
13
14
15
16
17
18
19
20
21
22
23
24
25
26
27
28
29
30
31
32
33
34
35
36
37
38
39
40
41
42
43
44
45
46
47
48
49
50
51
52
53
54
55
56
57
58
59
60

Figure 20

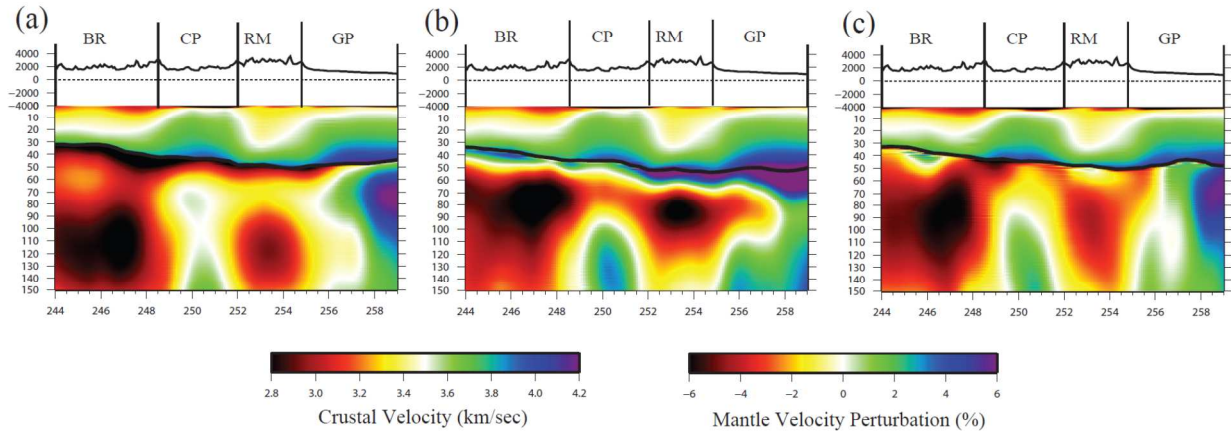
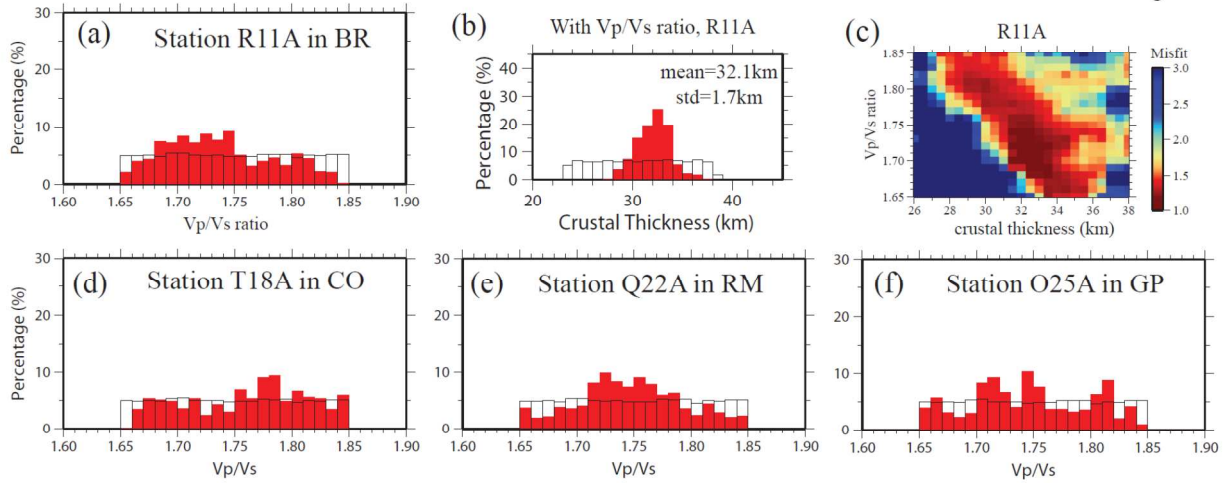
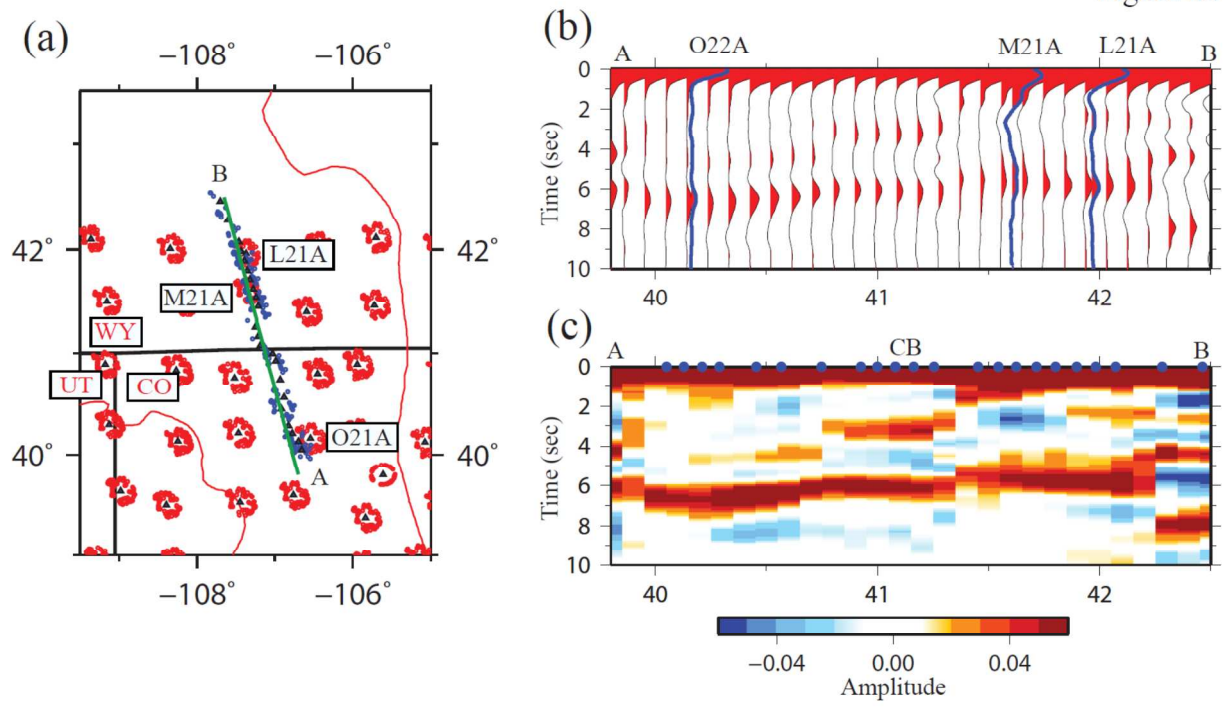


Figure 21



1
2
3
4
5
6
7
8
9
10
11
12
13
14
15
16
17
18
19
20
21
22
23
24
25
26
27
28
29
30
31
32
33
34
35
36
37
38
39
40
41
42
43
44
45
46
47
48
49
50
51
52
53
54
55
56
57
58
59
60

Figure 22



Peer Review

Figure A1

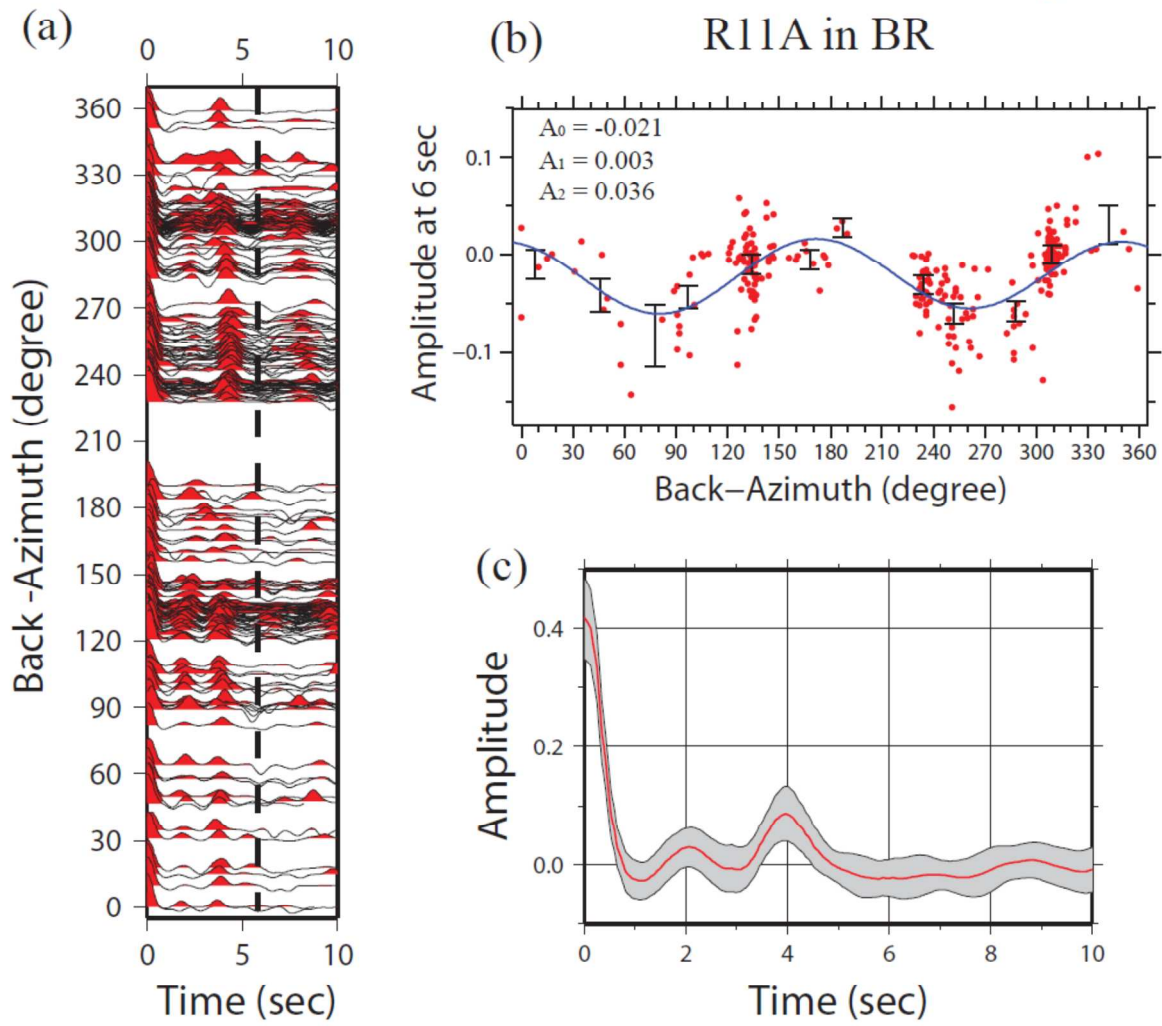


Figure A2

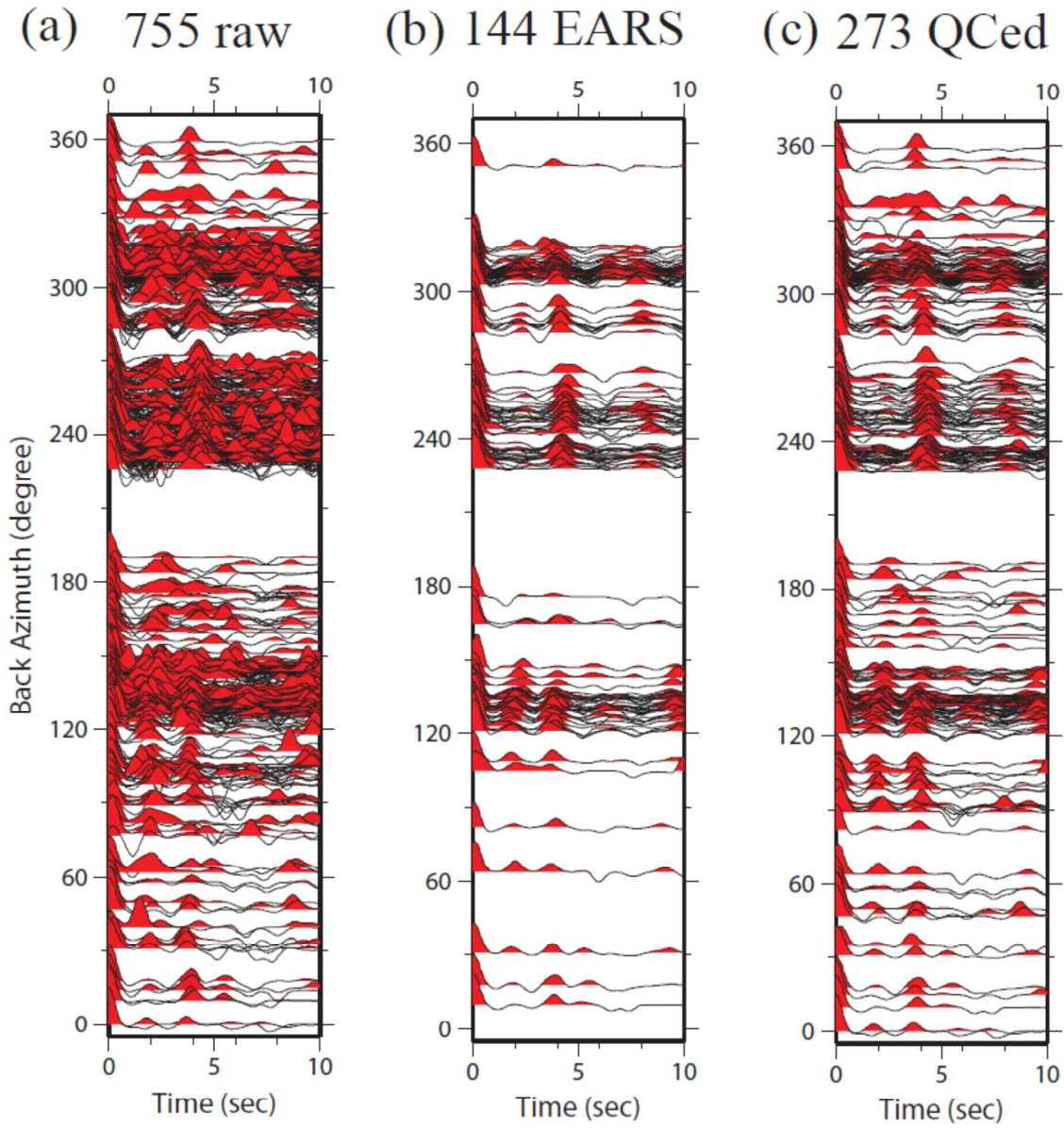
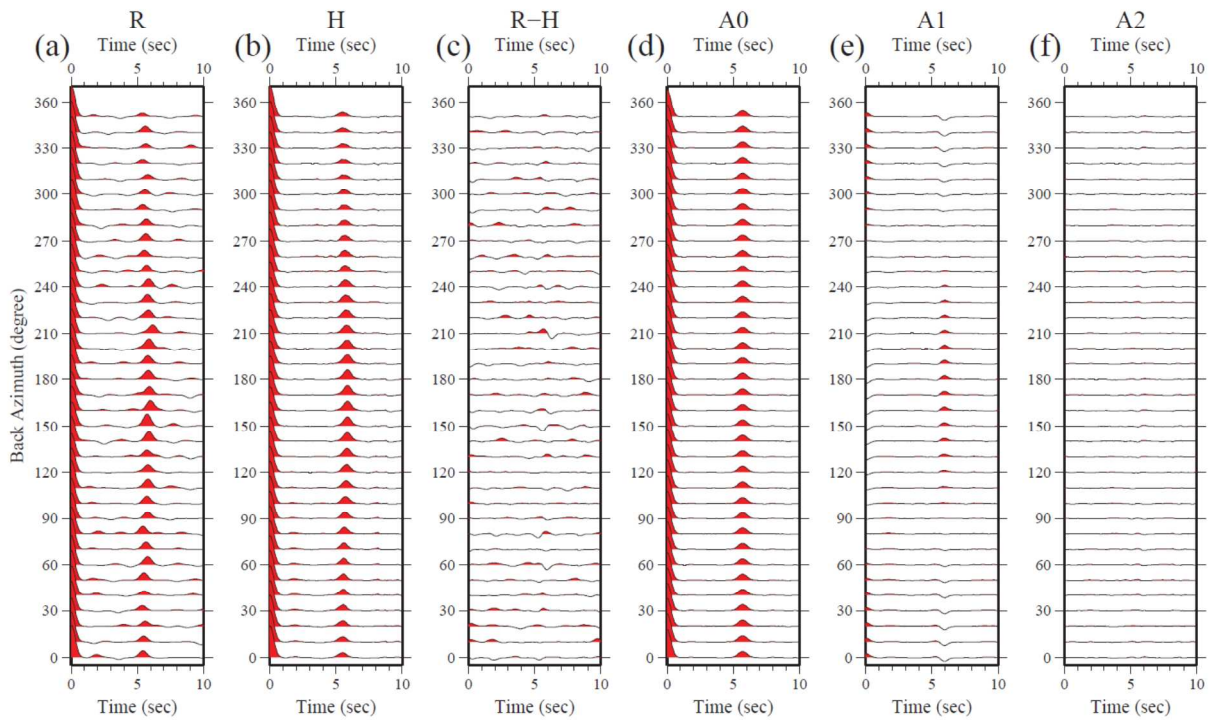
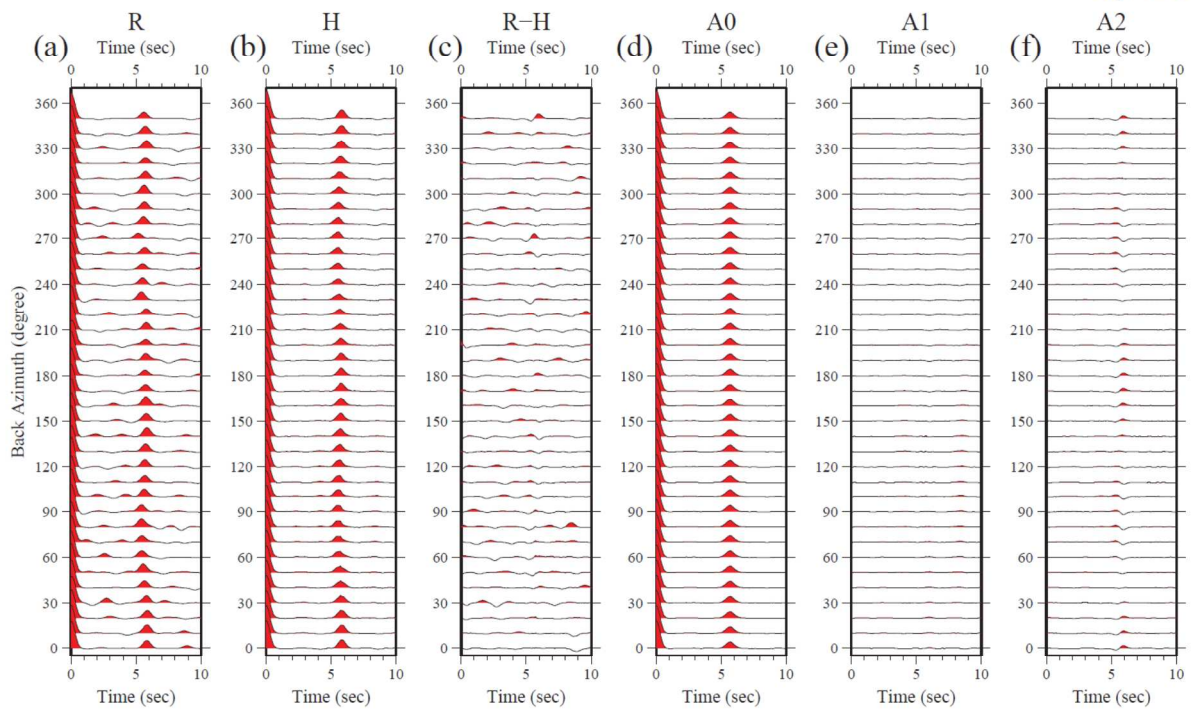


Figure A3



Review

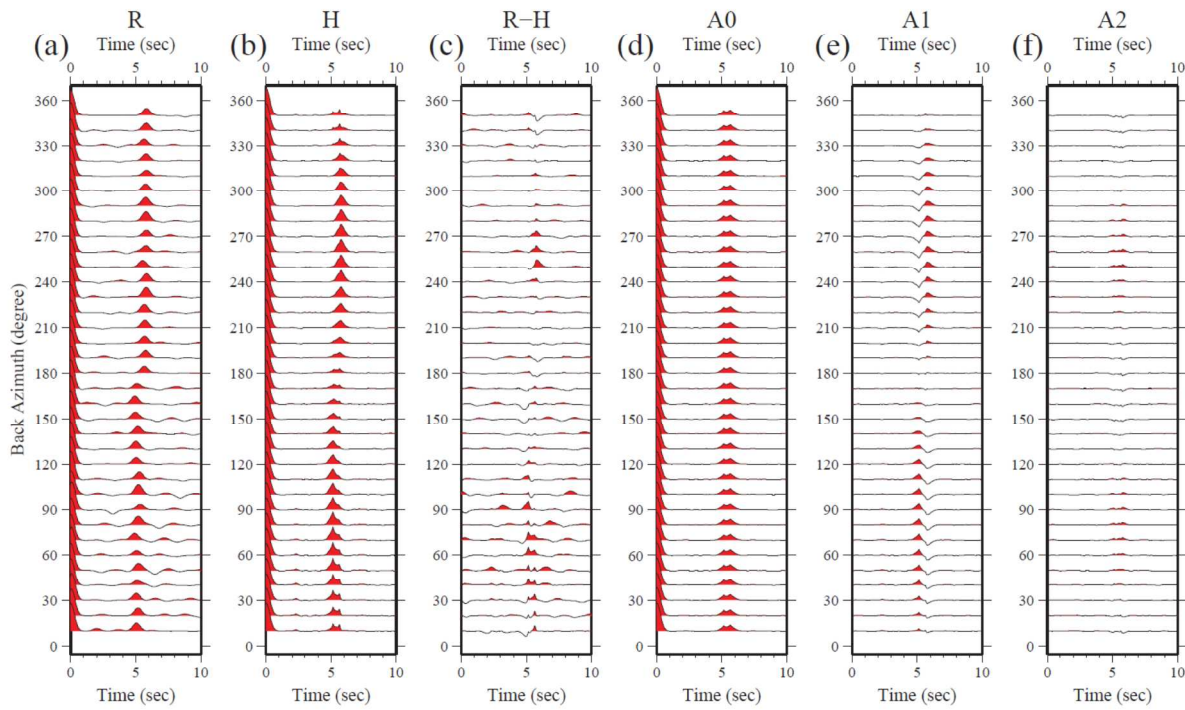
Figure A4



1
2
3
4
5
6
7
8
9
10
11
12
13
14
15
16
17
18
19
20
21
22
23
24
25
26
27
28
29
30
31
32
33
34
35
36
37
38
39
40
41
42
43
44
45
46
47
48
49
50
51
52
53
54
55
56
57
58
59
60

er Review

Figure A5



Peer Review

Figure A6

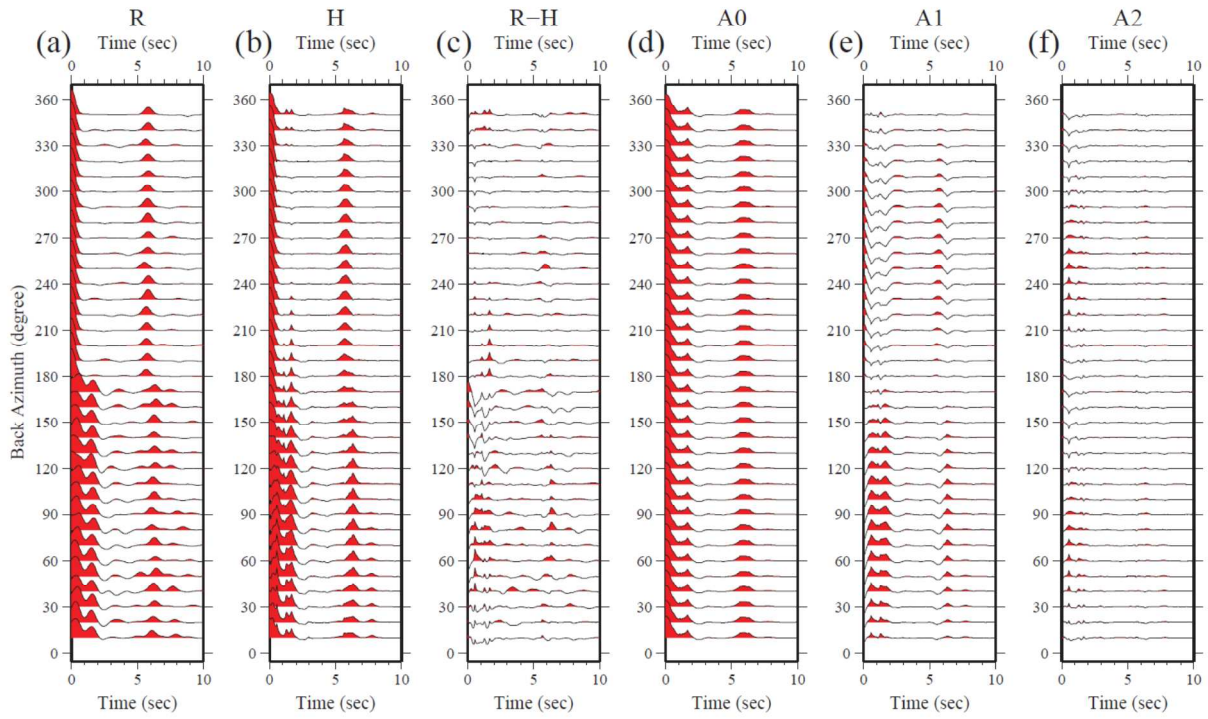
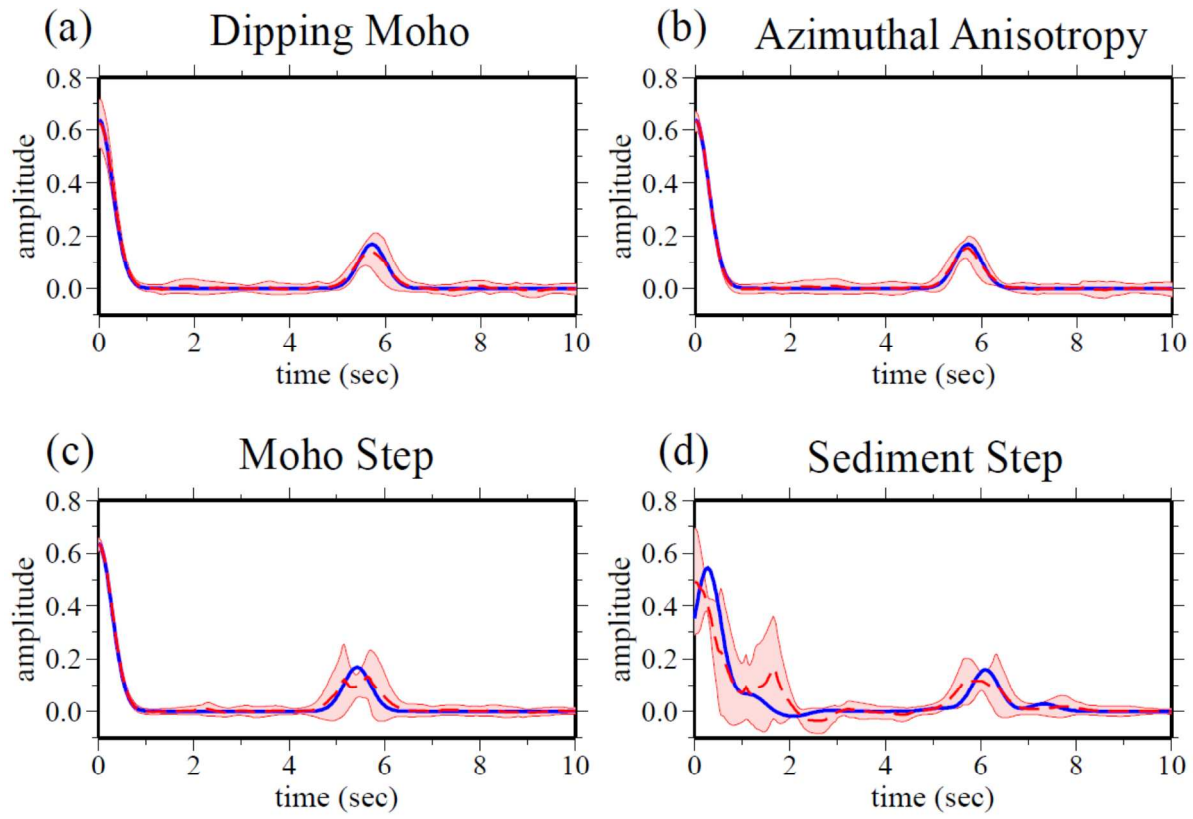


Figure A7



review